Femtosecond electron and X-ray source developments for time-resolved applications

THÈSE N^{O} 6938 (2016)

PRÉSENTÉE LE 17 JUIN 2016

À LA FACULTÉ DES SCIENCES DE BASE
GROUPE HAURI
PROGRAMME DOCTORAL EN PHYSIQUE

ÉCOLE POLYTECHNIQUE FÉDÉRALE DE LAUSANNE

POUR L'OBTENTION DU GRADE DE DOCTEUR ÈS SCIENCES

PAR

Fernando ARDANA LAMAS

acceptée sur proposition du jury:

Prof. V. Savona, président du jury
Prof. C. P. Hauri, directeur de thèse
Dr I. Radu, rapporteur
Prof. J.-P. Wolf, rapporteur
Prof. M. Chergui, rapporteur

ÉCOLE POLYTECHNIQUE
FÉDÉRALE DE LAUSANNE

Suisse
2016

You may say that I’m a dreamer
but I’m not the only one.
— John Lenon

To my parents, sister and friends . . .

Acknowledgements

This thesis would not exist without the continuous support, mentoring, patience and friendship of my supervisor Christoph P. Hauri. Thanks to his efforts and sacrifices this research has become possible. Many many thanks to Alexander Trisorio, Carlo Vicario, Clemens Ruchert, Marta Divall and Christian Erny for introducing me to the fascinating world of femtosecond lasers and sharing together these wonderful years. It has been a real pleasure to work with all of you. I also want to thank Andreas Dax, Mostafa Shalaby, Julien Rehault and Yunpei Deng for giving me the possibility to learn many things for each of them and sharing a great time with them. Special thanks go as well to Frederic Le Pimpec for his mentoring and all the fruitful discussions, and to Alexander Anghel for his collaboration on the photochathode developments. Special thanks go to Edwin Diwall, Collings Higgs, Hanspeter Gehrig, Thomas Steigmeier, Lars Binder and Ivo for their support in setting up the HHG beamline, to the people from Amplitude Technologies for their contributions in setting up the laser systems, to Guillaume Lambert, Boris Vodungbo and Jan Luning for the time we spend together during the different experiments on HHG and magnetism as well as for all the scientific discussions. To the team of the THz beamline at FLASH: Nikola, Tosten and Marc for all the support during the measurement including getting us to know the city. To the whole SwissFEL project (Hans Braun, Rafael Abela, Romain Ganter, Pavle Juranic, and many others) for all their contributions and their advice.

My main thanks go to my family: Maria Angeles, Fernando, Talia, Ewoks and Eva without your continuous teaching and support I will not be the person I am today. Huge thanks to my Spanish-Swiss colleges, especially to Ainara Irastorza for all the moment shared during these years, to Henar Rojo for so many coffees together, Maria Cabanes for all the hikes we did and to Aurora Alberca for teaching that time is more like a big ball of wibbly wobbly... time-y wimey... stuff. Many, many thanks to Raquel Almonte for standing on my side during the past and work dominated eight months making me feel so special. To Marta and Victoria for making the day by day life so nice. Many thanks to Laura and Roberto for getting me to know the wonders of Zurich city. Finally special thanks to the ones that are not here anymore: Lenin, Baby, Chiapas, Lola and Nana and of course to the one who just arrived, Baldo.

Baden, 18 January 2016 F. A. L.

Abstract

This manuscript summarizes the different technological developments and scientific activities in the field of ultrafast laser and electron physics which I have carried out as part of my PhD thesis. The topics addressed in my thesis range from the development of a novel electron gun to the construction and operation of a coherent X-ray laser, which I used for the study of ultrafast magnetization dynamics. The work was carried out within the frame of SwissFEL at the Paul Scherrer Institute.

Electron sources with a very good beam quality are a prerequisite for the realization of compact free electron lasers. In the first part of my work I will describe a novel electron cathode, which is based on a micro-structured surface. The cathode offers a quantum efficiency 2 orders of magnitude larger than what is achieved with conventional metallic cathodes.

Then I will describe a table-top soft x-ray source based on HHG where I have played a major role in the construction and commissioning. The generated attosecond pulse train from this source has been characterized by means of a newly developed Terahertz streak camera. Furthermore, first attempts have been made to extend the the spectral range offered by HHG to significantly higher photon energies (up to 400 eV) using an intense mid-infrared laser. Such a source will enable new science applications in near future.

Finally, the ultrashort x-ray pulses were used to study ultrafast magnetic dynamics in Cobalt thin films. For this purpose two different techniques, namely XMCD and X-ray MOKE were implemented and tested at the HHG beamline and first studies on ultrafast magnetization were successfully performed.

Key words: **Ultrafast sciences** **High-order harmonis** **High-brightness electron beam** **THz applications** **Magnetization dynamics** **THz streak camera**

Zusammenfassung

Dieses Manuskript fasst die verschiedene technischen Entwicklungen und wissenschaftlichen Taetigkeiten im Feld der Ultraschnellen Laser- und Elektronenphysik zusammen, die ich im Rahmen von meiner Doktorarbeit durchgefuehrt habe. Der Themenkreis erstreckte sich von der Entwicklung einer neuartigen Elektronenkanone bis hin zum Aufbau und Betrieb eines kohaerenten Roentgenlasers, der zum Studium von ultraschnellen Magnetisierungsdynamiken verwendet wird. Diese Arbeiten wurden im Rahmen vom SwissFEL Projekt durchgefuehrt. Elektronenquellen mit einer sehr guten Strahlqualitaet sind die Voraussetzung fuer die Realisierung von kompakten Freien Elektronenlasern. Im ersten Teil meiner Arbeit beschreibe ich eine neuartige Elektronenkathode, die auf einer mikrostrukturierten Oberflaeche beruht. Die Kathode hat eine Quanteneffizienz, die 2 Groessenordnungen ueber derjenigen von herkoemmlichen metallischen Kathoden liegen. Des weiteren beschreibe ich eine auf HHG basierende Roentgenquelle, bei der ich massgeblich beim Aufbau und bei der Inbetriebnahme mitgewirkt habe. Die von dieser Quelle erzeugten Attosekunden Pulszuege wurden mittels einer neu entwickelten Terahertz Streakkamera zeitlich vermessen und fuer weitere Anwendungen optimiert. Ebenfalls wurden erste Versuche unternommen, um den spektralen Bereich signifikant zu erweitern unter Verwendung eines intensiven Lasers, der im mittleren Infrarot emittiert. Die damit erzeugte Roentgenstrahlung erreicht Photonenenergien bis hin zu 400 eV, was neuartige Anwendungen ermoeglichen wird in naher Zukunft. Die ultrakurzen Roengtenpulse von dieser Quelle wurden ebenfalls verwendet um ultraschnelle magnetische Dynamiken in Duennfilmen zu studieren. Dafuer wurden zwei verschiedene Techniken XMCD und X-ray MOKE an der HHG Strahllinie implementiert und getestet und erste Untersuchungen an Duennfilmen erfolgreich durchgefuehrt.

Contents

List of Figures

List of Tables

1 Introduction

Science, from the Latin scientia ’Knowledge’, is defined as the organized set of the human knowledge. This definition imposes two major tasks on the scientist community, namely to organize and to expand the human knowledge. In this manuscript, I present the small contributions added to ultrafast science. In ultrafast science, we study physical phenomena that happen on a time scale smaller than 10^{-12} s. Such phenomena are relevant in many different research fields in physics and chemistry [2, 3, 4, 5].

To observe and understand phenomena occurring on ultrafast time scales we need to be able to ’see’ the dynamics happening on this scale. Human vision is useful for resolving movements occurring in the order of tens of milliseconds. Improved temporal resolution down to a few microseconds is achieved by the use of modern cameras. Even better temporal resolution is achieved by using the principle of stroboscopy. In stroboscopy, the fast vibration or rotation of mechanical system are recorded using short light flashes rather than a fast camera. Ultrafast science takes this principle to the extreme using light pulses with duration as short as few tens of attoseconds (10^{-18} s) to record ultrafast phenomena like photoionization [6, 7, 8], magnetization [9, 10] or molecular dynamics [11, 12].

It is difficult to give an exact date of birth for ultrafast science but it was probably close to 1965 when the first picosecond laser pulses were realized [13] using a mode-locked Nd:glass laser by means of a saturable absorber. Later on, in 1974 using a passively mode-locked dye laser the first femtosecond pulses were demonstrated [14]. During the last decades many efforts have been undertaken to develop novel ultrafast sources and techniques including the development of the chirp pulse amplification (CPA) [15] and the advent of Kerr-lens mode-locked oscillators [16]. Particularly exciting is the recent development of x-ray free electron lasers (FELs) [17]. FELs are a novel kind of large-scale facility where intense femtosecond x-ray pulses are generated by electrons accelerated to GeV energies and passing through elongated insertion devices. Most of the work presented in this thesis are indeed related to developments and experiments at the FEL currently being constructed at the Paul Scherrer Institute (SwissFEL). For example, the development of a high brilliance electron beam source is motivated by the need of such as electron source for the realization of compact FELs [18]. The development of intense soft x-ray pulses from a table top HHG system are important for FELs as HHG seeding is a recognized approach to improve the temporal FEL pulse characteristics significantly. Other efforts presented here, like the characterization of attosecond pulse trains by a Terahertz streaking camera or the study of ultrafast magnetization dynamics by means of an HHG beamline represent pilot experiments for future FEL efforts.

This thesis is organized in 4 chapters. The first chapter presents the development of a novel kind of multifilamentary photocathode [19, 20] for high-brilliance electron beam generation. The goal of my research was to investigate the full potential of this novel electron source and their capabilities to be implemented in a compact FEL.

In the second chapter, I describe the main activities performed during my thesis, which is the development of a high-order harmonic generation (HHG) source. Laser-driven HHG in a rare gas are an elegant and simple way for producing the shortest light pulses ever observed nowadays [21]. The photon energies provided by HHG range from the VUV up to the water window and beyond [22, 23]. The advantage of HHG-based sources are their compactness which allows straightforward implementation in modern laser labs. However, HHG has the drawback of providing low photon fluxes. Furthermore, the photon flux decreases dramatically for photon energies interesting for applications (e.g. L absorption edge of atoms). The characteristics of our laser system make our HHG source suitable for applications where a large number of photons per pulse are required.This includes the development of a bright high-order harmonic generation beamline for seeding a free electron laser. Seeded FELs have many advantages respects to self-amplified by spontaneous emission (SASE) FELs. In seeded FELs the generated radiation presents larger longitudinal coherence as well as a better spectral stability. Because the HHG are generated using a laser system the pulses of an HHG seeded FEL becomes intrinsically synchronized to this laser system improving in this way the synchronization of the pump-probe experiments. However, FEL seeding at short wavelength is a challenging task. The FEL shot noise (ASE radiation) increases with the photon energy. On the other hand, the brightness of HHG sources decreases dramatically for higher photon energies. These opposite behaviors motivate the development of a powerful HHG source with sufficient seed power to overcome the FEL shot noise for wavelength below 40 nm [24, 25, 26].

The HHG source developed here it an excellent tool for feasibility studies prior to FEL experiments. An example of such an application is given in chapter 3, which describes the streaking measurements of an attosecond pulse train. These measurements have been performed with the THz streak camera which will be used at SwissFEL. Temporal characterization of HHG pulses using a near infrared (NIR) streak field is a well know technique which has been combined with Terahertz a few year ago by Frühling et al. [27]. This way the measurement range of the streak camera could be expanded towards larger time windows. This makes possible to perform temporal characterization of the entire attosecond pulse train from HHG or femtosecond FEL pulses. The temporal characteristics of the FEL pulses, with a pulse duration in the order of tens of femtosecond and with a jitter in the arrival time if hundreds of femtoseconds, make impossible to use conventional IR streak cameras. Also the shot- to-shot fluctuations on the FEL pulses make not feasible to use scanning techniques like FROG or x-ray autocorrelation to perform the temporal characterization of the FELs. Using HHG, THz streak camera allows to perform the characterization of the full attosecond pulse train (ATP) without the need of long scans. This is important for HHG sources like ours with a large number of photons per pulse but with low repetition rates.

In chapter 4 I present studies on ultrafast magnetization in cobalt samples. The original idea behind these studies was to use a strong THz field [28] to coherently control magnetization. Using this strong field we observed for the first time magnetization dynamics phase-locked to the magnetic field of the laser. This entails a femtosecond control of the magnetization dynamics. With the HHG source developed here, it is possible to study ultrafast magnetization dynamics with element sensitivity, thanks to the large spectrum provided by HHG. The required techniques like XMCD and X-ray MOKE have been set up and commissioned in our HHG beamline as part of my thesis.

Finally, I would like to thank the entire SwissFEL laser group for contributing to this work in many different aspects. Even more, in general, the scientific developments presented here could have never been achieved without the quasi-anonymous contributions of thousand of researchers from the past. For this reason, along this manuscript we refer always to ’we’ as the subject.

2 Characterization of a novel metallic multifilamentary photocathode

Contents

Electrons accelerated to relativistic speed are essential for the realization of modern x-ray facilities like synchrotron sources and free electron lasers (FELs). To produce bright X-ray pulses in FELs a low-emittance electron beam is required carrying a charge of a few hundred picoCoulomb. Since modern linear accelerators preserve the electron beam emittance it is the electron source which defines the ultimate beam brightness. The motivation of our research lies therefore in the development of a high brightness electron source. In this context we explored photoemission of a novel type of electron emitter, which is a microstructured Nb and Nb_3Sn cathode. The cathode offers a quantum efficiency which is significantly higher than conventional metal cathodes.

The chapter is organized as follows. The first section outlines the theory of electron generation in metal photocathode illuminated by a laser and introduces the basic concept of a low emittance electron beam and its characterization. The second section presents the experimental results of the electron beam characterization emitted by the micrometric-sized Nb and Nb_3Sn filamentary cathode, such as quantum efficiency, transverse beam profile and emittance. Two different emission regimes will be discussed that depend on the intensity of the illuminating laser.

2.1 Photocathode theory

Three different emission mechanisms are typically employed for electron production.Thermionic emission, field emission and photo emission. Thermionic emission of electrons occurs, for example, when a thin wire is heated above 1000 °C. At such high temperatures the electrons are continuously released from the material as their kinetic energy is sufficiently high to overcome the material's workfunction. For pulsed electron sources field emission or photo-emission is typically employed. Field emission occurs when the cathode is exposed to a strong external electric field, originating e.g. from a laser. Under such conditions the workfunction is reduced by the Schottky effect which significantly enhance the propability of the electrons to tunnel through the potential barrier. Photo-emission of electrons occurs when a metal or semiconductor is irradiated with photons whose energies are normally higher than the material workfunction. Electron guns using photocathodes can control the 3-D electron distribution by shaping the spatial and temporal profile of the driver laser. Most of modern FELs use a laser-illuminated photocathode as electron source since it offers excellent electron beam properties, such as a low emittance, high charge, a well-definded electron bunch shape and high stability. We therefore present the mechanism of photo-electron emission in the section below.

2.1.1 Three step model for photo-electron emission

The performance of a cathode material can be described by its quantum efficiency (QE) and thermal emittance. QE is defined as the ratio between the number of emitted electrons and the incident photons. The thermal emittance is related to the area of an electron beam in the position-momentum phase space. Both quantities can be estimated using a model where the photoemission process is divided into three sequential steps [29]. The main aspects of this model regarding the calculation of QE is presented in the following.

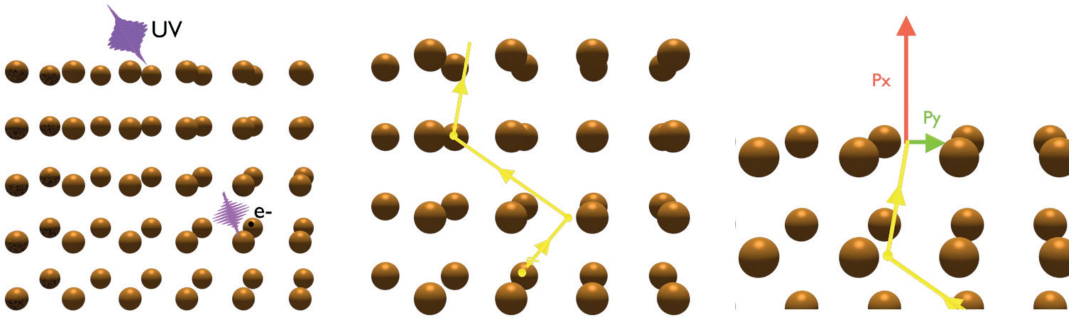

Figure 2.1: Sketch of the three step model describing the photo-electron emission from a photocathode. First step (left), a photo-electron is generated by means of an intense UV pulse. Second step (center), the generated electron travels to the surface. Third step (right), the electron overcomes the workfunction and is ejected from the surface.

A photon impinging a photocathode penetrates into the material by typically few tens of nanometers (in metals) and is absorbed by an atom. This leads to the ejection of a free electron (step I). The probability of this process is:

$$P_1(E,\hbar\omega) = [1-R(\omega)]\frac{\int_{E_l}^{\infty} F(E,T)N(E)[1-F(E+\hbar\omega,T)]N(E+\hbar\omega)}{\int_{-\infty}^{\infty} F(E,T)N(E)[1-F(E+\hbar\omega,T)]N(E+\hbar\omega)} \tag{2.1}$$

where N(E) is the density of states (DOS), $F(E,T)$ the Fermi-Dirac distribution function, $E_l = \phi_{eff} - \hbar\omega$ the minimum energy level of the electrons that after absorbing a photon can be excited to the continuum, ϕ_{eff} the effective workfunction that includes the reduction of the workfunction due to the Schottky effect ([30]), T the electron temperature and $R(\omega)$ the reflectivity of the cathode material.

In a first approximation the DOS is estimated by following the model of a free electron gas in 3D where $N(E) \propto \sqrt{E}$. This approximation is valid in simple metals but fails for transition metals. To obtain accurate and material dependent values of the QE the DOS is derived via numerical simulation using a FLAPW (full potential linearized augmented planewave) code named FLEUR [1]. Examples of these calculations are shown in fig. 2.2 .

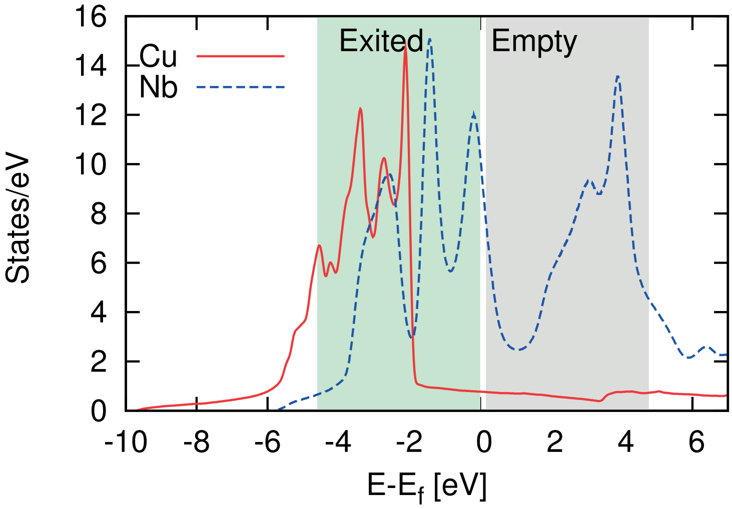

Figure 2.2: Example of two different DOS. In red copper and blue niobium. In niobium there is a high availability of empty states allowing the electron to be excited obtaining a higher QE.

In the second step the free electron travels across the material towards the surface undergoing different scattering processes like electron-electron scattering and electron-phonon scattering. These scattering processes are fundamentally different for metals and semiconductors, respectively. For example, electron-electron scattering is usually the dominant process in metal photo-cathodes. The energy loss due to scattering is high enough that a single scattering event is sufficient to reduce the kinetic energy below the kinetic energy required to overcome the barrier. For semiconductors there exist an energy window where pair production due to scattering process cannot take place. In this situation electron-electron scattering becomes negligible and electron-phonon scattering becomes the dominant process.

Because of the small energy loss in electron-phonon scattering and the fact that the process implies a change of the momentum of the scattered electron, electron-phonon scattering can increase the quantum efficiency. In normal conditions the momentum distribution of exited electrons is isotropic, meaning that only half of the electrons travel towards the surface. However with the reorientation produced by electron-phonon scattering the number of electron reaching the surface is increased enhancing the QE.

Due to these multiple scattering events the temporal profile of the electron beam emitted from a semiconductor may not mimic the temporal profile of the incident laser pulse. This limits the applications of semiconductor based photocathodes to applications where a rigorous control of the temporal profile of the electron beam is not required. Since FELs requires relative short (picosecond)and well shaped electron beams metallic photocathodes are normally used. Metal photocathode offers superior electron shaping capabilities, as the temporal profile of the electron bunch is almost an exact copy of the temporal laser profile. We mention that electron beam shaping is helpful to achieve the lowest possible emittance at the electron gun.

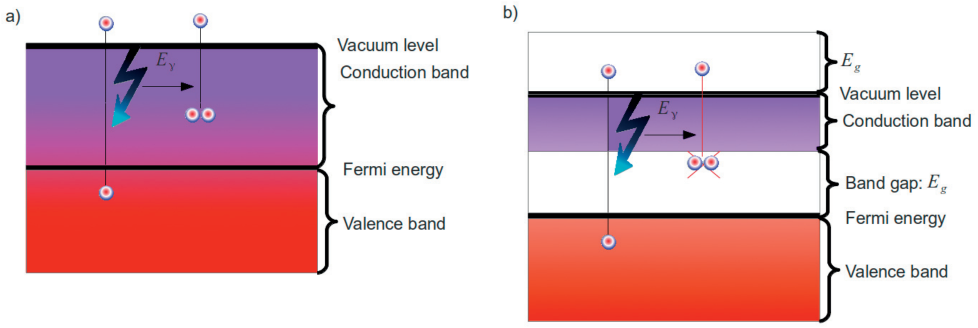

Figure 2.3: Band structure in a metal a) and semiconductor b). In semiconductors the presence of a bandgap avoids the creation of secondary electrons due to inelastic scattering of low energy (below bandgap) electron.

For metallic photocathodes, the probability of step II is given by:

$$P_2(E,\omega) = \frac{1}{1+\dfrac{\lambda_{opt}(\omega)}{\lambda_{e-e}(E)}} \tag{2.2}$$

where $\lambda_{opt}(\omega) = \lambda/4\pi k$ is the laser penetration length obtained from [31]. $\lambda_{e-e}(E)$ is the energy dependent electron-electron scattering mean free-path. Typically the values of λ_{e-e} are know for only few energies but according to Dowell [32] we can extrapolate from the reference value as: $\lambda_{e-e}(E) = \lambda_m(E)(E_m/E)^{3/2}$ where λ_m is the measured mean free path for electrons with energy E_m.

Finally in step III the electrons arrive to the photocathode surface and if the momentum component perpendicular to the surface is higher than the workfunction the electron is finally ejected.

$$P_3(\cos\theta_m) = \frac{\int_{\cos\theta_m}^{1} d(\cos\theta)}{\int_{0}^{1} d(\cos\theta)} \tag{2.3}$$

where $\cos\theta_m = \phi_{eff}/E$. Finally, the quantum efficiency is obtained by combining these three probabilities:

$$QE = P_1(T,\hbar\omega)P_2(E,\omega)P_3(\phi_{eff},\hbar\omega) \tag{2.4}$$

2.1.2 Workfunction reduction in a external electric field

It is important to take into account that in a modern electron gun the photocathode is embedded in a strong electric field. This electric field is used to accelerate the electrons as soon as they are ejected from the surface to several MeV in order to minimize space charge effects. However the strong electric field at the surface of the photocathode produces a Schottky barrier reduction modifying the effective workfunction of the material. In general the effective workfunction is given by the equation:

$$\phi_{eff} = \phi - \sqrt{\frac{e\beta F}{4\pi\epsilon_0}} \tag{2.5}$$

Where F is the peak of the electric field, β the field enhancement factor that takes into account a non-flat geometry for the photocathode and ϕ the workfunction of the material in the absence of the electric field.

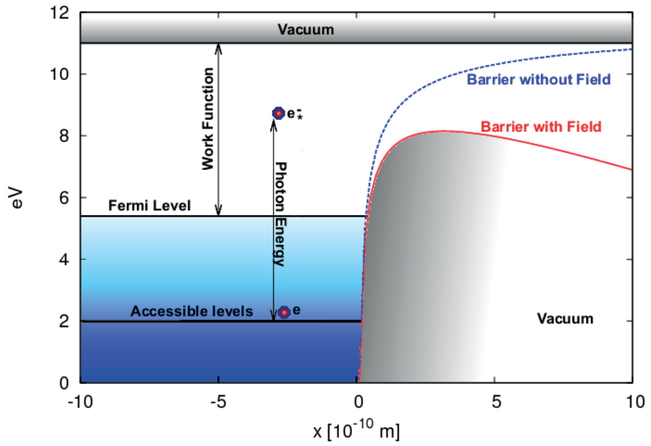

Figure 2.4: Energy levels of a metallic photocathode in the presence of a strong electric field showing the Schottky barrier reduction.

With this set of equations we have now the tools to predict the QE of metallic photocathodes. The equations assume that two photon absorption does not take place. This can be easily proved experimentally by representing the emitted charge as function of the number of photons. In case of obtaining a linear dependency single photon processes are dominant, however if a quadratic dependency is obtain a two photons process is dominant.

2.1.3 Low emittance electron beams

Electron beam emittance (ϵ_x) is defined as the averaged spread of the electron beam in a phase-space diagram of position and momentum:

$$\epsilon_x = \sqrt{\langle x^2\rangle\langle x'^2\rangle - \langle xx'\rangle^2} \simeq \sigma_x\sigma_p \qquad (2.6) \qquad \epsilon_{n,x} = \beta\gamma\epsilon_x \qquad (2.7)$$

For the approximation of eq. (2.6) a non-correlation between position and momentum is assumed. With the definition of eq. (2.6) the emittance depends on the electron momentum. As the electron momentum is not easily measurable in the experiment normalized emittance (eq. (2.7)) is normally used.

The development of low-emittance electron beams it is one of the main requirements for the realization of compact FELs. Modern X-ray FELs are based on the principle of self-amplified spontaneous emission (SASE) caused by an electron beam passing through an undulator section. In order to get the most efficient SASE process the electron beam has to fully cover the generated radiation along theentire undulator section while keeping the density of the electron beam high. Only a low emittance electron beam fulfills this condition particularly well.

The x-ray radiation generated in the undulator can be approximated as a point source [18] whose angular divergence and radius are given by:

$$\theta_r = \sqrt{\frac{2\lambda_r}{\lambda_u N_u}} \qquad (2.8) \qquad \sigma_r = \frac{1}{4\pi}\sqrt{\frac{\lambda_r\lambda_u N_u}{2}} \qquad (2.9) \qquad \epsilon_x \leq \frac{\lambda_r}{4\pi} \qquad (2.10)$$

where λ_r is the wavelength of the SASE radiation, λ_u the undulator period and N_u the number of undulator periods. Equation (2.10) defines the threshold for emittance for producing amplification of the spontaneous emission. A reduction of the normalized emittance is highly beneficial for the FEL performance as it gives rise to an increase of the saturation power as well as a decrease of the saturation length, producing more compact and bright FELs.

Experimentally there are several established methods to retrieve the electron beam emittance such as the pepper-pot technique[33], slit-scan [34] and solenoid scan approach[35] and others. A detailed explanation of the pepper-pot method is given in the next paragraph since it was routinely used for our emittance measurements. In general the method applied for the emittance measurement depends on whether the divergence of electron beam is dominated by the emittance or the space charge. To distinguish these regimes the laminary parameter (ρ) is typically used [18]. This parameter is given by:

$$\rho = \frac{Q\, \sigma_{xy}^2}{2\, I_A\, \gamma\, \tau_b\, \epsilon^2}, \tag{2.11}$$

σ_{xy} is the electron beam radius, I$_A$= 17 kA the Alfén current, γ the relativistic factor, τ_b the time width of the electron beam and ϵ the estimated beam emittance.

The pepper-pot method is based on a direct mapping of the phase-space of momentum and position coordinates by passing the electron beam through a dense array of a ’pepper-pot’ like holes imprinted on a metallic plate (fig. 2.5).This method is well suited for a high-charge electron beam with a laminarity parameter (ρ) larger than one since ideally each individual beamlet formed by passing through the pepperpot mask has a charge sufficently low such that space-charge effects are negligible.

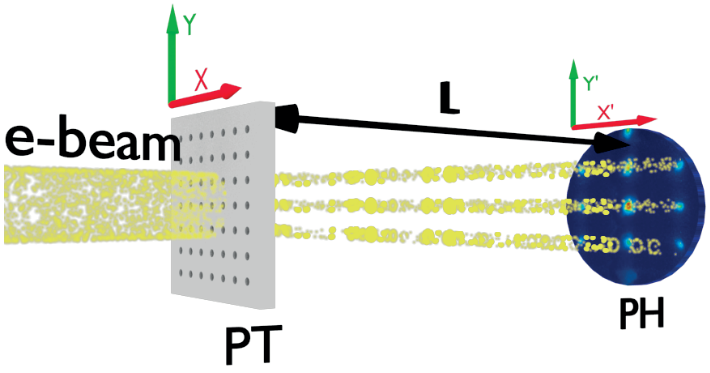

Figure 2.5: Scheme of a emittance measurement with a pepper-pot. L is the distance between the metal plate and the projection plane, PT the pepper-pot mask and PH the phosphor screen. X, Y represent the coordinates of the electron beam on the metallic plate and η, ν the coordinates on the projection screen.

In this configuration the rms angular distribution $\langle x'^2 \rangle$ and the cross term $\langle xx' \rangle$ can be derived following [33] given that:

$$\langle x'^2 \rangle = \frac{1}{N} \sum \left[n_j \sigma^2_{x'_j} + n_j(\bar{x}_j - \bar{x}')^2 \right] \tag{2.12}$$

$$\langle xx' \rangle = \frac{1}{N} \sum \left(n_j x_{sj} \bar{x}'_j - N\bar{x}\bar{x}' \right) \tag{2.13}$$

where N is the total number of electrons, $\bar{x}'$ the average position of the electron beam in the phosphor screen, n_j the numbers of electron passing though the j-slit, $\bar{x}_j$ and $\sigma_{x'_j}$ are the average position and the rms divergence of these electrons beam as they pass through the hole.

The value of $\sigma_{x'_j}$ can be obtained through the rms size (σ_j) on the phosphor screen of the electron beam that passes through the hole j, $\sigma_{x'_j} = \frac{\sigma_j}{L}$. By combining equations (section 2.1.3) and (section 2.1.3) and eq. (2.6) the emittance can be expressed as:

$$\epsilon^2_{rms} = \frac{1}{N^2} \left\{ \left[\sum_{j=1}^{p} n_j (x_j - \bar{x})^2 \right] \left[\sum_{j=1}^{p} \left(n_j \left[\frac{\sigma_j}{L} \right]^2 + n_j [\bar{x}'_j - \bar{x}']^2 \right) \right] - \left[\sum_{j=1}^{p} n_j x_j \bar{x}'_j - N\bar{x}\bar{x}' \right]^2 \right\} \tag{2.14}$$

2.2 Multifilamentary photocathodes

Here I present our work performed on a novel kind of metallic photocathode [19, 20]. The photocathode is made out of a matrix of Nb or Nb_3Sn filaments with 2 μm of diameter and 1 mm of height. The main result is the observation of two emission regimes which were found to depend on the laser fluence.

In the first regime the photocathode exhibit a QE that is typically in the order of 0.001%. This is a typical value found for metallic photocathodes. However by increasing the laser fluence above 10 $\frac{mJ}{cm^2}$, the QE increases two orders of magnitude up to 0.1%. Such a high QE is exceptional for metallic photocathodes. We provide an argument for the responsible physical mechanism yielding to this enhancement of the QE and present simulations on the QE, electron beam transport and acceleration of the electron beam through the beamline, from the cathode to the diagnostic tools. To study the field enhancement effect occurring at the ends of the filament wires a code based on time-dependent finite elements is used.

Finally we discuss the implantation of a multifilamentary photocathode in a Diode-RF electron gun which was supposed to be used for the FEL currently being constructed at the Paul Scherrer Institute. However the results of this experiment were not satisfying as electrical breakdown was observed on the cathode. The induced surface damage prevented long term operation.

2.2.1 Samples description

The multifilamentary cathodes are manufactured by the so called bronze route. First, a pure Nb rod is inserted in the hole of a drilled bronze billet which is drawn to a small hexagonal bar. Many such hexagonal bars are then packed together in a copper billet with a Tantalum (Ta) inner jacket. This package is then consecutively drawn to smaller and smaller diameters until the desired filament diameter is reached. The bronze route process results in a wire with a large number of Nb filaments which are almost uniformly distributed in a bronze matrix surrounded by a Ta barrier and a Cu jacket, as shown in Fig.fig. 2.7 (left panel) and fig. 2.8. This is the so called non-reacted wire. It contains several thousands of Nb filaments surrounded by a bronze matrix.

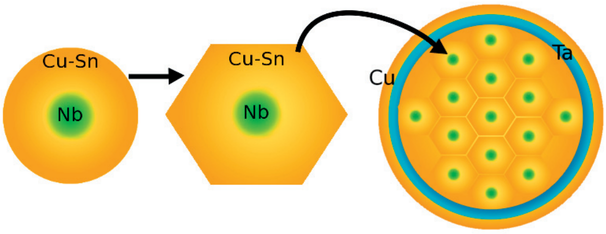

Figure 2.6: (color online) The multi-filamentary wire technology. Many filaments are compacted together to form a multi-filamentary composite wire. After a heat treatment the filaments transform partially in the superconducting compound Nb_3Sn. In a real strand the number of filaments is much larger (10'000-40'000) than showed in the sketch.

The non-reacted wire may be heat-treated to form the Nb_3Sn intermetallic compound (reacted wires), by diffusion of Sn from bronze into the Nb filaments. The standard heat treatment procedure, "‘temperature/time"’ is described by the sequence: 210/50 + 340/25 + 450/25 + 575/100 + 650/200 [in °C/hr]. The result is the so called reacted Nb_3Sn wire which is superconducting below 18.3 K. To avoid bronze formation in the copper jacket of the final cathode the Ta jacket acts as a diffusion barrier against outward Sn diffusion, fig. 2.8. Typical for the bronze route technology is the presence of a small non-reacted Nb core in the center of the Nb_3Sn filaments. This fact makes the reacted wires interesting not only because they are superconducting but also because they offer an additional structure of pure Nb with a diameter smaller than the nominal filament diameter.

The superconducting property of the reacted wire is noteworthy in view of the large currents which could in principle be extracted from such cathode and transported thus without thermal losses. A reacted Nb_3Sn cathode could be a good candidate for a superconducting RF gun operating at 4.2 K. Unfortunately, our electron-gun test facility does not permit testing at low temperatures. At this time the cathodes, either the reacted or the non-reacted ones, were studied only at room temperature.

At the end of the process a wire with 0.8 mm of diameter it is obtained. This wires are cut with a length of several millimeters and one of the surface are mechanically polish. After polishing the samples some of them are treated (etching) in the polished surface with Hydrochloric acid (HCl) removing in the Cu that is surrounding the Nb columns. In total we can obtain four different kind of multifilamentary photocathode: reacted/etched, reacted/non-etched, non-reacted/etched and non-reacted/non-etched.

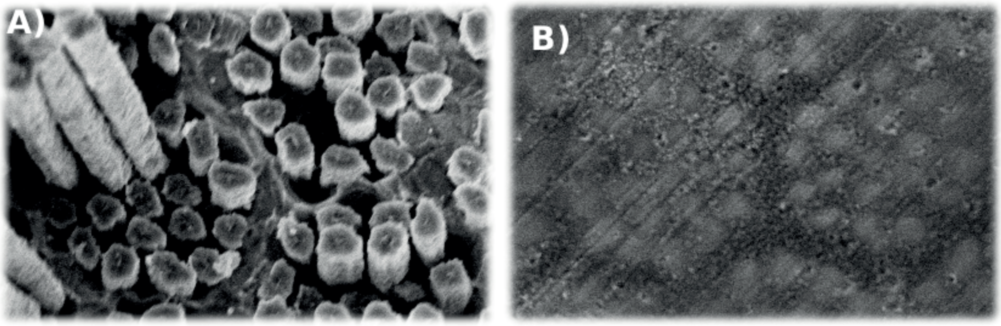

Figure 2.7: A) SEM pictures of an etched cathode withNb_3Sn columns.The typical length of the free-standing columns is several tenth of μm. Some of the colums are broken to visualize the column length (several 10's of μm) B) non-etched, polished cathode.

In order to enhance the electrical field at the filament tips, some of the cathodes tested were etched using HNO_3 acid to remove the bronze core and the Cu jacket over a length of several tenth of μm. This leaves the filaments of Nb (non-reacted wires) or Nb_3Sn (reacted wires) exposed. The difference between an etched and a non-etched wire cathode is shown in fig. 2.7.

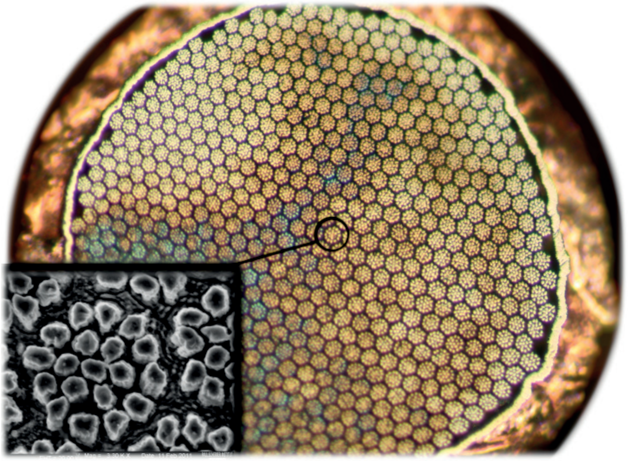

Figure 2.8: (color online). A close-up view to a typical bronze route strand used in our measurements. The wire has 14326 filaments grouped in 754 bunches of 19 filaments each, 6.6 μm in diameter surrounded by a Ta barrier and a Cu stabilizer sheath. A SEM picture of the structure is show on the bottom left.The full diameter of the multi-filamentary cathode is 0.8 mm.

Finally, we have compared the results from our multifilamentary Nb_3Sn cathodes with the one obtained from a Cu cathode wire of the same dimension (0.8 mm) under identical measurement conditions.

2.2.2 Experimental setup

The experimental setup used in the development and characterization of the multifilamentary photocathode can be divided in three different parts: the laser system, the high voltage pulser and the vacuum chamber.

The laser system is a Nd:vanadate mode-locked laser system. The mode-locking is achieved through the use of a saturable semiconductor mirror inside the oscillator cavity that produces a train of 6.2 ps rms pulses at 80 MHz. An acusto-optic modulator (AOM) is used to reduce the repetition rate to 10 Hz prior to the amplifier. The selected pulse is amplified to approximately 40 μJ per pulse. The laser pulses with spectral line centered at 1064 nm are frequency-quadrupled in two consecutive second harmonic generation (SHG) stages reaching a final wavelength of 266 nm with a maximum pulse energy of 12 μJ.

The laser beam size at the cathode position is adjusted between 40 and 200 μm FWHM using a two lense telescope. The beam profile is monitored using a camera placed as the same distance as the cathode. The pulse energy sent to the cathode is adjusted in the range of 2 to 5 μJ using a half-wave plate in combination with a polarizer.

The laser oscillator is frequency-locked to an external reference that produces as well the trigger signal for the high voltage pulser. This high voltage power supply (fig. 2.9) provides pulses with a rise/fall time of 1 ns and a peak voltage of 50 kV. The high voltage is connected to the sample holder via a 500 mm coaxial cylinder whose inner copper diameter (0.7 mm) is surrounded first by a 50 mm diameter insulating ceramic material and finally with a 1 cm bronze layer.

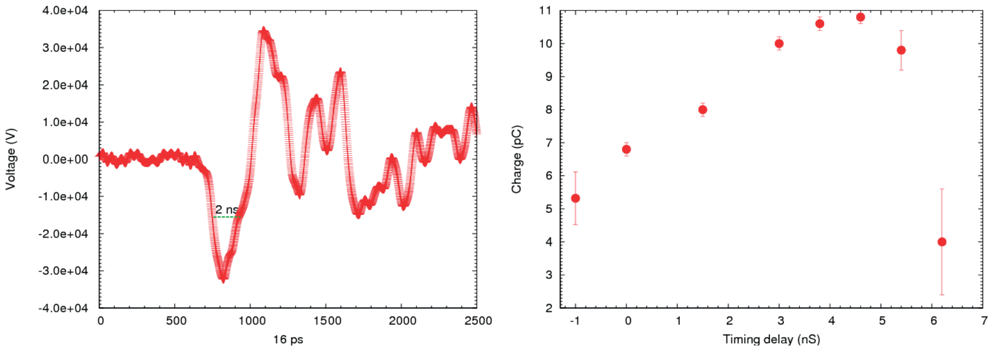

Figure 2.9: Left, temporal profile of the high voltage pulse measured using an high power attenuator and fast oscilloscope. Mapping of the high voltage pulse obtained by measuring the electron charge as function of the time delay of the laser.

The multifilamentary photocathode is inserted into an aluminum support with 1 cm diameter. This support is itself attached to the copper termination of the high voltage feedthrough that is connected to the cathode of the high voltage power supply. This ensemble is covered by an aluminum structure that is acting as anode.

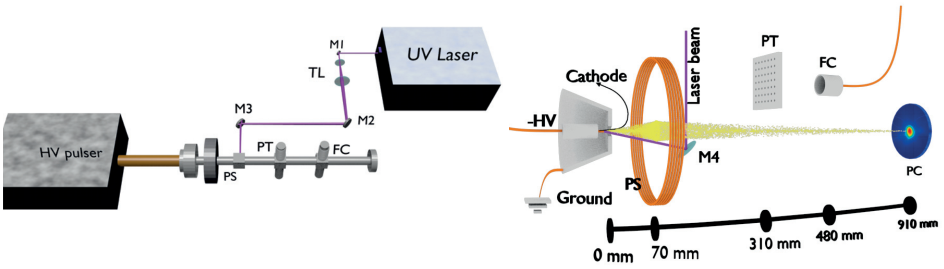

Figure 2.10: Left, scheme of the experimental setup. Right, overview of the electron beam path inside the experimental chamber. M1-4 are UV enhanced aluminum mirror used to steer the laser pulse into the cathode. TL, two lenses telescope, PT is the peeper-pot, FC the Faraday cup, PS the pulse solenoid and PC the phosphor screen.

In the UHV chamber a vacuum ladder is placed at 310 mm from the cathode. In this ladder there two different components: a Ce:YAG screen, used to visualized the electron beam and a tungsten plate with a pepper-pot like pinhole array, used during the emittance measurement. A Faraday cup, used to measure the electron beam charge, can also be inserted at 480 mm from the cathode. The vacuum chamber is closed with a phosphor screen (at 910 mm) allowing to visualize the direct electron beam or the project imaged from the pepper-pot.

The electron beam is controlled by using a solenoid magnet placed at 70 mm from the anode. This magnet provides a magnetic field strength up to 110 mT and allows to focus the electron beam either on the Ce:YAG screen or on the phosphor screen at the end of the chamber.

2.2.3 Charge emission and quantum efficiency

To measure the QE our standard experimental procedure was to monitor the charge emission as function of the laser intensity (power/area) and accelerating voltage for different photocathode samples. The charge values reported here are measured by the Faraday cup without any corrections for cup efficiency. The quantum efficiency (QE) defined as the number of emitted electrons per incident photon was calculated using the following formula:

$$QE = \frac{N_e}{N_{ph}} = \frac{Q}{W}\left(\frac{\hbar\omega}{e}\right) \tag{2.15}$$

where N$_e$ is the number of emitted electrons and N$_{ph}$ the number of incident photons, Q is the total charge, W the laser energy and $\hbar\omega$ the photon energy.

The laser intensity I_{ph} is calculated with the relation :

$$I_{ph} = \frac{W}{\sqrt{2\pi}\sigma_t S_{spot}} \tag{2.16}$$

and is varied by changing the laser spot area on the cathode, S_{spot}. With this definition it is clear that the QE is defined locally within the laser are on the cathode and not relative to the whole cathode surface. Illuminating the entire wire surface (diameter 0.8 mm) is possible but it would be counterproductive from the point of view of emittance decrease. The minimal spot radius (40 μm) is large enough to cover at least three bunches of filaments ($\sim$60 filaments).

The typical charge emitted and QE for an etched, non-reacted Nb$_3$Sn cathode are shown in fig. 2.11 as a function of laser intensity for two laser energies, 2.3 μJ and 4.6 μJ. For each energy, the laser intensity was modified by changing the laser spot-size on the cathode but keeping the laser energy and pulse duration constant. Two different regimes characterized by low-charge and high-charge emission have been observed for all Nb_3Sn wires tested.

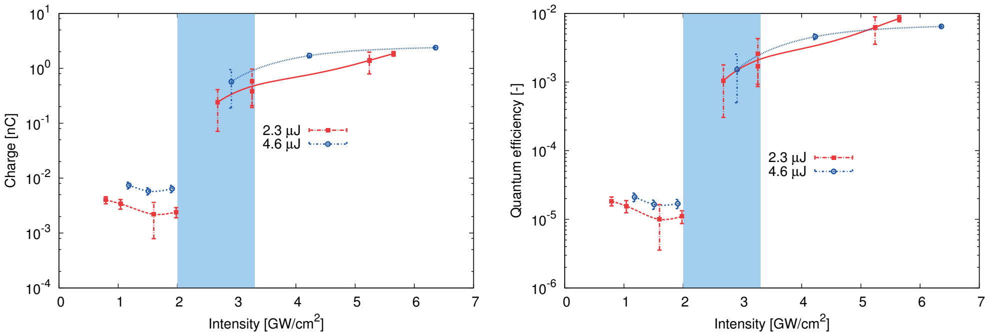

Figure 2.11: Left: charge versus laser intensity for an etched, non-reacted wire at two different laser energies. Right: quantum efficiency versus laser intensity for the same set of measurements. For each energy, the laser intensity is modified by changing the laser spot size and keeping the laser power constant. The blue region marks an unstable operation of the gun between the low and high charge regime as shown by the much larger error bars. The lines are a guide to the eye.

As fig. 2.11 illustrates, in the first regime for laser intensities up to 2 GW/cm^2, the maximum charge extracted is around 30 pC. As expected the charge emitted is higher at higher laser energy; the number of emitted electrons is proportional to the number of photons indicating single-photon emission. Typical for this low-charge regime is the round, symmetric transversal beam-shape as shown in fig. 2.12B.

The QE, shown in fig. 2.11, is on the order of 10^{-5}. These are typical values for metallic photocathodes [36, 37, 38]. Assuming that the charge emission is produced within the laser pulse width, the duration of the charge emission at the cathode is $\tau_b = 2\sqrt{2\ln 2}\sigma_t = 14.57$ ps (FWHM). The beam is emittance dominated, because the laminarity parameter is smaller than one ($\rho < 1$).

The room temperature QEs for the multi-filamentary cathodes with different preparation properties (reacted, non-reacted, etched, non-etched) are very similar as it is shown in fig. 2.12A. The difference between the reacted (superconducting) and non-reacted (normal conducting) wires, if any, are expected to be revealed only at low temperature (4.5 K), when the reacted wire becomes superconducting. We observe a clear difference between the QE of the Nb_3Sn cathodes and the reference Cu cathode (a polished Cu wire of the same diameter as the multifilamentary wire sample). The copper wire has a systematically lower QE, which is more than an order of magnitude smaller for accelerating fields $\geq$40 kV.

We observe a small difference in the QE for the two laser energies used. The explanation is based on the known fact that the field enhancement factor for a cylindrical wire increases from the center reaching a maximum at the wire edge. At higher laser energy,

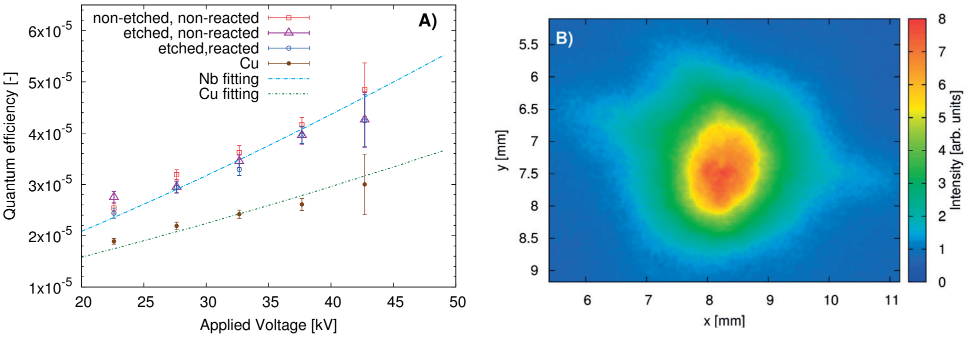

Figure 2.12: Experimental results and numerical fit for the low-charge regime. A) QE versus applied voltage for different cathodes. The numerical calculations for Cu and Nb according to the three-step model are represented by the dashed lines. Fit parameters for Nb are ϕ=4.73 eV, β=2000 m^{-1}, T=1200 K and for Cu ϕ=4.68 eV; β=1800 m^{-1}, T=2000 K. B) electron beam profile recorded at SCR2.

in order to have the same intensity the spot radius must be increased. This results in a larger average enhancement factor. At the lower energy, the spot size is smaller and the enhancement factor is reduced. Therefore we get a larger QE at the higher laser energy.

At intensities larger than 2 GW/cm^2 and less than 3 GW/cm^2, the operation of the gun is unstable. This is characterized by large differences in charge emission from pulse to pulse. The standard deviation is typical 50% but can increase up to 100% and more. At laser intensities higher than $\sim$3 GW/cm^2, the instabiliy disapear and the stable operation is recovered. In this second regime, the extracted charge is in the nC range, a factor 100 increase over that in the first regime. Also the beam transverse profile is no more round as shown in fig. 2.13B. The laminarity parameter ρ is $\sim$ 10 and is calculated using a measured emittance of 0.6 mm·mrad at a charge of 2.5 nC. Accordingly, the beam in the second regime is space-charge dominated. In this high-charge regime the charge emission of the multifillamentary cathode is close to what is usually reached with semiconductor cathodes[38] providing QEs in the order of 0.5%.

In principle, the high-charge regime could be attributed to the explosive electron emission (EEE) [39]. With the same experimental setup, using a sharp ZrC tip (apex of a few tens of nm) [40], the EEE regime starts for power densities above 1 GW/cm^2. A strong erosion of the ZrC tip was observed after a few hours of operation [41]. On the contrary, our Nb_3Sn multifilamentary wires, did not show any sign of damage even after hundred hours of operation and for laser intensities up to 10 GW/cm^2. This indicates that, for the multifilamentary wire cathodes, the driving mechanism responsible for the high-charge regime is not connected to EEE.

To estimate the field enhancement factor for our cylindric wire cathode, we performed an electrostatic simulation for the flat wire tip using a finite element solver. The

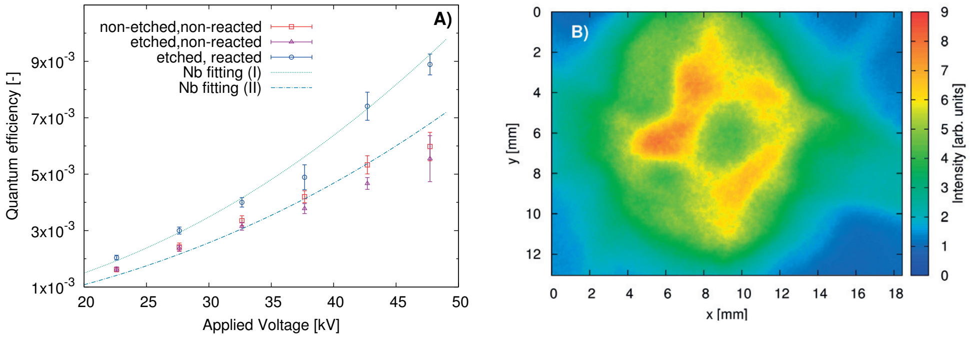

Figure 2.13: Experimental results and numerical fit for high charge regime. A) Quantum efficiency as function of the applied voltage for non-reacted/non-etched and non-reacted/etched samples. The lines represent the numerical results for Nb using the three-step model. Fit parameters for reacted (I) ϕ=4.73 eV, β=150'000 m^{-1}, T=3000 K and for non-reacted (II) ϕ=4.73 eV, β=120'000 m^{-1}, T=3000 K. B) electron beam profile at SCR2, affected by space charge forces.

cylindric wire has a diameter of 0.8 mm with rounded edges (radius 200 nm). In the experimental configuration (tip height of d=3.5 mm) the calculated field enhancement factor is $\alpha \approx 7.5$ (fig. 2.14.), corresponding to $\beta = \alpha/d$ = 2000 m^{-1}.

Additionally we take into account the loss of electrons during propagation from the cathode to the detector, due to the space charge forces, applying a correction proportional to the applyed accelerating voltage i.e. $QE_{fit} = QE_{calc} \cdot V_0/V_{max}$ where V_{max}=50 kV is the maximum voltage of our pulser.

The experimental results were fitted with the equation (2.4) using a calculated density of states for Nb and Cu from FLEUR [1], a freely available FLAPW (Full Potential Linearized Augmented Planewave) code, based on density-functional theory. The integrals were calculated numerically.

The three-step model is well suited in describing our experimental results for the low-charge regime as presented in fig. 2.12 for different cathode materials (solid lines). The experimental data were fitted using the work function, ϕ=4.73 eV and a field enhancement factor β=2000 m^{-1}, similar to previously reported values ([42]). On the contrary, in the high-charge regime fig. 2.13,

we had to assume a significantly larger field enhancement factor in order to fit the experimental data with the three-step model. We need a β=1.2×10^5 m^{-1} and β= 1.5×10^5 m^{-1}, for the non-etched and etched sample, respectively. This is more than a factor of 60 higher that in the low-charge regime.

The apparently very large increase of the field enhancement factor for the high-charge

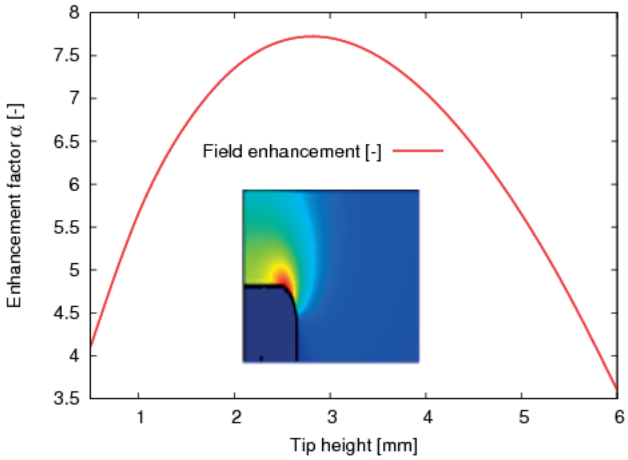

Figure 2.14: Simulated macroscopic field enhancement factor at the center of the Nb_3Sn (location of laser spot) as function of tip height above the support. The inset shows the field enhancement map mimicking a real needle geometry with radius 0.4 mm (only half of the needle cylinder shown), at a tip height of 3 mm. Curvature radius at the edge is 100 μm.

regime, which is not sustained by the sample geometry and is clearly not physical, suggests that plasmonic effect could be at play at the wire surface. The surface roughness with a moderate geometrical field enhancement of the same order as that observed in the low-charge regime ($\beta \sim$2000 m^{-1}), together with a surface plasmon effect can enhance the charge emission at the filament level or even at a smaller length scale, resulting in the large fictitious values of the field enhancement factor from the three-step fit with the Schottky effect included. The fact that plasmonic effect can lead to an enhanced photoelectric effect was predicted and observed in [43].

2.2.4 Emittance measurement

The emittance was measured with a pepper-pot (PPT) made of a stainless-steel foil, 10 mm × 10 mm with a 20 × 20 hole array of 50 μm diameter. The pepper-pot is introduced in the HV chamber by a vacuum ladder where a Ce:YAG screen is also located to be able to see the electron in the peeper-pot plane, as shown in fig. 2.10. The beam image on the phosphor screen placed at the end of the HV chamber at 910 mm, using a 35 keV beam is shown in fig. 2.15(A) for low-charge regime and fig. 2.15(B) for the high-charge regime. In (B) the beam transversal dimensions are larger than the pepper-pot. This is a result of the high-charge in the beam resulting in a large space-charge repulsion and by consequence a large transversal expansion of the electron beam.

In fig. 2.15(B) we observe a central spot which is very bright. This is in good agreement

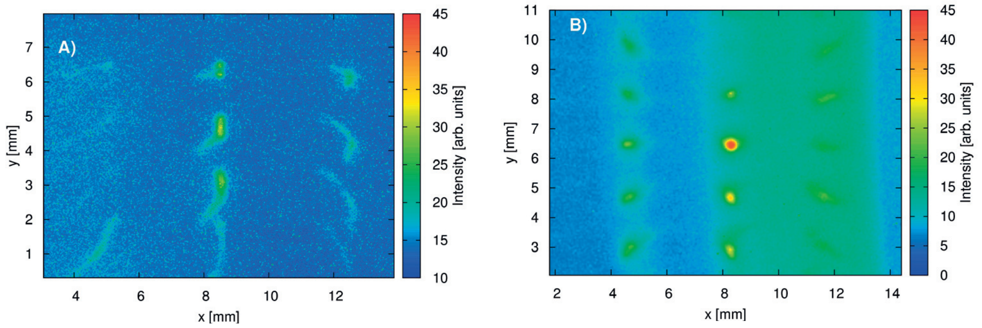

Figure 2.15: Pepper-pot profiles from an electron beam in the low-charge regime (A) with ϵ_n=0.4 mm·mrad and the high-charge regime (B) with ϵ_n=0.6 mm·mrad.

with our particle in cell (PIC) simulations (fig. 2.16) that shows a high charge density, central bullet with a large halo. The PIC simulation mimics the experimental setup with the 35 kV acceleration voltage of a 4 nC charge emitted from a flat Nb wire cathode.

From our measurements, the normalized emittance of the part of the beam intercepting the pepper-pot was calculated, using XanaROOT [44]. We get a value around 0.6 mm·mrad for a beam of 2500 pC i.e in the high-charge regime. This emittance value is a remarkable low value for a picoscond electron beam with a charge in the order of nC. As illustrative example, the nominal emittance value for the SwissFEL photoninjector using a copper photocathode is of 0.4 mm mmrad with a charge of 200 pC. However we are aware of the fact, supported also by the PIC simulations, that the pepper-pot intercepts only a part, i.e. the bullet and not the halo, of the emitted electron beam. In the low-charge regime, for a charge of 30 pC, we measured an emittance of ϵ_n=0.4 mm·mrad. The emittance in this case is surely overestimated due to the blur produced by the the long integration time needed to obtain a good signal/noise ratio.

Emittance conservation for a sub-relativistic electron beam during the propagation over the long distance from the cathode to the pepper-pot is challenging. The ejected electron bunch at the cathode is short due to the picosecond (σ_t=6.2 ps) laser pulse used for electron emission. Due to the space-charge forces the electron beam expands longitudinally and transversely during the beam propagation to the peeper-pot (PT) and spoil the electron beam emittance, especially in the high-charge regime. The longitudinal expansion of the beam, due to the longitudinal space-charge forces, could be suppressed by using a higher acceleration gradient, like the typical fields encountered in an RF-gun ($\sim$100 MV/m). In fig. 2.16 the particle in cell (PIC) simulation shows the beam expansion due to the space charge forces acting on a 4 nC electron bunch. Soon after ejection at the source the electron bunch breaks apart into several parts. The simulation indicates the formation of a central bullet with a high charge density and kinetic energy followed by two heavily space-charge dominated sub-bunches at lower energy.

The beam optics in our experiment has been set to transport the high-energy part of the beam towards the PPT for emittance characterization. The emittance measurement presented in fig. 2.15(B) is attributed to the on-axis bullet observed in the simulation. Clearly observable is also the background caused by the trailing electrons (green, yellow colorcode) which suffer from emittance blow up.

From the presented measurements of charge and emittance one can estimate the transversal electron beam brightness, B_n as

$$B_n = \frac{I_p}{4\pi^2\epsilon_n^2} = 10^{13} A/(rad^2 \cdot m^2) \tag{2.17}$$

with $I_p = Q/\sqrt{2\pi}\sigma_t$ is the peak current, ϵ_n the normalized emittance and under assumption of the electron bunch length being equal to the laser pulse duration. This assumption is valid only in the vicinity of the cathode, since space charge forces expand the electron bunch significantly upon propagation (fig. 2.16). With this emittance value together with the high charge of the electron beam makes this kind of photocathode a very promising source for applications where high brightness electron beam are required.

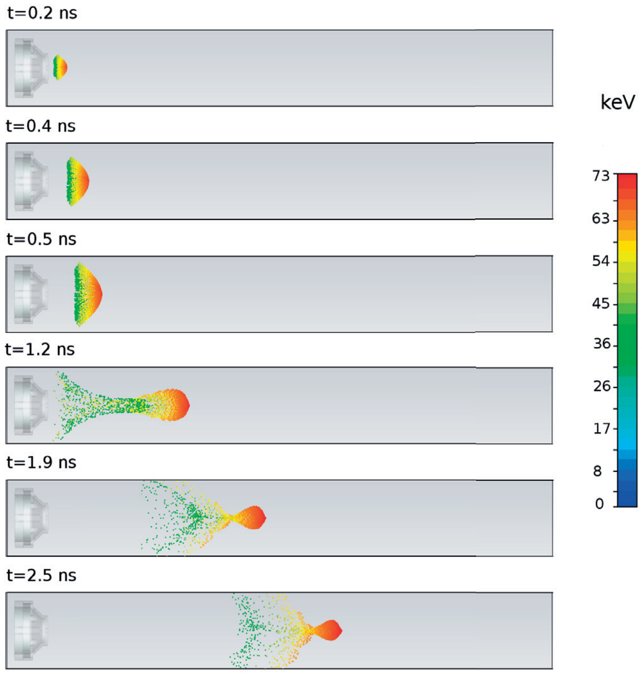

Figure 2.16: Particle in cell simulation for electron beam propagation across the beamline shown in fig. 2.10. Due to space charge forces the 4nC electron beam splits into several sub-bunches of different energies towards the end of the beamline. The drift region is 610 mm long.

2.3 Conclusions and outlook

A new kind of metallic multifilamentary needle-photocathode with a microstructured surface has been investigated. This cathode combines the fast response of metallic cathodes with a QE comparable with that of some semiconductor photocathodes.

Two emission regimes have been observed. The first one is at low laser intensities of up to 2 GW/cm^2 and is characterized by values of QE typical for metallic photocathodes. It is well explained by the three-step model including Schottky effect and a moderate (β=2000 m^{-1}) field enhancement at the tip. The second regime with a QE two order of magnitude higher (up to 0.5%) appears at laser intensities on the order of 3 GW/cm^2. In spite of the large extracted charge (up to 4.8 nC), high current density and large laser intensity, no laser ablation was observed after hundred of hours of continuous operation at 10 Hz. In this regime the three step model could be fitted to the experimental results only by using a very large field enhancement factor, $\beta \sim 10^5$, pointing towards possible plasmonic effects.

Operation of the multifilamentary wire cathode in a 3 GHz (100 MV/m) RF photogun is the next step towards a full characterization of this new type of cathode [45]. At

3 GHz the equivalent pulse time for the high gradient would be below the ns range, although the RF pulse length can be up to one microsecond long. We believe that stable operation in such environment is possible giving the short time in which the high field is present on the surface of the cathode.

Applications like free electron lasers, ultrafast electron diffraction, as well as linear colliders, can benefit from this new electron source with high brightness. In a free electron laser, the gain length ($L_g \propto B^{-1/3}$) could be reduced using this kind of sources with increased brightness B, as compared to the typical value for a RF photogun.

Up to now our research has not explored the superconductive properties of these photocathodes. In the superconductive phase, an enhancement of the QE can be expected due to the reduction of the electron-electron scattering length. Also, we have investigated only one technological superconductor: $\mathrm{Nb_3Sn}$ known as low-T$_c$ superconductor. The are as well others technological superconductor, like NbTi has a similar multifilamentary structure but was not investigated in the frame of this work. Recently, new superconductor compounds known as high-T$_c$ are technologically available but their multifilamentary structure is less developed. Nevertheless, their investigation is of great interest due to the expected special photoemission properties of the basic materials associated to their 2D structure.

3 High-order harmonic generation

Contents

In 1875 using the Crookes tubes, Pulyui and Röntgen made the first empirical observation of X-rays radiation. In the Crookes tubes, X-rays are generated by the bremsstrahlung of electrons that have been generated by thermal emission and accelerated to KeV energies by a DC electric potential. Since that day, many efforts have been made to develop different types of X-ray sources.

Some of these x-ray sources rely on particle accelerators. For example, in 1956 Tomboulian and Hartman confirmed the theoretically predicted radiation losses of bending magnets by means of a 320 MeV synchrotron facility. Using this radiation they reported the first experiments on soft X-ray spectroscopy. The recent developments of high brightness and low emittance electron beams have made possible the development of FELs. Modern FELs generate X-ray pulses with wavelength down to 0.1 Å at pulse durations variable between tens to hundreds of femtoseconds with pulse energies up to a few mJ [46].

Particle accelerators are not the only source of X-rays. It has been shown that X-rays can be produced in a similar way that is used in optical lasers by exciting an inner shell transition in an atomic gas media. However, X-ray lasers based on amplification from stimulated emission are difficult to scale up in power as they suffer from a dramatic increase of power to produce higher gain in the media. An example of this kind of laser was the project ExCalibur [47] that aimed to produce an X-ray laser, pumped by nuclear reaction, powerful enough to destroy ballistic missiles.

In 1987 McPherson [48] and later on Ferray [49] found during some studies on multiphoton ionization that a series of higher-order harmonics were generated when a gas media was exposed to a high intensity laser. The high-order harmonic generation (HHG) spectrum can be divided into three regions well differentiated:(1) the perturbative regime, where the intensity of the harmonics is decreasing with the harmonic order. (2) the plateau region where the HH intensity remains constant up to many orders and (3) the cut-off region where the HHG generation process terminates. In principle this observation could be attributed to some non-linearities in the gas medium however, the existence of a plateau region in the HHG intensities indicates that the generation process is a non-pertubative phenomenon in contrast with other non-linear processes.

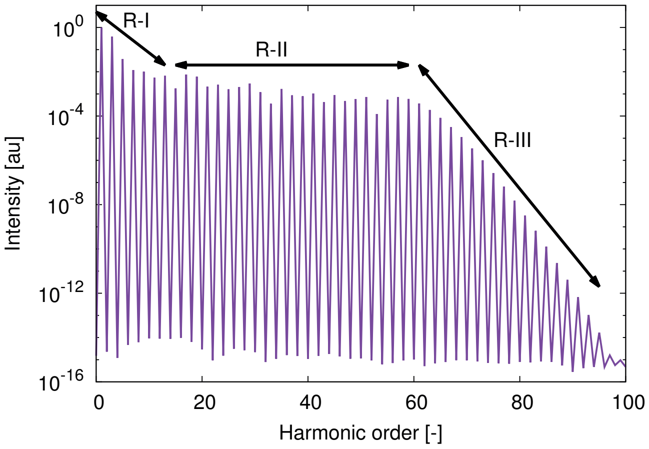

Figure 3.1: Typical HHG spectrum. R-I is the initial exponential decay, R-II is the plateau region and R-III the final decay after the cut off.

In 1993, Corkum [50] proposed a theoretical model to explain this novel kind of radiation. In this so-called 3 step model the electron is released from the parent ion into the continuum due to tunneling ionization (step 1), is accelerated in the electric field of the driving laser and gains kinetic energy (step 2) before it finally recombines with the parent ion emitting the excess of kinetic energy as a photon (step 3) (fig. 3.2).

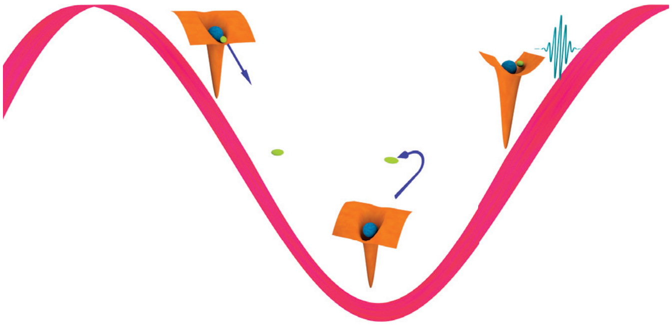

Figure 3.2: Sketch of the three step model proposed by Corkum. The initially bound electron is released into the continuum by tunnel during the first half of the laser cycle. It gains kinetic energy in the electric field and finally recombines during the second half of the laser cycle.

The properties of HHG make them a unique source of X-rays. The extremely large spectrum, for example, allows the production of the shortest ever measured light pulses in the attosecond domain [21]. Furthermore, these pulses are intrinsically synchronized to the femtosecond driving laser making them an ideal tool for probing ultrafast dynamics.

In this chapter developments of an HHG source are described. The source has been set up from scratch in order to serve for various applications ranging from seeding the soft X-ray beamline at SwissFEL to probing ultrafast magnetic process. In the first section, the fundamental aspects of HHG are presented both from an atomic and macroscopic point of view. In the second section, we present details about the HHG beamline developed at the Paul Scherrer Insitute and the laser system, followed by a detailed characterization of the HHG source and developments towards the expansion of the HHG spectrum into water window spectral region.

3.1 Theory of high-order harmonic generation

It is well known that the correct framework to describe atomic processes such as ionization or recombination that are part of high harmonic generation is quantum mechanics. However the classical treatment of the electron dynamics in the electric field of a laser helps to understand most of the fundamental aspects of the high-order harmonic generation process. Lets start considering the Lagrangian of an electron in a time dependent electric field:

$$L = \frac{1}{2}m\dot{\mathbf{r}}^2 + e\dot{\mathbf{r}} \cdot \mathbf{A} - e\phi \tag{3.1}$$

with $\mathbf{A}$ the electromagnetic vector potential and ϕ the electric potential. Using the canonical momentum ($p_i = \frac{\partial L}{\partial \dot{r_i}}$) one can use the Legendre transform to obtain the Hamiltonian of the system:

$$H = \mathbf{r}\mathbf{p} - L = \frac{(\mathbf{p} - e\mathbf{A})^2}{2m} + e\phi \tag{3.2}$$

In our case we consider a vector potential given by $A(t) = -\frac{E_0}{\omega} sin(\omega t)\hat{x}$ and $\phi = 0$. The equations of motion are thus:

$$\frac{\partial x}{\partial t} = \frac{\partial H}{\partial p_x} = \frac{p_x - eA_x}{m} \qquad \frac{\partial p_x}{\partial t} = -\frac{\partial H}{\partial x} = 0 \tag{3.3}$$

using the initial conditions $v(t_0) = 0$ and $x(t_0) = 0$ we obtain

$$v(t) = \frac{eE_0}{m\omega}[sin(\omega t) - sin(\omega t_0)] \tag{3.4}$$

$$x(t) = \frac{eE_0}{m\omega^2}\left[cos(\omega t) - cos(\omega t_0) + (\omega t - \omega t_0)sin(\omega t_0)\right] \tag{3.5}$$

From these euqtions one can calculate the recombination phases ($\phi_r = \omega t_r$) as function of the ionization phases ($\phi_0 = \omega t_0$) by finding the roots of $x(t)$. Figure 3.3 illustrates that only for a birth point at phase $0 \leq \theta_i \leq \frac{\pi}{2}$ the electron is capable to return to the parent ion. However for $\frac{\pi}{2} < \theta_i < \pi$ the electron can not return to the parent ion.

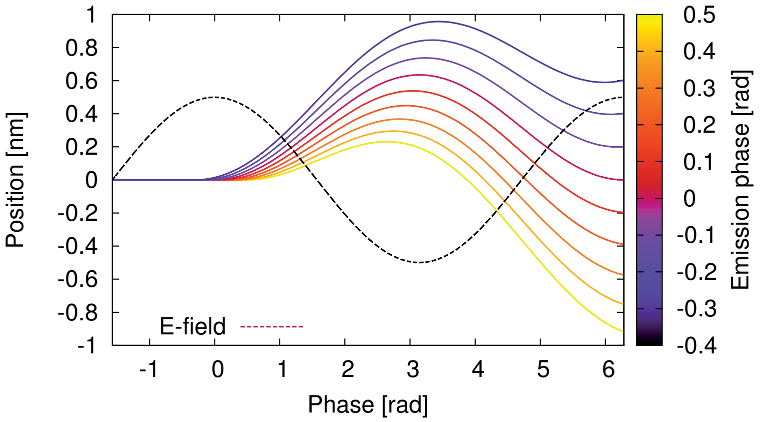

Figure 3.3: Electron trajectories in a cosine electric field as function of the emission phase.

The classical model presented above gives also valuable information about the maximum kinetic energy of an electron upon returning to its parent ion. Figure 3.4 shows the electron kinetic energy as function of the ionization phase. Two different kinds of trajectories can be observed:(1) trajectories with an excursion time of less than half an optical cycle (i.e. short trajectories) and (2) trajectories with an excursion time larger than half of an optical cycle (i.e. long trajectories). The maximum kinetic energy the electron can gain results in the highest photon energy released by HHG. This relation can be expressed in the following cut-off law:

$$E_{cut-off} = I_p + 3.17U_p = I_p + 3.17\frac{e^2E^2\lambda^2}{16\pi^2mc} \tag{3.6}$$

where I_p is the ionization potential of the parent atom, U_p the ponderomotive energy, E the peak electric field of the laser, λ the wavelength of the laser, m, e are the mass and charge of the electron and c the speed of light in vacuum.

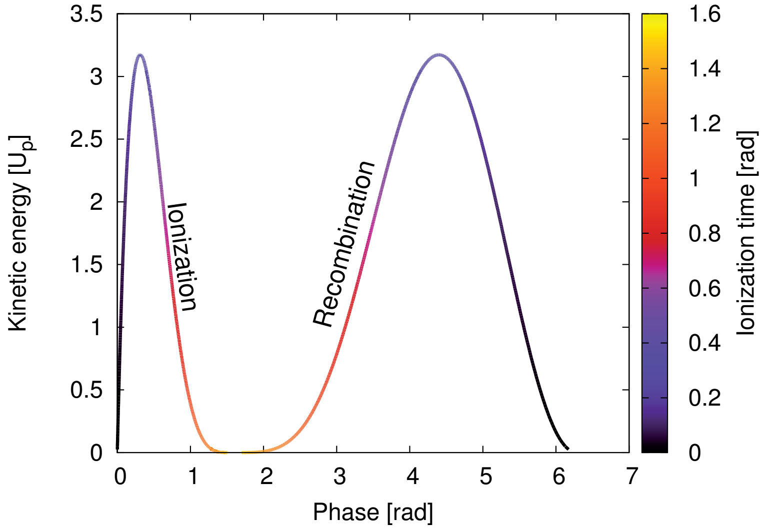

Figure 3.4: Electron kinetic energy as function of the ionization time (phase). Left side curve and fals color correspond with the ionization phases. Right side curve shows the recombination phase.

We conclude that the framework of classical mechanics is sufficient to get information about the maximum photon energy and emission times allowing the electron to recombine with the parent ion. However as mention before classical mechanics cannot give us any information about the ionization and recombination processes occurring in the high-order harmonic generation. In order to obtain a more complete picture the process has to be described by quantum mechanic.

3.1.1 Single atomic response

We use quantum mechanics to obtain more information about the single atomic response of the HHG process. Here we follow the calculations performed for the first time by Lewenstein et al. [51]. Along this analysis we will assume the Strong Field Approximation (SFA) [52]. The main assumptions of the SFA are the following.

- For the description of the atomic system only the ground state is taken into account.
- The population of the ground state is constant and equal to one.
- Once the electron is released it is consider as a free particle. Meaning that is not affected by the atomic potential.

Now that the initial framework has been defined, we can start with the Schrödinger equation of an hydrogenic atom (single active electron) under the action of a sinusoidal time-dependent electric field.

$$-i\hbar\frac{d}{dt}\left|\psi(\mathbf{r},t)\right\rangle = \left[-\frac{\hbar^2}{2m}\nabla^2 + V(r) + A(t,\mathbf{r})x\right]\left|\psi(\mathbf{r},t)\right\rangle \tag{3.7}$$

where $|\psi\rangle$ is the electron wavefunction, $V(r)$ the atomic potential and $A(t,\mathbf{r})$ the vector potential of the laser. From now on we will use atomic units ($e = \hbar = c = m_e = 1$). By employing the first approximation of the SFA the wavefunction can be written as

$$\left|\psi(\mathbf{r},t)\right\rangle = e^{iI_pt}\left(a_0(t)\left|0\right\rangle + \int d^3\mathbf{v}b(\mathbf{v},t)\left|\mathbf{v}\right\rangle\right) \tag{3.8}$$

where $|0\rangle$ is the atomic ground state, $a(t)$ the ground state population and $|\mathbf{v}\rangle$, $b(\mathbf{v},t)$ the continuum state and its probability with velocity $\mathbf{v}$, respectively.

Inserting this solution into (3.7) and considering $a(t) = 1$ (SFA) we obtain the following equation for $b(\mathbf{v},t)$:

$$\dot{b}(\mathbf{v},t) = (-i\frac{1}{2}v^2 + I_p)b(\mathbf{v},t) = -A(t)\frac{\partial b(\mathbf{v},t)}{\partial \mathbf{v}} + iA(t)\mathbf{d}(\mathbf{v}) \tag{3.9}$$

where $d(\mathbf{v})$ is the probability of the transition bound-free electron along the polarization axes, in the case of hydrogenic atom in the ground state is given by:

$$\mathbf{d}(\mathbf{p}) = \frac{i8\sqrt{2}(2I_p)^{5/4}}{\pi}\frac{\mathbf{p}}{(p^2+2I_p)^2} \tag{3.10}$$

This differential equation has the exact solution

$$b(\mathbf{v},t) = i\int_0^t dt' Ecos(\omega t)\mathbf{d}(\mathbf{v} + \mathbf{A}(t) - \mathbf{A}(t'))\, exp\left[-iS(\mathbf{p},t,t')\right] \tag{3.11}$$

where $\mathbf{p(t)}$ is the canonical momentum defined as $\mathbf{p} = \mathbf{v} + \mathbf{A}(t)$ and $S(\mathbf{p},t,t')$ is the semi-classical action given by:

$$S(\mathbf{p},t,t') = \int\limits_{t'}^{t} dt'' \left(\frac{[\mathbf{p}-\mathbf{A}(t'')]^2}{2} + I_p \right) \tag{3.12}$$

we can now calculate the expected value $x(t) = \langle \Psi(t) | \, x \, | \Psi(t) \rangle$ introducing (3.11) into (3.8):

$$x(t) = \int\limits_{-\infty}^{t} dt' \int d^3\mathbf{p} \, d(\mathbf{p}+\mathbf{A}(t)) \, exp\left[-iS(\mathbf{p},t,t')\right] \, \mathbf{E}(\mathbf{t}') \, d(\mathbf{p}+\mathbf{A}(t')) + c.c. \tag{3.13}$$

Within the three step model this equation can be interpreted as follows:

- $E(t') \, d(\mathbf{p}+\mathbf{A}(t'))$: Ionization probability at time t'
- $exp\left[-iS(\mathbf{p},t,t')\right]$: Propagation in the laser field from t' to t
- $d(\mathbf{p}+\mathbf{A}(t))$: Recombination with the parent ion at time t.
- $\int\limits_{-\infty}^{t} dt'$: Integration over all possible ionization times.
- $\int d^3\mathbf{p}$: Integration over all possible trajectories from t' to t.

We can now calculate the Fourier transform of $x(t)$:

$$x(\omega_k) = \int\limits_{-\infty}^{\infty} dt \int\limits_{-\infty}^{t} dt' \int d^3\mathbf{p} \, d(\mathbf{p}+\mathbf{A}(t) \, exp\left[i\omega_k t - iS(\mathbf{p},t,t')\right] \, \mathbf{E}(\mathbf{t}') \, d(\mathbf{p}+\mathbf{A}(t')) + c.c. \tag{3.14}$$

The semi-classical action $S(\mathbf{p},t,t')$ provides the probabilities for the different electron trajectories in the continuum.By finding the stationary points of this action, we obtain the electron trajectories with highest probability. The stationary points of this semi-classical action fulfill the following conditions:

$$\frac{\partial S}{\partial \mathbf{p}} = p(t-t') + \int_{t'}^{t} dt\text{"}A(t\text{"}) = 0 \tag{3.15}$$

$$\frac{\partial S}{\partial t} = \frac{[p+A(t')]^2}{2} + I_p = 0 \tag{3.16}$$

$$\frac{\partial S}{\partial t'} = \frac{[p+A(t')]^2}{2} + I_p - \omega_k = 0 \tag{3.17}$$

Applying now the stationary phase approximation to the integrals of (3.14) we obtain a sum over all the possible trajectories that are stationary point of the semi-classical action:

$$\begin{aligned} x(\omega_k) = \sum_s \left(\frac{\pi}{\epsilon + \frac{i}{2}(t_s - t'_s)} \right)^{3/2} & \frac{i2\pi}{\sqrt{det|s(t,t')|_s}} d(\mathbf{p}_s + \mathbf{A}(t_s)) \\ & \times exp\left[i\omega_k t_s - iS(\mathbf{p}_s, t_s, t'_s) \right] E(t'_s) \mathbf{d}(\mathbf{p}_s + \mathbf{A}(t'_s)) \end{aligned} \tag{3.18}$$

where the term $det|s(t,t')|_s$ is given by:

$$det|s(t,t')|_s = \left(\left. \frac{\partial^2 S}{\partial t \partial t'} \right|_s \right)^2 - \left. \frac{\partial^2 S}{\partial t^2} \right|_s \left. \frac{\partial^2 S}{\partial t'^2} \right|_s \tag{3.19}$$

Using (3.18) we can calculate the HHG spectrum generated by the dipole response of a single atom (fig. 3.5). However due to approximations made in the calculation some effects are not taken into account. For example it's well know that Argon presents a minimum in the photo-ionization cross-section around 50 eV (Cooper minimum) [53]. Since this process can be view as the opposite for the electron recombination, the HHG in Argon presents as well a minimum on the spectral intensity around this energy.

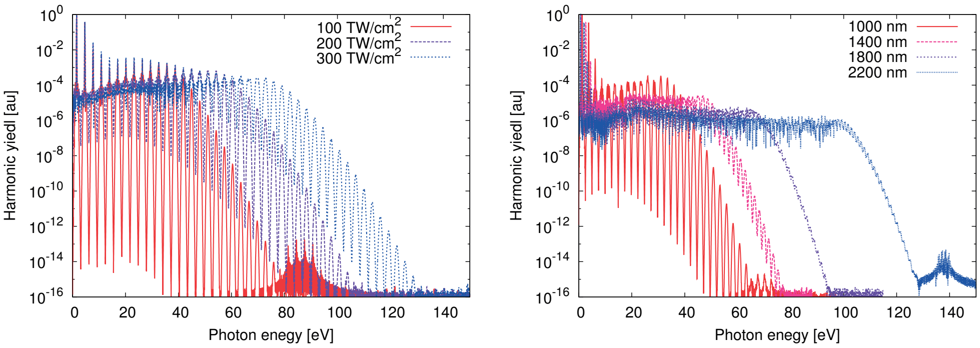

Figure 3.5: Left: spectral response of a a single atomic dipole as function of the laser intensity for a 45 fs, 800 nm driving laser . Right: spectral response as function of the driving laser wavelength. Pulse duration is 45 fs and a peak intensity of 50 $\frac{TW}{cm^2}$.

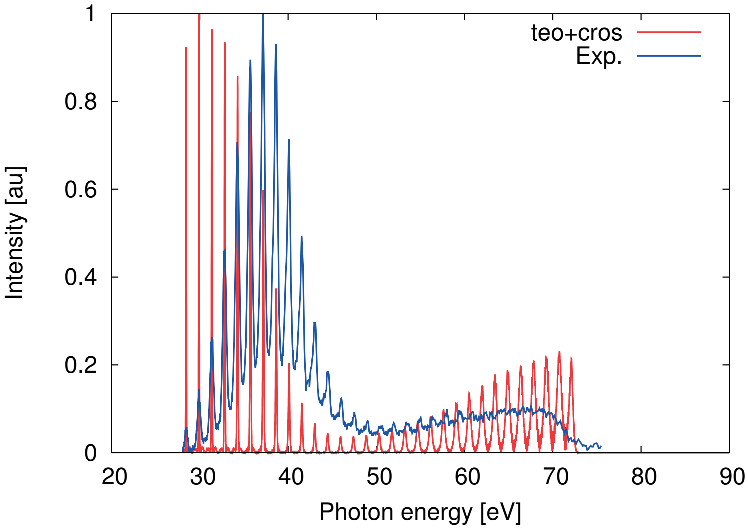

Figure 3.6: Comparison of a calculated and an experimentally measured HHG spectrum taking into account the ionization cross-section of the generation media as well as the transmission of a 200 nm thick Aluminium filter.

In fig. 3.6 we compare a HHG spectrum measured in our experimental setup with a calculated one taking in to account the minimum for this recombination cross-section. More precisely, since the values for the photo-ionization cross section where not available for this energy range, we used the inverse value of the absorption coefficient (k)[54]. The use of the inverse of the absorption coefficient is justified since lower cross-section entails large transmission.

3.1.2 Phase matching conditions

In the previous section we have presented an overview of the HHG process at the atomic level. However to obtain a full overview of the process we need to know as well how to coherently combine the radiation emitted from the different atoms. In other words, to efficiently generate high-order harmonics, phase matching between the fundamental laser and the generated radiation must be achieved, preferably along an elongated distance to enhance the high harmonic yield.

Different physical mechanisms are present in HHG that can cause a phase mismatch between the driver laser and the generated harmonics. These contributions have either a geometrical origin and depend on the generation scheme, depend on the generation medium or are intrinsic to the HHG process itself. The various contributions are listed below [55, 56].

The first mechanism is the chromatic dispersion originating from a neutral atom:

$$\Delta k_n = \frac{2\pi q}{\lambda} P \Delta\delta \left(1-\eta\right) \tag{3.20}$$

where q is the harmonic order, λ the wavelength of the driving laser, $\Delta\delta$ the difference in the refractive index between the driver and the high order harmonics, P the gas pressure and η the ionization level of the gas medium.

The second contribution originates from the dispersion the drive laser accumulates by passing through a region with free electrons caused by laser-induced ionization of the gas medium. The corresponding phase mismatching is given by

$$\Delta k_f = -qP\eta \left(N_{atm} r_e \lambda\right) \tag{3.21}$$

with N_a the atomic density of the gas and r_e the radius of the electron.

The third term originates from the laser geometry in the focus. For a non-guided laser beam this contribution is dominated by the Gouy phase:

$$\Delta k_{gG} = \frac{-q}{1+\frac{z^2}{z_0^2}} \tag{3.22}$$

Where z_0 is the position of the beam waist. In the case of HHG in a capillary waveguide this term is given by:

$$\Delta K_{gC} = q\frac{u_{11}^2 \lambda}{2\pi a^2} \tag{3.23}$$

where u_{11} is the geometrical factor for a TEM00 coupling and a the radius of the capillary waveguide.

Finally the HHG process adds a contribution itself due to the intrinsic atomic phase acquired during the generation process, this contribution is given by:

$$\Delta k_d = -\theta \nabla I \tag{3.24}$$

Where θ is the slope constant of the intrinsic atomic phase. However as discussed in [55] $\Delta k_d \sim 0$ if the generation area is centered around the focal point.

In the following we discuss more indepth HHG phase matching conditions in capillary waveguides [55, 57]. The dispersion characteristics in capillary waveguides offer an additional knob to to achieve better phase-matching between HHG and the driving laser. For the case of capillary waveguides we can re-arrange the different terms of eq. (3.20), eq. (3.21) and eq. (3.23) and obtain the following expression:

$$\Delta k = \frac{q u_{11}^2 \lambda_L}{2\pi a^2} - qP\left[\frac{2\pi}{\lambda_L}(\Delta\delta) - \eta\left\{\frac{2\pi}{\lambda_L}(\Delta\delta) + N_{atm} r_e \lambda_L\right\}\right] \tag{3.25}$$

this arrangement of terms allows us to find the conditions to achieve perfect phase matching for the whole HHG spectrum by choosing the optimum gas pressur for a given η. For this reason we can define a critical ionization fraction η_{cr}

$$\eta_{cr} = \frac{2\pi\Delta\delta}{2\pi\Delta\delta + r_e N_{atm} \lambda_L^2} \tag{3.26}$$

For an ionization level below η_{cr} the phase mismatch caused by the neutral gas can always be compensated by the corresponding contribution from the electron gas.

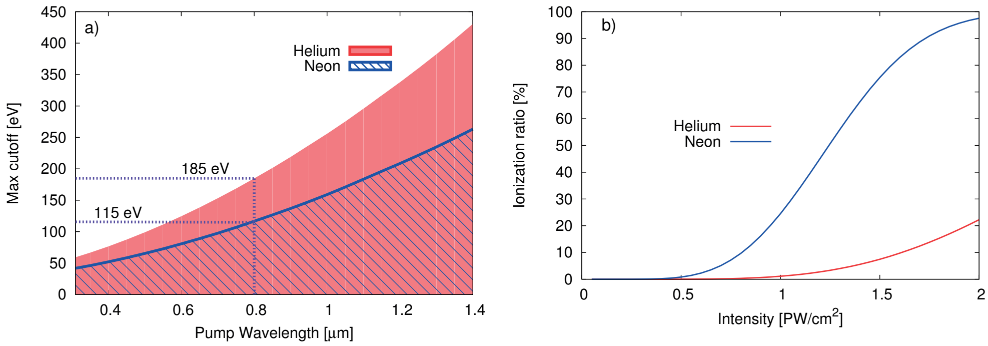

Figure 3.7: Left: maximum HH cut off energy in He and Ne for fully phase matched HHG in a capillary, as function of the laser wavelength. Right: Corresponding ionization ratio versus laser intensity for He and Ne.

Using (3.26) together with the ADK model [58] and the cut-off law (3.6) it is possible to estimate the maximum photon energy that is possible to achieve within the phase matching condition. Figure 3.7 a) illustrates this maximum photon energy as function of the wavelength of the driving laser using He and Ne as generation media. For Ti:sapphire lasers emitting at 0.8 μm the maximum photon energy is 185 eV (6.7 nm) in He and 115 eV (10.8 nm) in Ne, respectively. Harmonics above this maximum energies (indicated by the red and blue line for He and Ne, respectively) are not fully phase-matched and increasing the pressure will further decrease the harmonic yield. In the red region phase-matching of HH can only be achieved in He while in the blue region full phase matching can be achieved for He and Ne. For a given laser intensity defining the fraction of ionization and thus the maximum reachable HH cutoff energy, the gas pressure needs to be adapted adequately in order to achieve full phase matching.

An experimental study of the phase matching conditions for capillary waveguides is shown in fig. 3.8. For this experiments a Ti:Sa laser system delivering pulses with up to 6 mJ, 40 fs (FWHM) with a repetition rate of 1 kHz. The pulses are focused with a lens (f=1.5 m) into a 33 mm long capillary with 200 μm of diameter. The capillary is flodded continuously with Neon or Helium. A maximum laser intensity of $7 \cdot 10^{14} \frac{W}{cm^2}$ is achieved in the capillary waveguide. The graphs show the evolution of high harmonic spectra as function of gas pressure. For Neon and with intensities of $7 \cdot 10^{14} \frac{W}{cm^2}$ we are above the critical ionization ratio and increasing the pressure the efficiency of the HHG process it decreased. For Helium, on the other hand, we are correspondingly below the critical ionization ratio and increasing the pressure results in an improved phase matching, particularly for the higher-order harmonics.

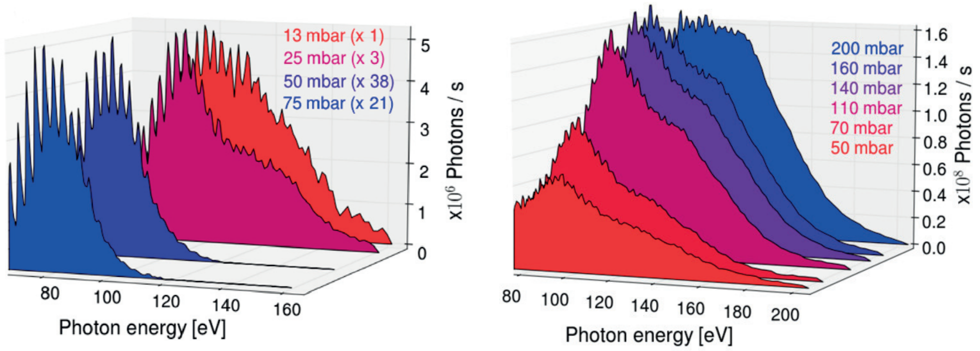

Figure 3.8: Evolution of the HHG spectrum as function of the gas pressure for Neon (left) and Helium (right). The total photon flux is estimated using the count numbers in the CCD and the calculated transmission of the HHG beamline.

3.2 Source development

3.2.1 Laser system

The laser system used to drive the high-order harmonic generation is a 100 Hz commercial Ti:Sapphire CPA laser from Amplitude Technologies. Here we will highlight the main characteristics of the system. A more detailed description is given in [59].The front end of the system consists of a broadband CEP stabilized oscillator, a booster amplifier, a low drift grating stretcher, a regenerative amplifier, a high-power amplifier followed by a grating-based compressor. The pump lasers used in this front end are four diode-pump solid-state (DPSS) ND:YAG laser (Quantel-centurion) each of them delivering 20 mJ, 500 ps pulses. The system also inlcudes a Dazzler for spectral phase adjutment and a Mazzler to perform spectral broadening and shaping in the regenerative amplifier (fig. 3.10).

Figure 3.9: Schematic of the laser system used for HHG.

After the high power amplifier stage the beam is divided in three parts (50%-25%-25%) seeding three different amplifiers. Two of these amplifiers are pump by two flash-lamp based Nd:YAG pump lasers (Nano TRL, Litron) and deliver compressed pulses with energies up to 20 mJ with a repetition rate of 100 Hz. The other amplifier delivers compressed pulses with energies up to 40 mJ. The compression of each amplifier output is performed in broadband compressors which support pulse durations down to 16 fs (FWHM). The high energy output is used to pump an Optical Parametric Amplifier (OPA). The three amplification stages provide energies up to 10 mJ (signal + idler). Figure 3.11 shows the pulse energy as function of the OPA wavelength.

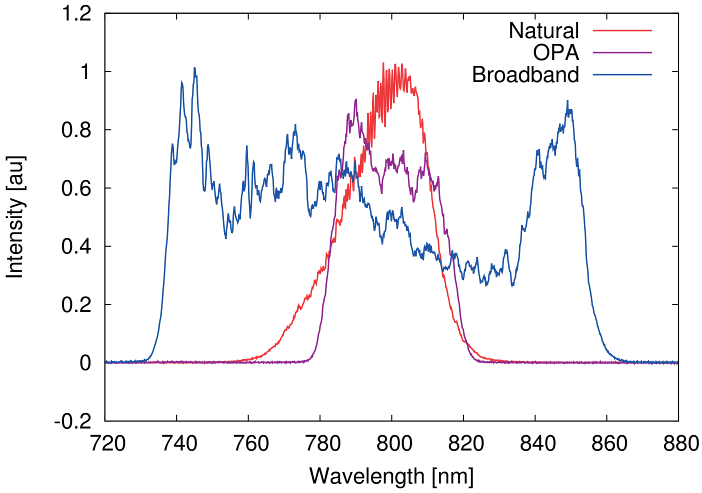

Figure 3.10: Typical spectrum of the laser system, in red natural spectrum (no losses introduced), purple spectrum used to drive the OPA and blue the spectrum used in the short pulse mode.

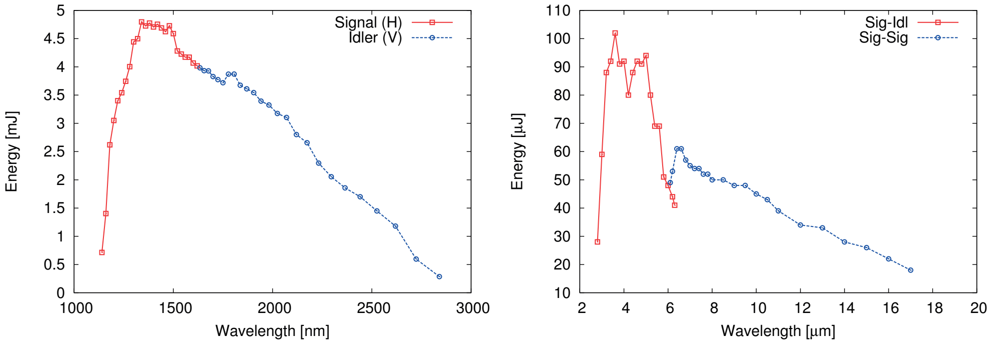

Figure 3.11: Left: wavelength dependence of the high energy output of the OPA. In red (blue) the signal (idler) with horizontal (vertical) polarization. Right: wavelength dependence of the DFG energy for the output of the OPA.

3.2.2 HHG beamline

The HHG beamline (fig. 3.12) consists of a set of vacuum chambers distributed along 10 meters which are designed for ultra high vacuum (UHV) conditions. Inside of each chamber there is a stainless steel optical breadboard which is decoupled from the chamber in order to minimize vibrations originating from the vacuum system.

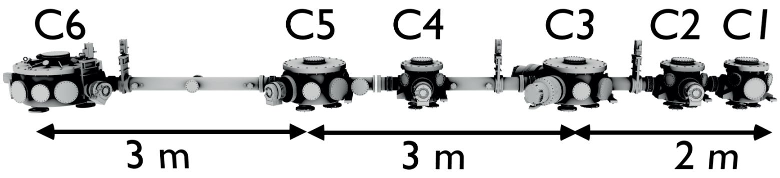

Figure 3.12: Scheme of the vacuum chamber of out HHG beamline. Chambers 1, 2 and 4 have a diameter of 400 mm, chamber 3 and 5 has 600 mm each one and for chamber 6 has 800 mm of diameter.

The first two vacuum chambers host the optical beam path and the focusing optic for the driving laser. The chambers are large enough to host different configurations, such as a two-color scheme in order to perform HHG in a $\omega + 2\omega$ field. In the third chamber, the high-order harmonics are generated using a target that consists of a bi-conical gas cell or a glass capillary (fig. 3.13). These targets are attached to a pulsed valve using a stainless steel mount. The entire valve is mounted on a 5-axes positioning stage for fine positioning in all 3 dimensions (x,y,z) as well as to adjust the two tilting angles (θ_x, θ_y). In addition a long translation stage allows to position the target along the propagation direction of the laser (z).

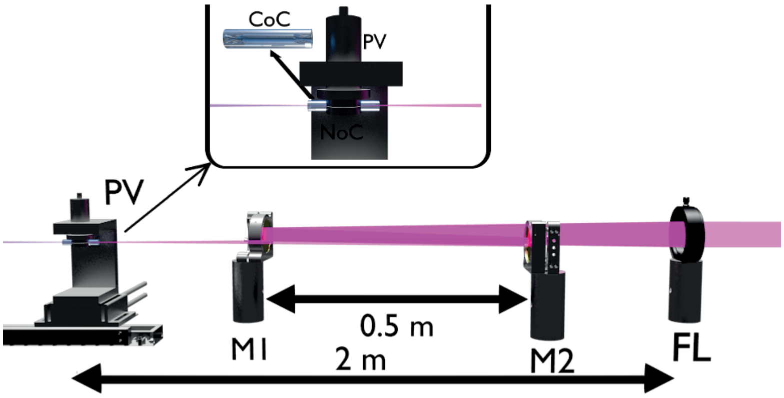

Figure 3.13: Scheme of the generation setup. The focusing lens (FL) is placed just before the entrance window of the vacuum chamber. Two flat gold mirrors (M1, M2) are added in order to increase the beam path inside the vacuum chamber minimizing the self-phase modulation (SPM) on the vacuum window.

The generation chamber is connected to the neighbouring one by a small cylinder with an aperture of 1 cm and length of 40 cm for differential pumping. This configuration helps to maintain the vacuum level in the chambers located downstream below 10^{-7} mbar. The next two vacuum chambers (fig. 3.14) contains the x-ray optics for control the HHG beam. When the harmonics are generated using a short focal length (using

NIR pulses) in the first chamber a flat SiO_2 mirror in combination with a toroidal mirror is used to steer and focus the beam in to the next chamber. A set of metallic filters can be placed either before the SiO_2 mirror or between this mirror and the toroidal one. This configuration is designed to produce a 1:1 image of the HHG source, located at 1.5 m from the toroidal mirror, in the center of the second chamber located as well a 1.5 m from the toroidal. The radius of curvature of the toroidal mirrors are chosen to produce this imaging with a grazing angle of 2 degrees.

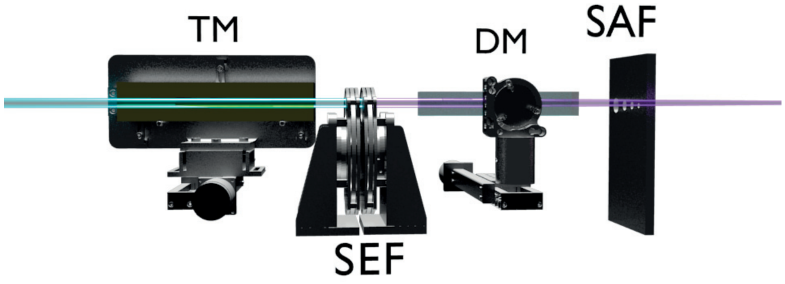

Figure 3.14: Configuration of the focusing optics for the loose focusing setup. TM is the toroidal mirror, SEF the metallic filter, SAP the pinhole arrays, and DM the SiO_2 mirror.

If high energy pulses (20 mJ) are used to produce the high-order harmonics another X-ray optics configuration is used. In this configuration the first vacuum chamber (at 1.5 m from the target) contains an array of pinholes to spatially filter out part of the remaining IR beam. In the second chamber (at 3 m from the target), a flat SiO_2 mirror is placed to steer the beam and a toroidal mirror performs the imaging of the source in the experimental chamber located 6 m away from the generation point. Between the SiO_2 mirror and the toroidal mirror two sets of metallic filters are placed to perform the spectral filtering of the HHG pulses. The toroidal mirror is designed to produce the 1:1 image of the HHG source under 2 degrees of grazing incidence.

In front of the experimental chamber, a rectangular chamber (500x1000 mm^2) is located in view of performing the online temporal characterization of the HHG pulses using the THz streak camera (chapter 4). This chamber can also be used to perform experiments that may benefits from its rectangular geometry. In this chamber we also placed an out coupling mirror in order to send the IR beam outside of the vacuum system to perform the correct alignment of the toroidal mirror. The beamline is equipped with two different X-ray spectrometers. The first one (fig. 3.15) is based on a transmission grating located around 300 mm before the CCD camera used to record the HHG spectra. In order to improve the spectral resolution, an adjustable slit is placed just before the diffraction grating. The second spectrometer is based on a cylindrical gold grating. This grating produce a line focus at CCD plane achieving a large spectral resolution. This spectrometer is designed for reflection angles between 70° and 85°. An entrance slit is placed at the entrance of the spectrometer in order to avoid reflection from the grating edges. In figure 3.16 we compare the recorded spectra using the two different spectrometers. We can see how the reflective grating one has a better spectral resolution than the transmissive one. However the global spectral response of both gratings seems to be identical.

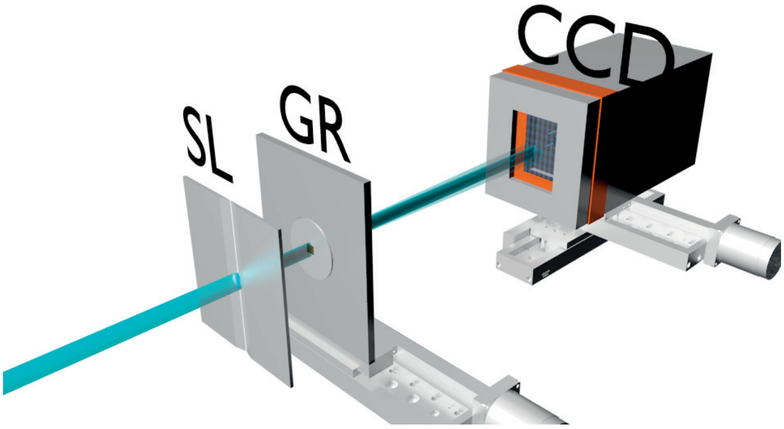

Figure 3.15: Basic scheme of the transmissive spectrometer placed in the experimental chamber. SL is the entrance slit and TG the transmission grating. The toroidal mirror located in chamber 5 has its focal spot on the CCD camera.

At the end of the beamline there is a 800 mm diameter chamber where pump-probe experiments take place. In this chamber the home-made spectrometer is located. The chamber is equipped with two in-vacuum CCD cameras, one of them allows to be fully inserted inside the chamber and the other one can be attached to one of the side flanges of the vacuum chamber.

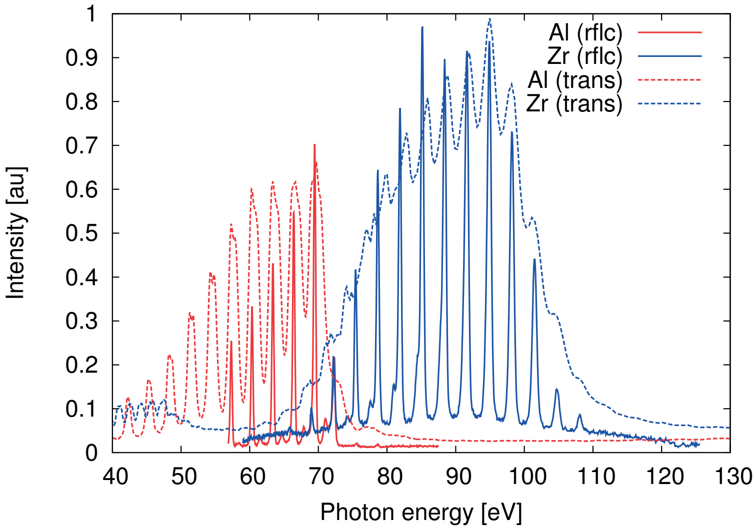

Figure 3.16: Comparison of the measured HHG spectra using the transmissive spectrometer, blue curve and the reflective one, red curve. The generation media was Neon with a back pressure of 3 bars.

3.2.3 Source characterization

In this section we present the spectral characterization of our high harmonic generation source. The HHG source is driven by one of the 20 mJ output of the Ti:sapphire laser system described in section 3.2.1.

The objective of this HHG source is to perform experiments on ultrashort X-ray pulse characterization and to study ultrafast magnetization dynamics. Figure 3.17 (left) shows a typical HHG spectrum using Argon as generation medium. Under this configuration we obtained a larger photon flux but with the harmonic photon energy limited up to 47 eV. This low energy cut-off is due to the low recombination probability produced by the Cooper minimum present in Argon [53]. Depending on the application we may use different generation conditions (i.e. focusing, gas, laser wavelength). So far, for the applications presented here we just changed the generation media in order to obtain either a larger photon flux (Argon) or higher photon energies (Neon). To perform the temporal characterization of the attosecond pulse train a THz streak camera was used. During this experiment the THz radiation was generated using 60 % of the energy leaving the remaining 8 mJ for HHG. This means that in principle even larger photon flux could be achieved by using the full 20 mJ delivered by the laser and increasing the focal length in order to obtain a large generation volume.

Figure 3.17 (right) shows the recorded HHG spectrum using Neon as generation medium it can be observed that the maximum photon energy is around 110 eV. This configuration is normally used to drive the experiment on magnetization dynamic. The laser energy used for HHG was 18 mJ leaving the remaining 2 mJ as pump for the magnetization experiment being enough to initiate the demagnetization process.

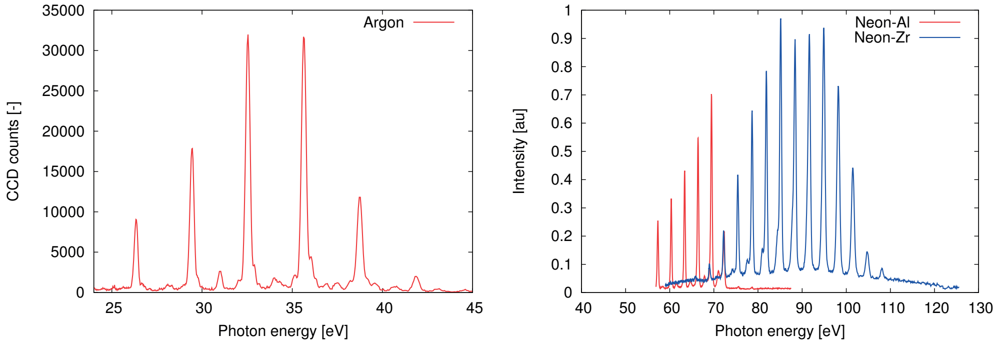

Figure 3.17: Left: high harmonic spectra using Argon as generation media. The HHG cut-off observed at 47 eV is due to the low generation efficiency around the Cooper minimum. Right: HHG spectra using Neon as generation media, back pressure 5 bar with a 210 μs opening time.

Using Helium as generation medium (fig. 3.18) the HHG cut-off is extended up to

130 eV. The blue curve displays the calculated transmission of the HHG beamline considering two Zirconium filters and one SiO_2 mirror under 2 degrees of grazing incidence angle. We can also observe a reflectivity drop for our SiO_2 mirror for photons energies above 100 eV.

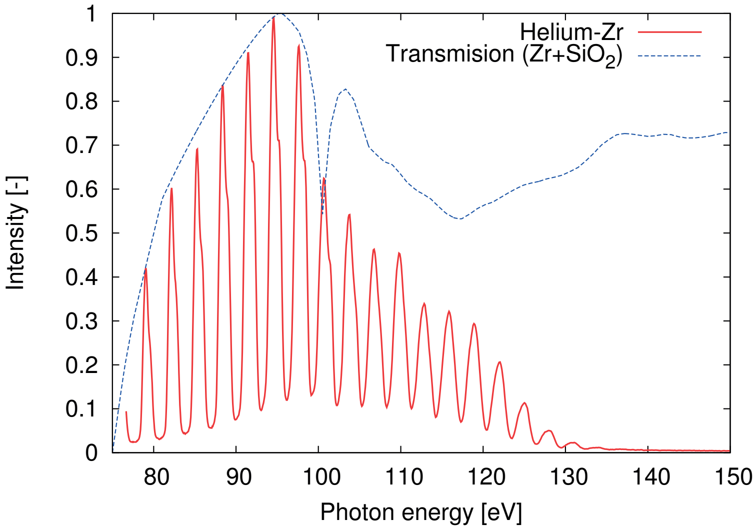

Figure 3.18: High harmonics spectrum using Helium as generation medium. Back pressure 3 bar with opening time of 220 μs.

To characterize the spectral stability of out HHG source we took two sets of measurement. The first one, for study the short-term stability and it consists in a sequence of 20 single shot spectra. In the second one, for study the long term stability we recorded a sequence of 200 spectra with 10 s integration time. The latter mimics the experimental conditions used for studying the ultrafast magnetization dynamics. For both measurement the generation medium was Neon with a backing pressure of 3 bar. As illustrated in fig. 3.19 the HHG spectrum is mainly impacted by intensity fluctuations. In order to quantify these fluctuations we computed the intensity stability for individual harmonics (order 41, 43, 45). The results are are summarized in table 3.1. We observed that for the single-shot measurement the spectral stability is around 5% rms, i.e. twice as large as the rms stability measured for the driver laser. The larger fluctuations in the HHG spectra are not surprising as the HHG process is a highly non-linear phenomenon.

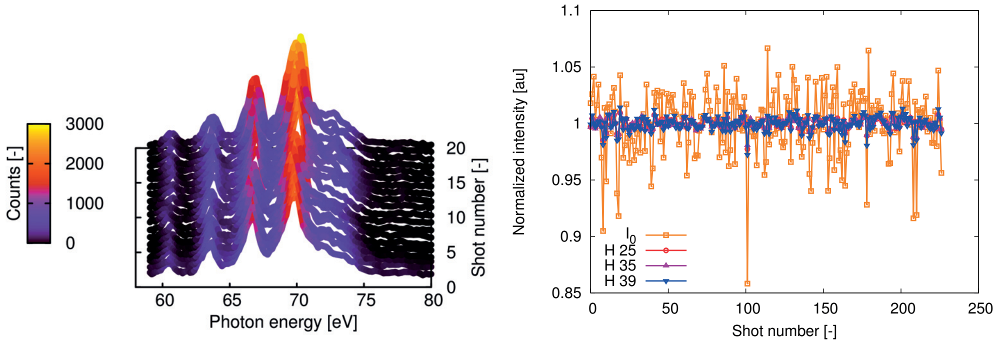

Figure 3.19: Left: Sequence of single shot HHG spectra for short term stability. Right: Normalize intensity for the different harmonic order in a sequence of more than 200 shots with integration time of 10 s.

	Short term		Long term	
Harmonic (-)	Rel. Inten. [-]	std (%)	Rel. Inten. [-]	std (%)
Zero	100	4.8	100	3
45	15	6.5	18	0.4
43	5	3.7	17	0.5
41	3	4.1	15	0.7
39	1	6.3	4	0.6

Table 3.1: Statistics for the integrated spectral intensities for the sequences of single shot measurements of fig. 3.19 for the harmonics 45 (69.75 eV), 43 (66.65 eV), 41 (63.55 eV) and for the entire spectral content (zero order of the grating).

Using these sets of measurements we have performed as well correlation studies for the different harmonics (table 3.2, table 3.3 and fig. 3.20). This study reveals that for the single shot measurement a correlation between 0.95 and 0.46 was found between the different harmonics and the non-diffracted beam intensity. The correlation becomes weaker for harmonic with a lower intensity. These harmonics have a better correlation with the noise of our CCD camera. However the stronger correlation is found between the individual harmonic and the average intensity of the remaining harmonics.

For the long term stability the best correlation is also between the intensity of a single harmonic and the average intensity of the remaining harmonics. The spectral stability after this 10 s integration is under 1% and the correlation coefficient above 0.95.

Corr. with	Harmonic [-] 45	43	41	39
I_0	0.95	0.65	0.67	0.46
Bg	0.44	0.60	0.53	0.72
Avg	0.86	0.81	0.83	0.82

Table 3.2: Correlation coefficients between the different harmonic orders and the non-diffracted beam (I_0), the measurement background (Bg) and the average between the other harmonics (Avg). The values were calculated using the short-term integration time measurement.

Corr. with	Harmonic [-] 45	43	41	39	25	23	21
I_0	0.66	0.75	0.82	0.80	0.78	0.79	0.86
Bg	0.69	0.57	0.51	0.53	0.61	0.58	0.49
Avg	0.95	0.98	0.98	0.97	0.98	0.97	0.97

Table 3.3: Correlation coefficients between the different harmonic orders and the non-diffracted beam (I_0), the measurement background (Bg) and the average between the other harmonics (avg). The values were calculated using the long-term integration time measurement.

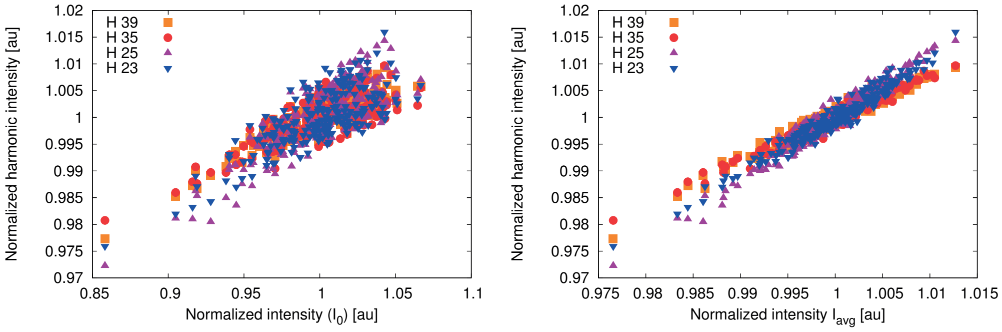

Figure 3.20: Intensity correlation for different harmonic orders as function of the non-diffracted intensity (left) and the average between the remaining harmonics (right).

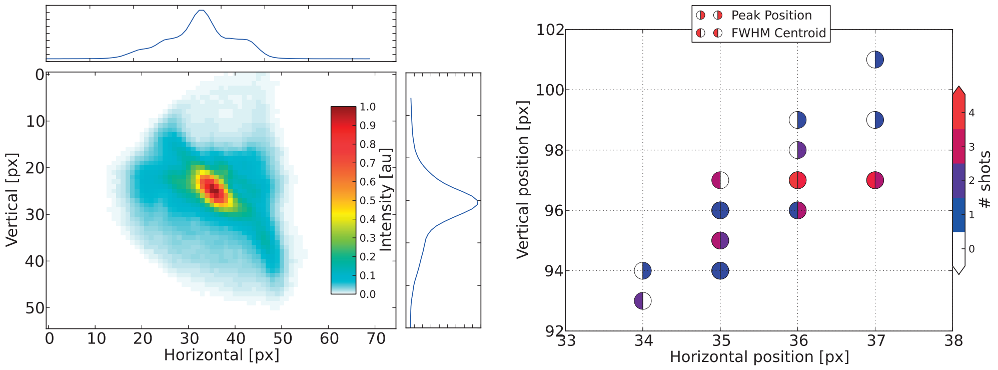

Figure 3.21: Left: HHG beam profile at the geometrical center of the experimental chamber. Right: beam pointing stability, right filled circles shows the peak position, left filled circles the position of the center of mass of the beam.

To complete the characterization of our high harmonic source we have performed an analysis of the HHG beam profile as well as the pointing and intensity stability. In fig. 3.21 (left) we can see the HHG beam profile at the center of the experimental chamber. Table 3.4 summarizes the spatial properties of the HHG beam. The HHG beam size is around 150 μm and slightly asymmetric. The beam position varies within 10 % (rms) of the beam size. The intensity fluctuations are around 5 % (rms). This is similar to the spectral stability (fig. 3.19, table 3.1) where the observed fluctuations were around 5% (rms). With these characteristics no major challenges are expected in HHG pump probe experiments.

Threshold	X [μm]	Y [μm]	Size x [μm]	Size y [μm]	Intensity [x 1e4 counts]
90	0 ± 19	0 ± 12	57 ± 9	55 ± 4	48 ± 6
50	16 ± 25	-5 ± 12	163 ± 25	138 ± 15	115 ± 5
1/e	17 ± 22	-6 ± 11	215 ± 21	171 ± 14	132 ± 7

Table 3.4: Pointing and energy stability of the HHG source. The generation conditions are identical to the one used for fig. 3.21. To estimate the beam size we take into account the pixels with intensities above the indicated threshold.

3.2.4 HHG source developments towards the water window

Extending the high harmonic cut-off towards higher photon energies is one of the main goal of the HHG community. Various applications especially in biology require photon energies in the spectral range between the K-edge of carbon (283 eV) and the Oxigen K-edge (532 eV), the so called water-window. Furthermore many materials show absorption edges in this spectral range making this development very interesting also for material science.

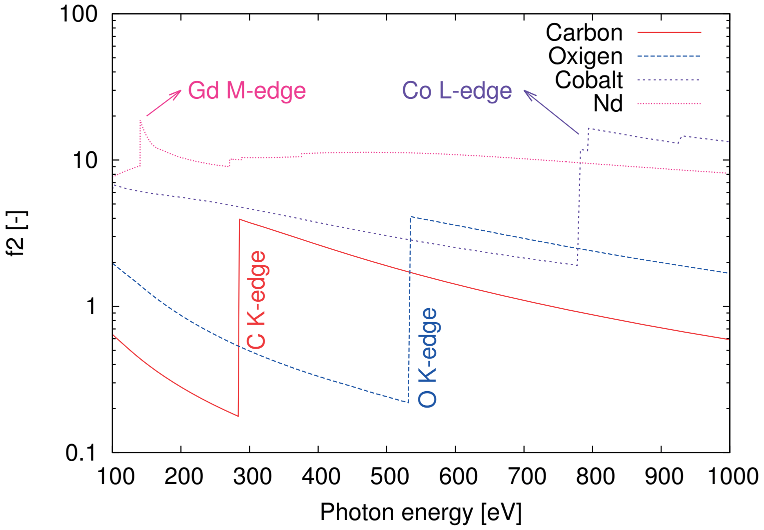

Figure 3.22: The absorption coefficient f_2 for different materials. The range between the O K-edge and C K-edge is known as the water window. The M-edge (L-edge) of Gadolinium (Cobalt) are relevant for magnetization experiments. The absorption coefficient is the imaginary part of the refractive index ($n = f_1 + i f_2$).

There are different routes towards extending the HHG cut-off energy. Equation (3.6) indicates that the HHG cut-off scales linearly with the laser intensity. In principle we can just extend the HHG cut-off by increasing the laser intensity. However to drive an efficient HHG process we need to take into account the phase matching conditions. As explained along the section 3.1.2 with intensities of the order of $2 \cdot 10^{15} \frac{W}{cm^2}$ the generation medium becomes fully ionized and it is not longer possible to achieve a efficient high harmonic generation in neutral atoms.

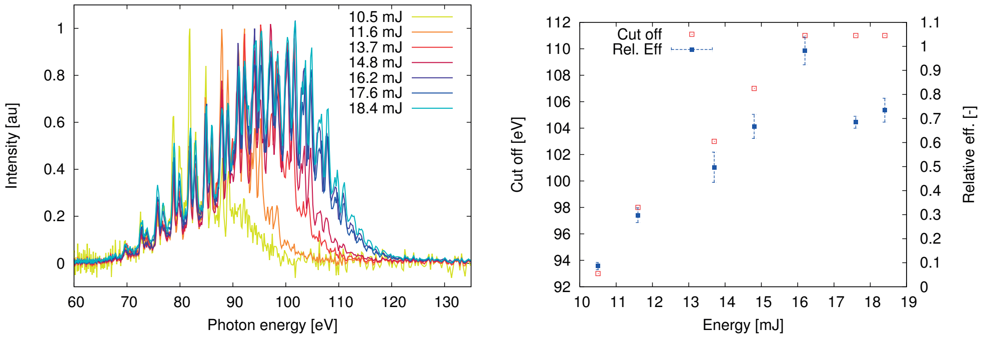

Figure 3.23: Left: evolution of the HHG spectra as function of the laser intensity. Right: maximum photon energy (red) and relative efficiency as function of the laser intensity (blue). The relative efficiency is calculated as the integrated energy along the spectrum divided by the driver energy.

Another approach one can use the scaling law describing the dependence of the cut-off energy with the squared wavelength of the driving pulse [23, 60]. Driving the HHG process with intense mid-IR laser it is possible to extended the HHG cut-off without fully ionize the gas medium. The cut-off extension as function of the driving laser wavelength originates from the fact that the ponderomotive energy of an electron quivering in the electric field of the laser increases with the wavelength of the laser field. This gain of energy is due to the fact that the electron spends a longer time in the accelerating field during the laser cycle. However, in the HHG process a longer travelling time prior to recombination with the parent ion entails that the electron wavepacket becomes more delocalized. This results in a dramatic decrease of the recombination probability of the electron with its parent ion. This reduction of the recombination probability results in a lower conversion efficiency for the single atomic response.

To study the wavelength scaling law experimentally we used the output of the Optical Parameter Amplifier described in section 3.2.1. For HHG the idler beam with a central wavelength tunable between 1.7 and 1.9 μm was used. The typical pulse energies were 3-4 mJ. In order to reach the intensities we used short focal optics (f = 1 m) for HHG. In a first attempt Argon was used as generation medium as it exhibits a higher photo-ionization cross section compared to He or Ne. This increases the recombination probability of the electron with its parent ion.

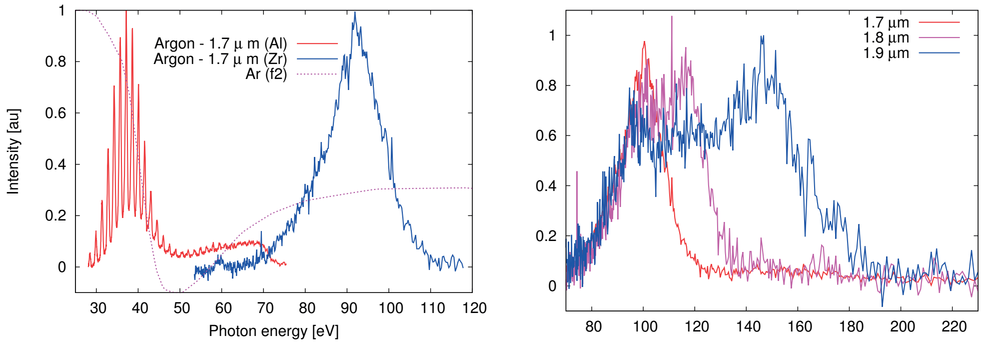

Figure 3.24: Left: HHG spectra obtained using a 1.7 μm-50 fs driving laser, the pink curve represent the f_2 form factor that takes into account the photo-ionization cross section. Right: evolution of the HHG spectra in Argon as function of the drive wavelength.

In fig. 3.24 the HHG cut-off is measured for three different wavelengths. The experiment shows how the maximum photon energy increases from 110 eV to 180 eV by scaling the driving laser wavelength from 1.7 up to 1.9 μm. In order to extend even further the HHG cut-off Neon was used as generation medium. In fig. 3.25, we can observe how using a 1.7 μm driving laser emission beyond the 200 eV edge of Zirconium is achieved with a maximum photon energy at 300 eV, just the beginning of the water window. Unfortunately technical problems on the 40 mJ beamline prevents us to continue this research.

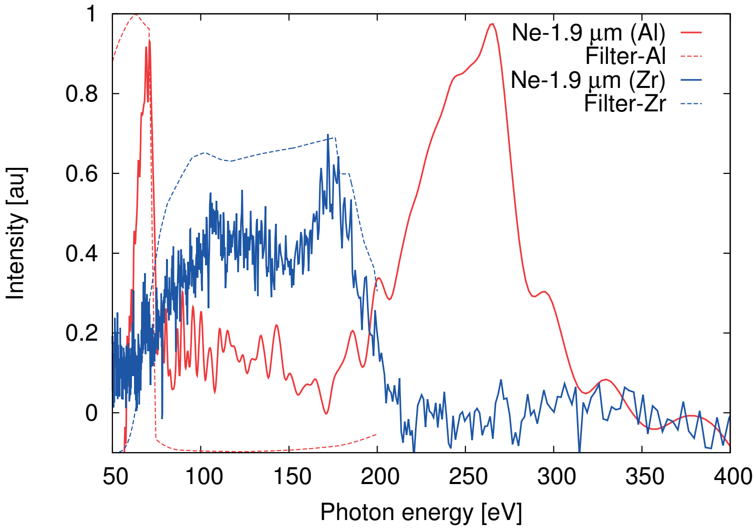

Figure 3.25: High harmonic spectrum using a 1.7 μm driving laser and Neon as generation medium. In blue (red) the obtained spectrum using a Zirconium (Aluminum) filter.

3.2.5 Conclusion

The spectral and spatial characterization of our HHG beamlines show the capabilities of this source to perform experiments where a high amount of photons is required like magnetization dynamics, non-linear studies or single-shot experiments.

Driving the high-order harmonic generation with our Ti:sapphire laser source, we can perform studies using the M-edge of different materials. Many applications can benefit from the large number of photons per pulse produced by our source, for example in magnetization studies high fluxes are required to obtain a good S/N but due to the slow relaxation time of the process, a minimum separation time of ms is required between pulses.

On the other hand, the first studies on HHG using a NIR driving laser shows the promising capabilities for this source to perform experiments within the water-window. Even if in our first measurements the source doesn't provide yet a full cover of the water window with an appropriate number photons, we have to remind this was a few days work. For example combining the wavelength scaling with the phase matching condition in capillaries, one can entail an increase of the photon flux and a full cover of the water window.

Finally to have a full characterization of our high-order harmonic source the temporal characterization is still missing. In the next chapter, we perform such characterization in combination with the commissioning of a THz streak camera that is foreseen to be used as a time of arrival diagnostic for SwissFEL.

4 Temporal characterization of ultra-short X-rays pulses

Contents

Nowadays ultrafast lasers have become a fundamental tool for many researchers. They provide ultrashort pulses that allow to study ultrafast phenomena with unprecedented temporal resolution. However, we also need to be able to perform the characterization of such pulses. Using modern electronic like fast photodiodes it is possible to achieve temporal resolution in the picosecond time scale. To characterize shorter pulses we have to use a different kind of techniques. Some techniques are based on the optical sampling of the pulses using even shorter pulses (cross-correlation) or the same pulse (auto-correlation) [13], with these techniques we can obtain the intensity profile of our pulses with some limitations. Further information, such as the phase or the actual electric field of the pulse, is not accessible through this techniques. This requires other techniques which are based on the characterization in the spectral domain. Performing the characterization in the spectral domain is an advantage since the spectral amplitude of the light pulse are easily measured with even subnm precision. However to successfully obtain the temporal characteristics of the pulses using the Fourier transform we need to know both the spectral intensities and phases. In the spectral region between THz and UV radiation, the non-linear interaction of different light pulses in a non-linear media allows us to retrieve this information. Typical examples of techniques using this approach are the Frequency Resolved Optical Gating (FROG) [61], Spectral Phase Interferometry for Direct Field Reconstruction (SPIDER)[62] or Self Referenced Spectral Interferometry (SRSI) [63].

The characterization of ultrashort light pulses in the region between VUV and soft X-rays adds another degree of difficulty. On this spectral range, most of the materials have a large absorption coefficient. This makes no longer possible to use the above mentioned techniques because the absorption in the material prevents the non-linear interaction of the pulses.

To overcome this limitation we can use an indirect approach based on the characterization of an electron beam generated by the light pulse to be characterized. The principle of this approach is that the photoemission process transfers the temporal and spectral characteristics of the incident radiation to the generated electron beam. In this way by characterizing the electron beam is possible to obtain an indirect measurement of the temporal properties of the X-ray pulses. There are several techniques using this approach for the temporal characterization. The following sections will present some of these methods starting with a version of the Frequency Resolve Optical Gating adapted to X-rays (FROG-CRAB)[64]. We start with this technique because it makes use of a more general description of the physics governing these phenomena.

The last section presents a description of the temporal characterization using the streaking technique [65, 27]. This technique does not provide the full spectral phase information but is capable of obtain some properties of the pulse just by comparing the streaked and unstreaked electron spectrum.

The method used to perform the temporal characterization strongly depends on the characteristics of the X-ray source. For example, HHG sources are intrinsically synchronized with other laser and provide a good shot to shot stability however, these sources do not provide pulses with a large number of photons. With these characteristics, HHG sources, especially the ones with a high number of pulses per second, are more suitable for characterization using scanning techniques. Other light sources like FELs are capable of providing extremely intense pulses but suffer for strong shot to shot fluctuations and lack of synchronization with external lasers, these sources are more suitable for a single shot characterization.

4.1 Frequency resolve optical gating

Frequency Resolve Optical Gating is a technique developed in 1991 by R.Trebino and D.J Kane [61], it allows to perform the temporal characterization of ultra-short laser pulses. It is based on the temporal decomposition of the pulse to be characterized by an optical gate. The spectra of different temporal slices are recorded and result in the so called FROG-trace or spectrogram. This spectrogram consist in a 2D-array collection of spectra acquired for different time delays between the pulse and the gate. The spectral phases are retrieved using a phase retrieval algorithm based on the decomposition of the spectrogram in eigenvectors using different technique such as Generalized Principal Component Analysis (GPCA) [66].

The reconstruction algorithm (see Fig. 4.1) works as follows: First, it sets an initial guess for the pulse $I(t)$ and the gate $G(t)$ (blind FROG) based on the recorded spectrogram $F_e(E,\tau)$. Using this initial guess a time domain spectrogram is calculated as the cross product of pulse and gate $S(t,t') = E(t) \times G(t')$.

Afterwards a temporal ordering is performed $S(t,\tau) = \tilde{T}[S(t,t')]$ (4.1) where the columns f the matrix are ordered by increasing values of the time delay ($\tau = t - t'$). Finally we bring the spectrogram from the time domain to the the frequency domain using Fourier transform along the time axes of the pulse. In this way the calculated spectrogram $F_c(E,\tau) = \mathcal{F}[S(t,\tau)]$ is constructed.

$$S(t,t') = \begin{vmatrix} S_{11} & S_{12} & \cdots & S_{1n} \\ S_{21} & S_{22} & \cdots & S_{2n} \\ \vdots & \vdots & \ddots & \vdots \\ S_{n1} & S_{n2} & \cdots & S_{nn} \end{vmatrix} \qquad T[S] = \begin{vmatrix} S_{1,\frac{n}{2}-1} & \cdots & S_{1,1} & \cdots & S_{1,\frac{n}{2}} \\ S_{2,\frac{n}{2}+1} & \cdots & S_{2,2} & \cdots & S_{2,\frac{n}{2}-1} \\ \underbrace{\vdots}_{\tau=-\frac{n}{2}+1} & & \underbrace{\vdots}_{\tau=0} & & \underbrace{\vdots}_{\tau=\frac{n}{2}-1} \end{vmatrix} \tag{4.1}$$

Now we replace the spectral amplitudes of F_c by the retrieved ones preserving the phases $F_r = \sqrt{|F_e|^2} exp\{\imath arg(F_c)\}$. F_r is transformed back to the time domain by inverting the previous operation $S_r = \tilde{T}^{-1}[\mathcal{F}^{-1}(F_r)]$ and S_r is finally decomposed in two eigenvectors (gate and pulse) using a Singular Valued Decomposition (S.V.D) algorithm. The retrieved gate and pulse are used as seed for the next iteration.

To perform the temporal gating different techniques can be used. For example, in the visible part of the spectrum a non-linear processes is typically used as temporal gate. Each process sets a different gate, for example in the case of Second Harmonic Generation (SHG FROG) the gate is given by $G(t') = E(t')$ and using the Kerr effect (PG FROG) the gate is $G(t') = |E(t')|'$.

For the wavelength range below 100 nm these non-linear processes can not be used due to two main reason: First, the strong absorption coefficient that any material has in this spectral region prevents transmission for reasonable thick crystals. Second the non-linear interaction requires high intensities to generate significant output, something which is difficult to achieve with HHG sources.

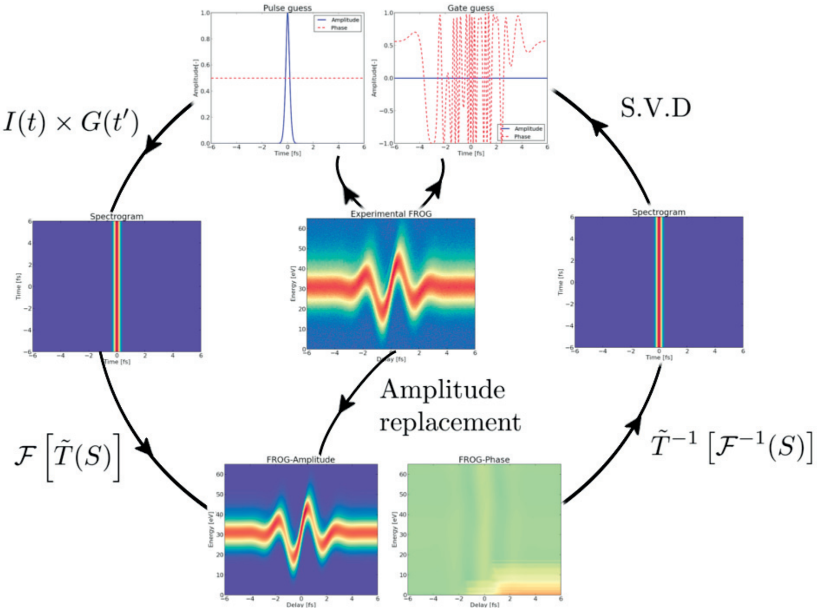

Figure 4.1: Scheme of the reconstruction algorithm of a Frequency Optically Resolve Optical Gating (FROG) trace.

To overcome this limitation we can apply the same principles that are used in the conventional X-ray streak camera. In those devices the X-rays generate an electron beam by illuminating a metallic or semiconductor photocathode. The temporal profile of the generated electron beam provides a one to one replica of the incident X-ray pulses. The temporal structure of the electron beam is mapped into a spatial dimension by applying a time-dependent electric field, so called streak field, to the generated electron beam. The resolution of the streak camera is limited by the gradient of the applied electric field as well as the blurring of the temporal profile produced due to the space charges forces inside the electron beam. The temporal mapping to the generated electron beam is not preserved for sub-picoseconds pulses when semiconductor cathodes are used as we discussed in section 2.1.1.

For these reasons several adjustments have to be performed in order to make this technique suitable for ultrashort (femto- to attosecond) X-ray pulses. The photocathode is replaced by a gas jet in order to warranty the temporal mapping of the temporal profile. The time-dependent electric field is replaced by the electric field of a laser pulse (so called dressing pulse) allowing to achieve higher field gradients. Thanks to the combination of both (gas media and laser field) it is possible to streak the generated photoelectrons right after they are generated, which minimizes the effect of space charge [some reference].

These are the modification made on the experimental configuration to be able to obtain a meaningful FROG spectrogram for short X-ray pulses. To use the FROG algorithm we also need to calculate the corresponding spectrogram using an initial input pulse and gate in the time domain. We can profit from the fact that high-order harmonic generation also implies photo-ionization and the later acceleration of electron in the electric field of a laser pulse. Therefore we can make use of equation (3.11) as starting point for the calculations. Following [64] the spectrogram of this photoelectrons is given by:

$$S(W,\tau) = \left\| -i\int_{-\infty}^{\infty} dt\, e^{i\phi(t)} \mathbf{d}_{\mathbf{p}(t)} \mathbf{E_H}(t-\tau) \exp\left[i(W+I_p)\,t\right] \right\|^2 \tag{4.2}$$

Where $d_{p(t)}$ is dipole transition element, $E_H(t)$ the X-ray pulse to be characterized, τ the time delay between XUV and streaking pulses, W the energy of the generated photoelectrons, and $\phi(t)$ is the phase factor of the electronic wavefunction:

$$\phi(t) = -\int_{t}^{\infty} dt' (\mathbf{v}\cdot\mathbf{A}(\mathbf{t}') + \frac{\mathbf{A}^2(t')}{2}) \tag{4.3}$$

In general the effects produced by the envelope of the dressing field on the electron spectrum can be neglected and the slowly varying envelope approximation can be applied. The vector potential can be approximated under this condition to: $\mathbf{A}(t) = \frac{\mathbf{E(t_0)}}{\omega_s}\sin(\omega_s\, t)$ and the phase terms is then:

$$\phi(t) = -\int_{t}^{\infty} dt U_p(t) + \sqrt{\frac{8\,W\,U_p(t_0)}{\omega_L^2}}\cos\theta\cos\omega_L t - \frac{U_p(t_0)}{2\omega_L}\sin 2\omega_L t \tag{4.4}$$

We can observe the dependence of the phase term with $W^{\frac{1}{2}}$, this dependence sets a limitation for this technique that rise up from the fact that we have to be able to revert the spectrogram from the spectral domain to the time domain. This can be done only if we neglected the energy dependence of the gate and we use just a central energy W_0. However this approximation reduces the reliability of the technique when extremely broadband pulses are used. As we mentioned before, there are different kinds of the FROG algorithm depending on the used gating process. In our case our it is a purely phase gate since no modulations on the intensity are produced in the spectrogram. This kind of FROG algorithm is known as FROG-CRAB. For simplicity we will simply refer to it as FROG.

In general the physics behind Eq. (4.2) is used in many other techniques like streak cameras, RABBIT [67], PROOF [68], etc. The advantage of FROG respect to other methods like RABBIT or streaking is that provides a complete reconstruction in most of the cases without any restriction on the relationship between dressing field and the X-ray pulse.

4.1.1 Numerical simulations

Based on the above mentioned algorithm, a code for FROG retrieval has been developed. To test this retrieval we have calculated spectrograms of two different input pulses. We feed the intensities of this spectrogram as experimental traces to the FROG code I developed. The goal of this numerical simulation is to verify the performance of the algorithm and to know which are its main limitations.The first numerical simulations consist in a XUV pulse with a pulse duration lager than the optical cycle of the dressing field. In this way we mimic the typical conditions where the RABBIT analysis is performed. More precisely the X-ray pulse consist on an attosecond pulse train (APT) produced by the coherent combination of odd harmonics of a 800 nm laser centered around a central frequency ω_0 and spaced by 3.1 eV. These pulses are expressed in the frequency domain as:

$$E(\omega) = exp\left\{ \frac{-(\omega-\omega_0)^2}{2\sigma_{env}^2} + i\left(\xi_2 \frac{(\omega-\omega_0)^2}{2\sigma_{env}^2} + \xi_3 \frac{(\omega-\omega_0)^3}{6\sigma_{env}^3}\right)\right\} \sum_{-n}^{n} E_n(\omega_n) \tag{4.5}$$

Where each $E_n(\omega_n)$ is similar to the Gaussian envelope of (4.5) but now center around the individual harmonics ω_n. With this definitions we have the r.m.s bandwidth of the total envelope σ_{env} and the harmonic bandwidth σ_n as well as the second and third order chirp for the pulse envelope (ξ_2 and ξ_3) as well as for the individual harmonics (ξ_{2n} and ξ_{3n}).

The APT is made out of 7 harmonics (n=3) centered around 20 eV with an energy spacing of 3.1 eV. For the total envelope the rms bandwidth is set to $\sigma_{env} = 9.3\,eV$ and the harmonics bandwidth $\sigma_n = 0.2\,eV$. The dispersion coefficient are of the individual harmonic is given by: $\xi_2 = 8.0$, $\xi_3 = 0$, $\xi_{2n} = 0$, $\xi_{3n} = 3 \cdot 10^{-1}$.

The dressing field is a four cycles IR laser $\sim$ 10.6 fs (r.m.s) with a central wavelength of

800 nm. The pulse intensity is set to $I = 1.3 \cdot 10^{17} \frac{W}{m^2}$.

After 300 iterations an accurate reconstruction of the amplitude and phase of the X-ray pulse is obtained (fig. 4.2). This is the main advantages respect to a RABBIT reconstruction where only the first order chirp and a symmetric pulse envelope is obtained. However along this simulation the effects of the space charge forces are neglected. This is something that should be taken into account for simulating high intensity X-rays pulses. It must be assumed that the space charges forces produce a broadening of the spectral lines. This spectral broadening leads to an underestimation of the pulse duration.

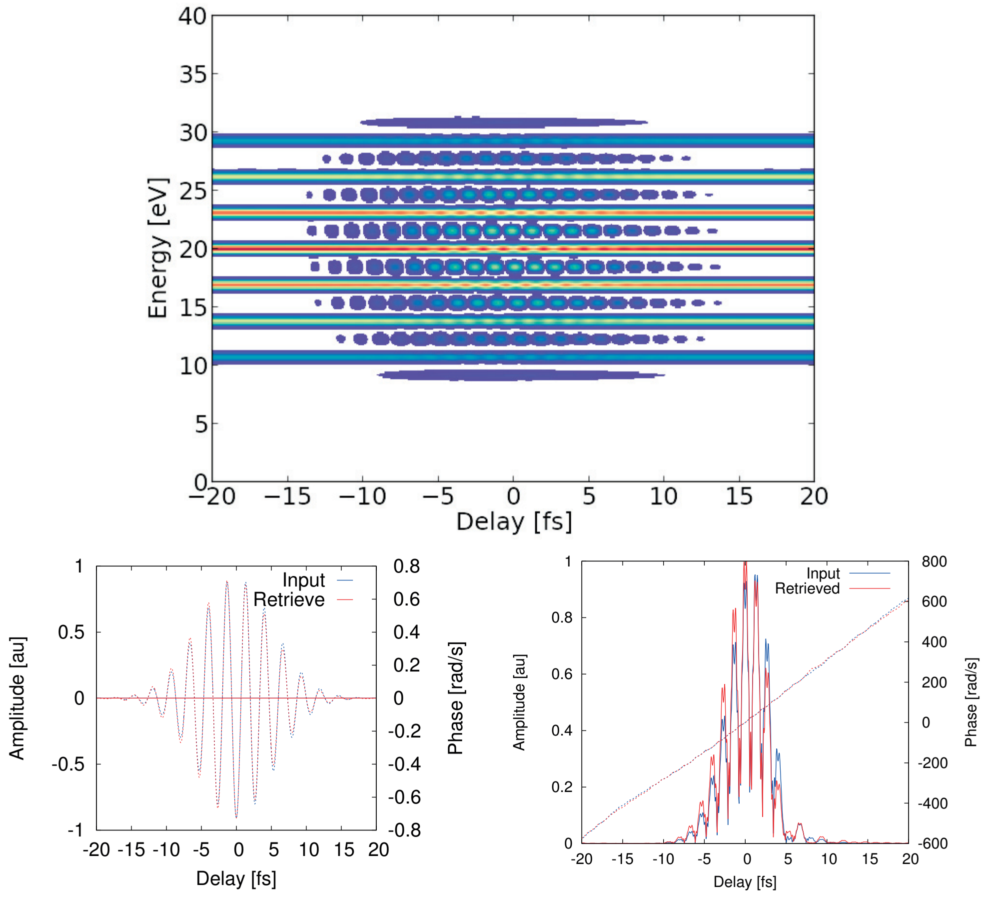

Figure 4.2: FROG retrieval from an APT with 7 harmonics with a central energy of 20 eV spaced by 3.1 eV . The dressing electric field has peak field of $10^9 \frac{V}{m}$ with four cycles and a period of 2.66 fs.

The result for the first simulation shows how in addition to the pulse duration and attochirp as in the case of a RABBIT measurement the full temporal profile of the X-ray pulse is retrieved.

In the second simulation the XUV pulse duration is shorter than the dressing field mimicking in this case the situation for the streak camera (fig. 4.3). For this simulations we use an isolated attosecond pulse (IAP) with a pulse duration of 200 as (rms) and central photon energy of 30 eV. This pulse is streaked by a single cycle 800 nm pulse with an intensity of $3.3 \cdot 10^{16} \frac{W}{m^2}$.

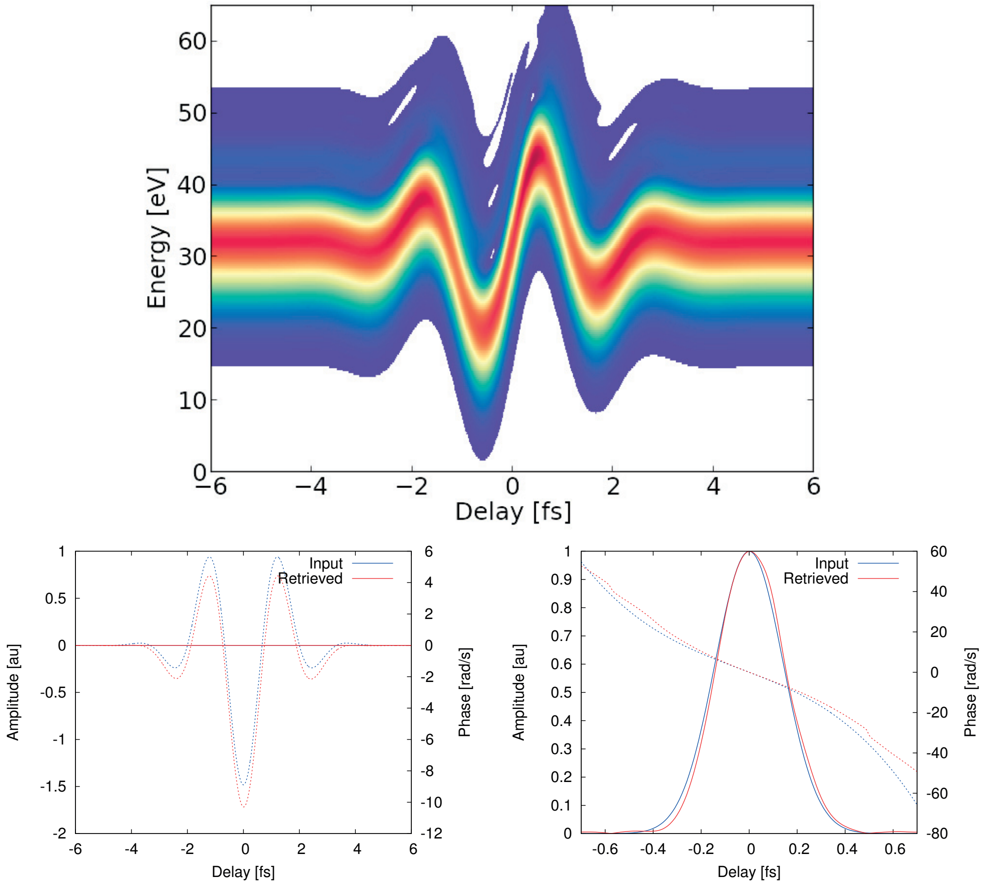

Figure 4.3: FROG retrieval from an ATP consisting in six pulses each one with a pulse duration of 200 as. Central photon energy is 30 eV. Dressing field is a 1e12 V/cm single cycle 800 nm pulse.

In order to check the effects of the approximation made in Eq.4.4 we performed some numerical simulations comparing the rms error of the retrieved pulse as function of the spectral bandwidth. This simulations used Gaussian pulses with up to third order

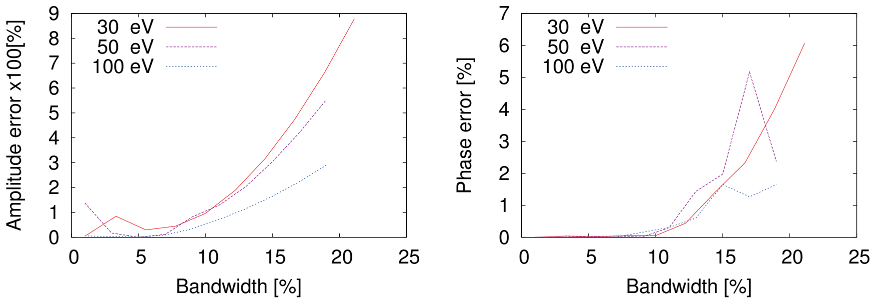

Figure 4.4: Left (right), rms amplitude (phase) error in the retrieved pulse after 150 iterations.

dispersion expressed by the equation:

$$E(\omega) = exp\left\{-\frac{(\omega-\omega_0)^2}{4\sigma_w^2}\right\}\, exp\left\{-i\left(\frac{\xi_2}{2\sigma_w^2}(\omega-\omega_0)^2 + \frac{\xi_3}{6\sigma_w^3}(\omega-\omega_0)^3\right)\right\} \tag{4.6}$$

Fig.4.4 summarizes the results of the numerical simulations performed for different central photon energies (30, 50 and 100 eV). The simulations were carried with $\xi_2 = 0.2$ and $\xi_3 = 0.1$. The temporal scale and the streaking frequency were also scaled according to the different photon energies. Due to the scaling of the streaking frequency the peak field is also scaled in order to keep the same phase modulation for the gate.

The simulations show how for bandwidth above the 20% of the central photon energy the error in the retrieved pulse duration is still below the 1%. Nevertheless it is necessary to take into account that the simulations neglected the effect of space charge forces that are dominant for shorter pulse duration.

4.1.2 FROG-CRAB conclusions

Keeping in mind that the main goal is to provide a suitable technique to perform the temporal characterization of HHG pulses but also in the future for the X-rays pulses delivered by a Free electron laser this technique has three major drawbacks.

First the requirement of a temporal synchronization between the FEL pulses and external laser below the pulse duration of the FEL what is typically around 100 to 10 fs. This nowadays is not possible to achieve for SASE FELs.

Second, in order to perform the FROG retrieval we need to acquire accurately several spectra at well defined time delays between the FEL pulse and dressing field. In SASE FELs this becomes unpractical. Due to the statistical nature of the process, the generated x-ray pulses show a large shot to shot variation in shape, amplitude, and central energy. Thus in the best case, an averaged FEL pulse can be reconstructed, but which is strongly deviating from the individual shots. Further the arrival time time jitter is in general larger then the FEL-pulse duration. Without the help of a external timing tool this limits the time resolution of the measurement to the timing jitter, thus renders the technique useless.

And finally it neglects the space charges forces on the electron beam, which must be expected when generated from high intensity X-rays pulses. This produces significant spectral broadening of leads to strong under estimation of the pulse duration.

To overcome these limitations in the next chapter the THz streak camera is presented. With this technique a full characterization of the temporal structure of X-rays pulses is not longer possible but it is possible to obtain some temporal properties of the x-ray pulse in a single shot basis and compensate as well the space charge effects. Furthermore using THz pulse as dressing field it is possible to profit for its long, above 100 fs, linear part of the electric field in order to measure the arrival time of the x-ray pulses respect to the external laser. This information is very useful in FEL's order to perform time resolved experiment with an unprecedented resolution.

4.2 Streak camera

The previously discussed retrieval algorithm provides a full temporal characterization of X-rays pulses. To perform this retrieval we have to measure the spectrogram of the X-ray source on the presence of dressing electric field. This implies to record multiply photoelectron spectra at many different time delays. To perform this measurement is essential to have a time jitter between the dressing and X-ray pulses smaller than the pulse duration. Another important point is that the electrons maybe still affected for some artificial spectral broadening due to the space charge forces in particular with high intensity X-ray sources. These requirements make the FROG reconstruction not suitable for the characterization of light sources with high pulse intensities or weak synchronization between the the dressing field and X-rays. Furthermore if the goal is to perform the temporal characterization of an X-ray source like SASE FELs we can only take into account techniques that are based on a single shot acquisition since the temporal and spectral profile of FEL pulse varies shot to shot.

Starting from the same physical principles as FROG-CRAB is based on, it is possible to apply several approximations to the eq. (4.4) in order to perform an analytical analysis of the electron spectrum generated by the X-ray pulse under the effect of a dressing field. In this ways we make it possible to extract pulse duration as well as the first order chirp of the X-ray pulses in a single shot basics.

The first approximation is made on the gating function, where a weak streaking field ($U_p \ll W$) is assumed. Under this conditions the second term in equation eq. (4.4) becomes dominant and the other terms can be neglected. The leading term can be also approximated, using the small angle Taylor expansion for the cosine function. Finally the gate gets reduced to:

$$\phi(t) \approx \sqrt{\frac{8\,W\,U_p(t_0)}{\omega_L^2}}\cos\theta\left(1-\frac{\omega_L^2 t^2}{2}\right) = \frac{s}{\omega_d^2}\left(1-\frac{\omega_d^2 t^2}{2}\right) \tag{4.7}$$

Another approximation is the assumption of a Gaussian like temporal profile for the X-ray pulse including a first order chirp. These pulses are represented by the equation :

$$E_H(t) = \exp\left\{-\frac{(t-t_0)^2}{4\,\tau^2}\right\}\exp\left\{-i\left[\omega(t-t_0)+\xi(t-t_0)^2\right]\right\} \tag{4.8}$$

with τ the rms pulse duration and ξ the first order chirp. The length of a transform limited pulse with the same spectral width is given by:

$$\tilde{\tau}^2 = \frac{\tau}{1+16\tau^4\xi^2} = \frac{1}{4}\sigma_0^{-2} \tag{4.9}$$

Now with these approximations it is possible to combine all the exponential terms in Eq.4.2 obtaining a second order polynomial:

$$\overbrace{-\left[\frac{1}{4\tau^2}+i\left(\frac{s}{2}+\xi\right)\right]}^{a^2}(t-t_0)^2+\overbrace{i\,[\,W-\underbrace{(W_0+st_0)}_{W_0'}\,]}^{2ab}(t-t_0)+i\left(\frac{s}{\omega_d^2}+st_0^2\right)= \qquad (4.10)$$

$$=(t'+b)^2-b^2+ic$$

where:

$$b^2=\frac{-(W-W_0')^2}{\frac{1}{\tau^2}+i(2s+4\xi)} \qquad (4.11)$$

with this polynomial Eq.4.2 just becomes a Gaussian integral expressed like:

$$S(W)=\left\|-i\,d_p(t_0)\,exp\left\{-\frac{(W-W_0')^2}{\frac{1}{\tau}+i(2s+4\xi)}\right\}\int_{-\infty}^{\infty}dt\,e^{(at'+b)^2}\right\|^2$$

and after integration can be easily obtained that:

$$S(W)=\frac{\sqrt{|d_pE_H(t_0)|^2}}{\sqrt{\mu}}exp\left\{\frac{-(W-W_0')^2}{2(\sigma_0^2+\tau^2\left[s^2\pm4\left|s\right|\xi\right])}\right\} \qquad (4.12)$$

Where σ_0 is the unstreaked bandwidth of the photoelectrons and $\mu=\sqrt{(1+s\xi\tau^2)^2+s^2\tau_4}$.

It is important to notice how W_0' takes into account the energy shift produced by the dressing electric field. However the expression $W_0'=W_0+st_0$ is just a consequence of the Taylor expansion made on eq. (4.7) the full expression is given by:

$$W_0(t)=W_0+\sqrt{2W}A(t) \qquad (4.13)$$

As shown in Eq.4.12 the broadening produced under the effect of the streaking field depends on the pulse duration as well as the chirp. By combining the measurement at two different positions of the streaking slope we can calculate directly both the pulse duration and the chirp using the following expressions:

$$\tau=\frac{\sqrt{\sigma_+^2+\sigma_-^2}}{2s} \qquad \xi=\frac{\sigma_+^2-\sigma_-^2}{8s\tau^2} \qquad (4.14)$$

To obtain a first approximation to the theoretical limit for the temporal resolution we can impose that the streaking field produces a significant broadening the spectral distribution respect to the unstreaked electron, this condition can be expressed as:

$$\beta = \frac{s\tau}{\sigma_0} \gg 1 \tag{4.15}$$

The temporal resolution of the measurement scales with the ponderomotive potential $U_p = E^2/4\omega_0^2$. The straight forward way to control the resolution is by changing intensity of the streaking field. However the approximations made in (4.7) limits the maximum streaking field for which an analytical solution exists in such way that reconstruction algorithms such FROG-CRAB are not needed. An alternative approach would include modifying its frequency, generally not readily available. In our experiment we estimate a ponderomotive energy of the THz field of $U_p \approx 1.2\,\text{eV}$, where as the measured kinetic energies of the photoelectrons are between 8 and 20 eV, thus not the maximum resolving power can be achieved.

4.2.1 Numerical simulations

The previous section has presented the principles of FROG-CRAB temporal characterization for X-rays pulse. The first step of that algorithm was to calculated the spectrogram of the X-ray pulse with the dressing field. Now it is possible to use the same calculations to simulate a spectrogram produced by a given X-ray pulse and gate function. Later on we will perform the streaking analysis of this spectrogram in order to cross check that the correct temporal properties of the pulse are obtained.

Ideally we should simulate the same conditions as founded in the experimental measurements however to produce spectrogram in the spectral domain with electron energies up to 20 eV requires high temporal resolution. This temporal resolution becomes a limiting factor for simulating a THz streak camera since the temporal resolution has to be maintained along the whole length of the THz pulse. Fulfilling these conditions we will produce an array with millions of data points imposing extremely high demands on computing performances.

For this reason the simulations are performed under different conditions from the experimental ones. However these simulations will still provide information about the validity of this technique and help to clear up any error in the analysis of the streaking experiment.

The first set of simulations are performed using a isolated x-ray pulse that generates and electron beam with central energy of 10 eV. The dressing field was set to a single cycle 15 μm pulse with an intensity of $2 \cdot 10^{10} \frac{W}{cm^2}$. The parameters of the simulation are summarized in table 4.1.

Figure 4.5 represents the retrieved pulse duration and first order chirp as function of the CEO phase of the streaking field. The different lines represent different first order chirp and pulse duration. It can be observed how for longer pulse duration the region where the retrieved values are corrected is becoming smaller. The retrieval error is symmetric respect to the zero phase point for both the chirp and the pulse duration. This behavior is in agreement with the approximation made along the previous section.

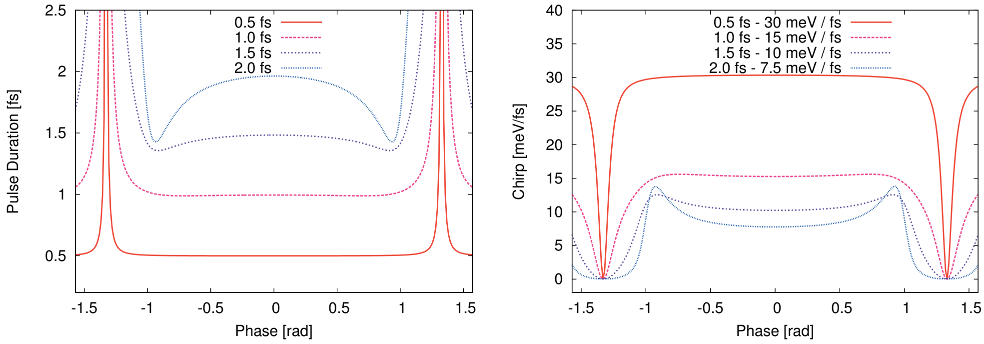

Figure 4.5: Left (right), pulse duration (chirp) as function of the CEO phase of the streaking field. Labels indicate the retrieved pulse duration and phase order phase at zero CEO phase.

Pulse duration (input) [fs]	ξ_i [meV/fs]	Pulse duration (retrieve) [fs]	ξ_r [meV/fs]
0.5	30.4	0.5	30.3
1.0	15.2	1.0	15.3
1.5	10.1	1.5	10.2
2.0	7.6	2.0	7.8

Table 4.1: Summary table for the simulation of fig. 4.5 with the parameter of the input pulse and the retrieved pulse parameter.

Other weakness of the streaking technique is the limitation to retrieve Gaussian pulses with only a first order chirp. In the next simulation we assume a Gaussian pulse but including a second order chirp, these pulses are represented by the following equation:

$$E_H(t) = \exp\left\{-\frac{(t-t_0)^2}{4\,\tau^2}\right\} \exp\left\{-i\left[\omega(t-t_0)+\xi_2(t-t_0)^2+\xi_3(t-t_0)^3\right]\right\} \quad (4.16)$$

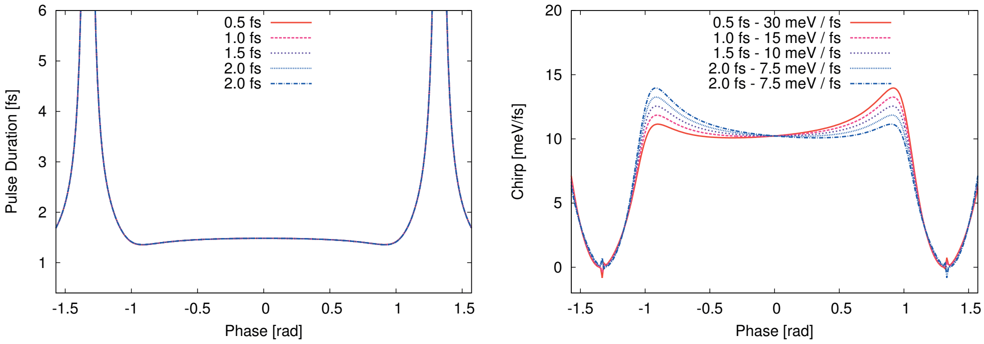

Figure 4.6: Left (right), pulse duration (chirp) as function of the CEO phase of the streaking field. Labels indicates the retrieved pulse duration and phase order phase at zero CEO phase.

Pulse duration (input) [fs]	ξ_{2_i} [meV/fs]	ξ_{3_i} [MeV fs^{-2}]	Pulse duration (retrieve) [fs]	ξ_{2_r} [meV/fs]
1.5	10.13	-5.85	1.5	10.24
1.5	10.13	-2.92	1.5	10.24
1.5	10.13	0	1.5	10.23
1.5	10.13	2.92	1.5	10.23
1.5	10.13	5.85	1.5	10.22

Table 4.2: Parameters of the input pulse and the retrieved pulse of the simulations performed with non-zero ξ_3 (fig. 4.6)

We can observe (fig. 4.6) how for small values of ξ_3 the retrieved pulse duration is not perturbed for the non-zero ξ_3 however the retrieved values of ξ_2 as function of CEO phase are modified producing an asymmetry on this curve.

4.2.2 Experimental setup

The experiment was performed using one of the 20 mJ branch of the laser system described in section 3.2.1. The pulse duration was set to 39 fs (rms) (fig. 4.7) with a central wavelength of 800 nm. The laser pulse was split to operate synchronously the THz source (60%) as well as the high order harmonic generation (40%).

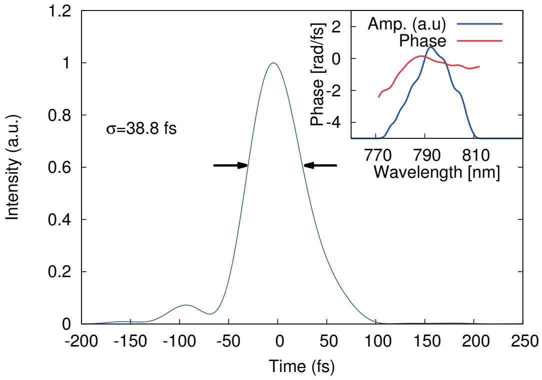

Figure 4.7: Temporal profile of the driving laser. The pulse length is 38.8 fs (rms). Inset, spectral amplitude and phase of the driving pulse, with the latter optimized for most efficient high-order harmonics generation.

To generate the High-order harmonics the 8 mJ beam is focused using a plano-convex lens with 3 meter focal length. The lens is mounted into a translation stage that allows to move it in the direction of propagation in order to adjust the position of focus.

The beam waist (85 μm, $\frac{1}{e^2}$ beam radius) was placed at the face of a 3 cm long unmodulated glass cell with 800 μm inner diameter. A solenoid-based valve situated at the center of the cell released bursts of argon with a backing pressure of up to 3 bar at the full repetition rate of the laser.

Downstream the HHG beam is focused by a toroidal mirror (focal length of 4 m) into the detection zone of the streaking chamber installed at the end of the 9 meter long HHG beam line. Two 200 nm thick aluminum filters and a fused silica plate were used to separate the HHG beam from the infrared laser.

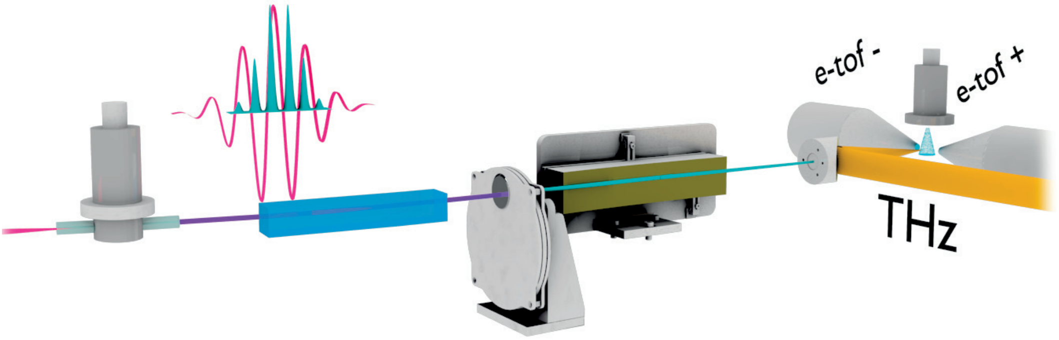

Figure 4.8: Experimental layout with high-order harmonics generated in a gas cell followed by harmonic separation (silicon plate and Al filters) and a toroidal mirror (4 m parent focal length) focusing the APT into the gas jet located in the detection zone of the two opposing time of flight electron spectrometers.

The THz generation setup consist in a 2:1 (fig. 4.9) cylindrical telescope that reduced the horizontal beam size using a pair of cylindrical lenses. Afterwards a reflective gold grating with 1800 l/mm optimized for the -1 order is used to produce the tilt of the IR wavefront. We used a spherical gold mirror (f=150 mm) to produce a 2:1 image of the grating surface in to the front surface of a $MgO : LiNbO_3$ crystal. This $LiNbO_3$ crystal produces the THz pulses by optical rectification of the IR pulses [69, 70]. Before the $LiNbO_3$ a half wave plate is used to rotate the polarization of the IR pulse in order to match the crystal axis.

After generation a 90 deg off-axis parabolic mirror is used to collimate the generated THz radiation. The generated output is vertically polarized. For our experiments we need the electric field to be in the horizontal plane (as the e-tofs). To turn the polarization we use a pair of gold mirror forming a periscope that also rotates the polarization.

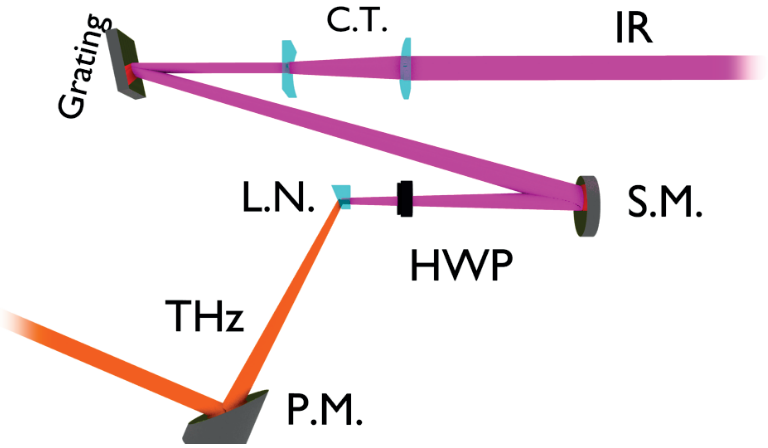

Figure 4.9: THz generation setup: C.L. is a 2:1 cylindrical lens telescope, S.M. is the spherical mirror with $r = 300\,mm$, HWP is a broadband half wave plate, L.N. the $LiNbO_3$ crystal and P.M. a 90 deg off-axis parabolic mirror with effective focal length $E.F.L = 170\,mm$

The streak camera (4.8) consists of two electron time-of-flight (e-tof) spectrometers oriented parallel to the electric field and placed at opposing sides of the gas jet. For this configuration the recorded signals of the two e-tofs are complementary. This allows the simultaneous retrieval of positively and negatively streaked electrons. The typical energy resolution of the used e-tof was around 1%. The photoelectrons were produced by single-photon ionization in different noble gases by the HHG beam. The gas was injected using a piezo controlled pulse valve with opening times typically around 20 μs with a backing pressure between 1 and 4 bars.

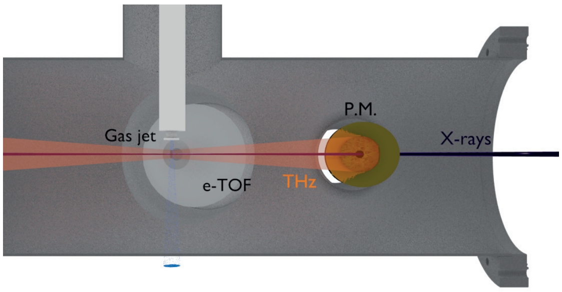

Figure 4.10: Cross section of the THz streak camera. P.M. is a 17 cm focal length off-axis parabolic mirror. The gas jet is operated in a pulsed mode delivering gas burst with a duration of around 40 μs. The vacuum level inside the gas jet is maintain below $10^{-6}\,mbar$ during operation.

4.2.3 Temporal characterization of attosecond pulse train

Calibration procedure

The first step in the experiments is the energy calibration of the time of flight spectrometer. As indicated by its own name the spectral analysis of the electron is performed via the arrival time of the electrons. The arrival time of the electron as function of the kinetic energy can be easily calculated using classical mechanics as:

$$t(E) = t_0 + \frac{L}{\sqrt{\frac{2(E-E_r)}{m_e}}} \tag{4.17}$$

where E is the kinetic energy of the electrons, E_r is the retarding potential that can be applied to lower the electron speed, L the travel length of the electron and t_0 the temporal offset. This equation can be easily inverted obtaining that:

$$E = E_r + \frac{m_e L^2}{2(t-t_0)^2} = c + \frac{a}{(t-b)^2} \tag{4.18}$$

The values of a,b and c of Eq.4.18 are obtained either by comparing with an optical spectrum or by using the fact that the harmonic lines are separated by 3.1 eV. In Xenon we can also profit from the double line structure coming from the two ionization levels.

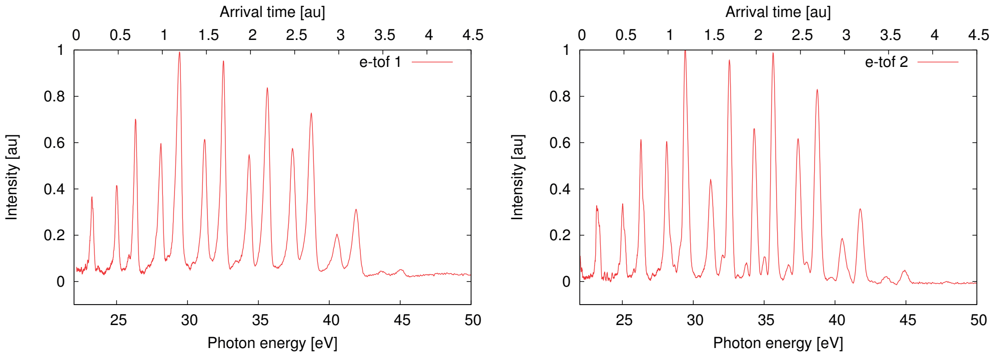

Figure 4.11: Retrieved HHG spectra from the two time of flight spectrometers using Xenon as ionization media. The obtained parameters for etof-1 (2) are: a=3.32e8 (3.35e8), b=-2972.9 (-3028.7) and c=3.243 (3.123) all these values are in au since the time of flight is as well in au.

Fig.4.11 represent a calibrated field free photoelectron spectra. It is possible to observe how the linewidth of the different harmonics are narrow enough to avoid overlap between the different ionization lines.

Once the energy calibration is performed we need to characterized the THz field and find the optimum time delay between the THz and the HHG pulse to perform the measurements. This information is obtained by recording a spectrogram or FROG-trace (Fig. 4.12). The first thing observed on the spectrogram is how the electron spectra coming for the different emission lines finally are overlapping due to the broadening that the THz electric field is producing as is predicted in Eq.4.12.

The THz electric field can be obtained directly from the energy shift induced on the electrons generated by the HHG pulse. The electric fields reconstructed using the two different e-tofs are shown in figure 4.16. To perform this calibration we can conclude that is convenient to record a full spectrogram like the one of figure 4.12.

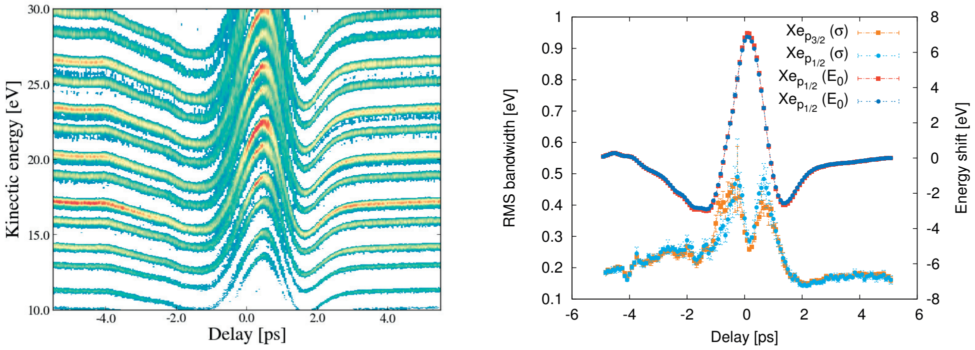

Figure 4.12: Left, recorded FROG-trace in Xenon. Right, corresponding fitting parameters for the Xe $p_{3/2}$ line.

With this measurements we can analyze individually each harmonic fitting the energy spectrum at every delay point to a double Gaussian distribution:

$$I(E) = A_0 \exp\left(-\frac{E - E_0}{2\sigma_0^2}\right) + A_1 \exp\left(-\frac{E - E_1}{2\sigma_1^2}\right) + D \tag{4.19}$$

Once the calibration is finished the unstreaked photoelectron spectrum and the streaking speed on the linear part of the vector potential are know and all the parameters needed for section 4.2 are know. To retrieve the pulse duration and the chirp of the X-ray pulses we just need to measure the photoelectron spectra under the effect of the THz field.

Xenon measurements

The first round of experiment uses Xenon as ionization media due its large photoionization cross section for the spectral range of our HHG pulses. However Xenon it has two ionization energies separated by 1.3 eV the first one the $p_{3/2} = 12.1\,eV$ and the second one $p_{1/2} = 13.4\,eV$. This separation of the spectral lines is enough to avoid the overlap but only in the field free case. Under the effect of the THz electric field due to the broadening the two spectral lines are overlapping. This makes necessary to perform a double Gaussian fit.

For each acquisition the integration time was set to one second accumulating in total 100 pulses. In addition to this we performed five measurements that are averaged and the standard deviation of this set of measurement is what is considered as the measurement error.

We calculate the pulse duration and first order chirp of the HHG pulses by comparing the width of the photoelectron spectra of the streak and unstreak cases for both e-tofs. In figure 4.13 we compare these spectra at one delay point where the vector potential has a liner slope and the corresponding electric field it has a local extrema.

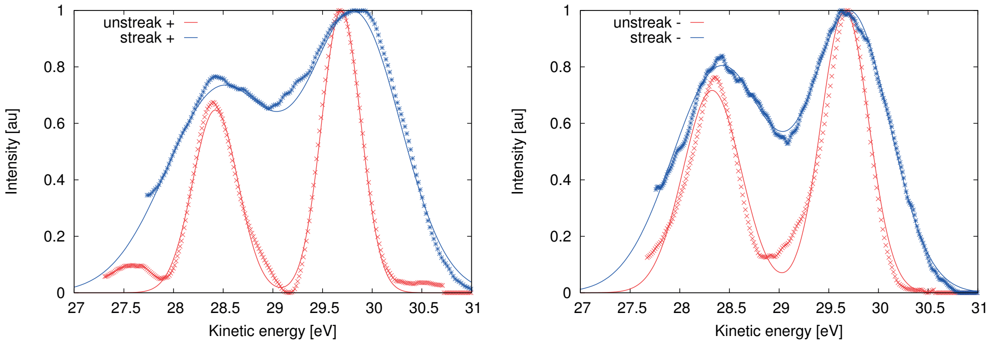

Figure 4.13: Left (right), Streaked and unstreaked electron spectrum of the harmonic 25 recorded by with positive (left) and negative (right) streaking speeds. Dots are the retrieved data and lines are the double Gaussian fit. The low energy part of the spectrum is cut due to the overlap with a lower energy harmonic.

e-tof	Delay (ps)	σ_a (eV)	s_a (meV/fs)	σ_b (eV)	s_b (meV/fs)
+	5.8	0.240 ± 0.01	$\sim 10^{-2}$	0.31 ± 0.03	$\sim 10^{-1}$
	0.583	0.46 ± 0.03	12.7 ± 0.7	0.44 ± 0.02	13.0 ± 0.5
-	5.8	0.196 ± 0.005	$\sim 10^{-2}$	0.240 ± 0.004	$\sim 10^{-1}$
	0.583	0.39 ± 0.04	-14.3 ± 0.9	0.58 ± 0.06	-14 ± 1

Table 4.3: Fitting parameters of the Harmonic 27 for the spectrum represented in figure 4.13. σ_a and s_a (σ_b, s_b) are the rms spectral bandwidth and the streaking speed of the photoelectrons produced for $\mathrm{Xe}_{p_{3/2}}$ ($\mathrm{Xe}_{p_{1/2}}$) ionization line.

In order to obtain a better statistics for our measurements and to cross-check the behavior predicted along the numerical simulations we compare the retrieved pulse duration and chirp at different values of the relative timing between the THz and the HHG pulses figure 4.14.

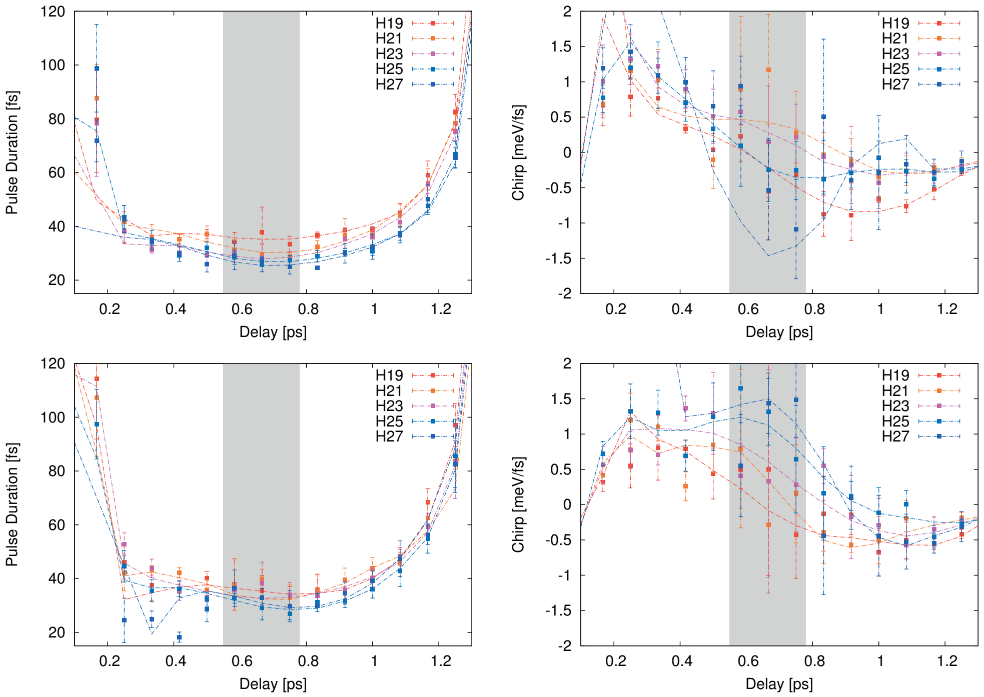

Figure 4.14: Left (right), pulse duration (chirp) as function of the time delay for the different harmonic orders. Top graph represents the value retrieved for the $\mathrm{Xe}_{p_{3/2}}$ line and the bottom one the $\mathrm{Xe}_{p_{1/2}}$. Dot are the experimental data and lines the Fourier filtered analysis performed cutting the higher frequencies in order to obtain smoother curves.

The grey area in Fig. 4.14 represent the data points within the time window where the THz electric field deviates less than 20% from the peak value. Along this area we take an weighted average using as weighting function the inverse square of the standard deviation, with this average we finally compute the pulse duration and the first order the chirp of the different Harmonics. The results are shown on Table 4.4

The asymmetry on the retrieved values of the chirp respect to the phase of the dressing fields can be attributed as it was show by the previous numerical simulations to a non-zero third order chirp.

	$Xe_{p_{3/2}}$		$Xe_{p_{1/2}}$	
Harmonic (-)	Pulse duration (fs)	chirp (meV/fs)	Pulse duration (fs)	chirp (meV/fs)
19	36 ± 11	-0.2 ± 0.1	35 ± 5	0.3 ± 0.2
21	30 ± 6	0.21 ± 0.05	37 ± 6	-0.2 ± 0.1
23	29 ± 4	0.5 ± 0.2	34 ± 7	0.5 ± 0.2
25	28 ± 3	-0.28 ± 0.01	28 ± 5	0.9 ± 0.3
27	25 ± 9	-0.6 ± 0.2	30 ± 13	1.2 ± 0.3

Table 4.4: Pulse duration and first order chirp for the different harmonics measured using the $Xe_{p_{3/2}}$ and $Xe_{p_{1/2}}$ lines.

The measurements shows how higher harmonics orders has a shorter pulse duration. This behaviour is in agreement with the cut-off law eq. (3.6). The higher orders need higher driver intensities, which are achieved during shorter periods of the driver laser. We can also observe how the retrieved pulse duration from both Xenon lines are lying within the error range. However the measurement of the first order chirp seems to be less consistent without any clear tendency in the harmonic order and furthermore a disagreement between the two different lines.

One of the major difficulties along these measurements is the fact that the photoelectron spectrum produced for the two different lines of Xenon overlap under the stretching effect of the THz field. To avoid the spectral overlap is possible to replace the ionization medium from Xenon to Helium. With its single ionization energy at 24.6 eV and lower ionization cross-section Helium will produce a significantly less charged electron beam and therefore reducing the space charge forces.

Helium measurements

The following measurement were performed using Helium as ionization medium. The opening time of the gas jet it was set to 40 μs and the back pressure was set to 3 bars. The other experimental parameters were maintained to be able of having a comparison with the previous measurements performed in Xenon.

Helium has a single ionization energy located at 24.6 eV this sets the harmonic order 17 as the lower harmonic that can be observed as we show in the calibration spectrogram of fig. 4.15.

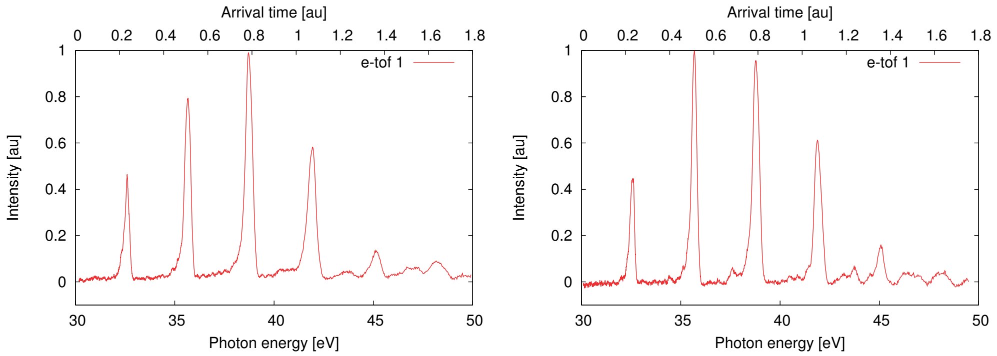

Figure 4.15: Retrieved HHG spectra from the two time of flight spectrometers using Helium as ionization media. The obtained parameter for etof-1 (2) are : a=4.485e7 (5.754e7), b=-1389.9 (-1507.1) and c=0.15 (-0.47) all these values are in au since the time scale of the scope was as well in au.

Proceeding as we did in Xenon, we characterized the THz pulse and the field free photoelectron spectrum. In this case due to the single ionization line a single Gaussian distribution is fitted to the photoelectron spectrum at each delay point. Figure 4.16 shows the recorded spectrogram for Helium and the retrieved THz electric field calculate from the energy shift of the photoelectrons.

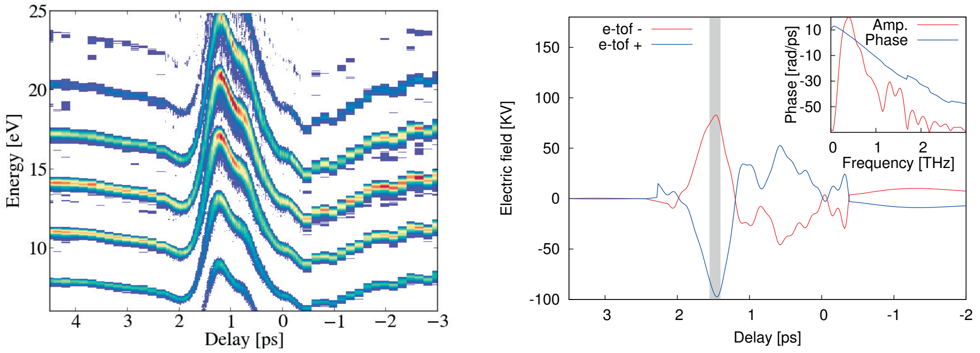

Figure 4.16: Left, photoelectron spectrum as function of the time delay. Right, THz electric field calculated from the electron energy shift.

It is possible now to compare the streaked and unstreaked electron spectra to obtain the pulse duration and chirp of the HHG pulses.

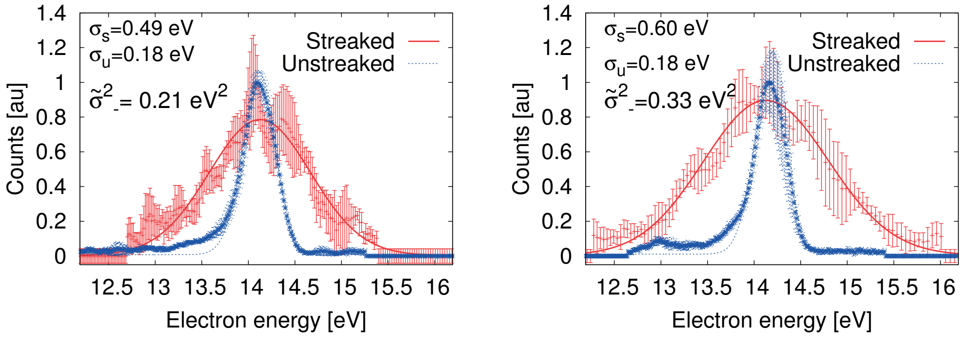

Figure 4.17: Left (right), Streaked and unstreaked electron spectrum for etof + (etof -). Both signals streaked and unstreaked are normalize to its maximums.

Following the same procedure that during the Xenon measurements we performed the measurement in the area around the peak of the electric (gray are in figs. 4.17 and 4.18 and we take a weighted average for the values of the pulse duration and chirp of the different harmonics table 4.5.

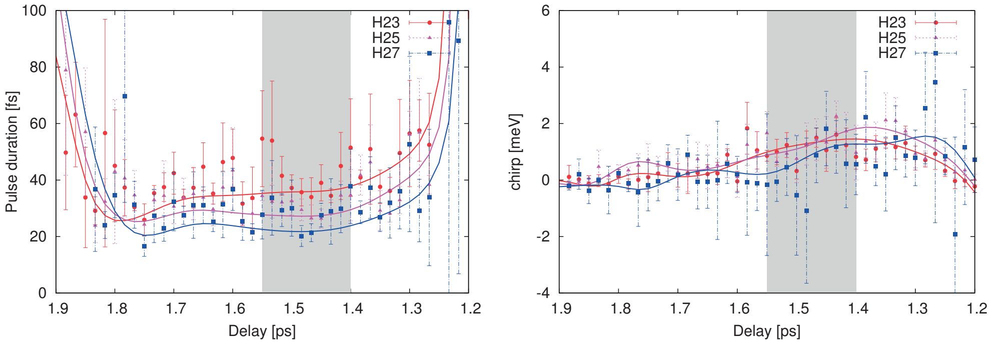

Figure 4.18: Pulse duration (left) and first order chirp (right) as function of the time delay. Discrete point represent the averaged experimental data. Lines represents the values obtained after applying a low-pass filter to the retrieved values of the streaking speed and spectral broadening as function of the time delay.

Harmonic [-]	**Pulse length (rms) [fs]**	**Chirp [meV/fs]**
23	36 ± 5	-0.96 ± 0.08
25	32 ± 4	-0.91 ± 0.1
27	24 ± 2	-0.82 ± 0.1

Table 4.5: Summarized results from 4.18. The pulse duration and chirp is calculated as the weighted average over the region where the approximation $\cos \omega_{THz} t \approx 1 - \frac{\omega_{THz}^2 t^2}{2}$ is valid (grey area).

The retrieved pulse duration shows as in the case of Xenon a tendency where higher order harmonics show a shorter pulse duration. We can see how the measured pulse duration in Xenon and Helium are in agreement within the experimental error. The asymmetry on the retrieved value of the chirp as function of the time delay is as well observed indicating the non-zero value of the second order chirp.

Conclusions

This section has presented a detail description of how to use a Streak camera to characterize ultrashort X-ray pulses. Furthermore using THz as dressing field we have been able to perform the measurement of the pulse duration for the individual harmonics that are present in an attosecond pulse train.

It is import to be able to measure the pulse duration of the individual information because many different application are using only one of this harmonics as element selective probe for ultrafast dynamics.

The technique has show to have the capability to perform a shot-to-shot measurement of the X-ray pulse [27]. This is beneficial for X-ray sources with poor shot-to-shot stability or with low number of pulses per second. Furthermore the streak camera is a technique that is less sensitive to the space charges produces by high X-ray source than other characterization techniques as FROG-CRAB or RABBIT.

The measurement of the pulse duration using the Streak camera technique has been prove to be very consistence obtaining very similar results in the case of the three different measurements ($Xe_{p_{3/2}}$, $Xe_{p_{1/2}}$ and Helium). Nevertheless the experimental error is in the other of 10% being slightly higher in the case of Xenon due to the less accurate fitting of the double peak structure.

In all the cases a clear tendency has been observed where higher order harmonic have a shorter pulse duration. This behavior is in full agreement with the cut-off law eq. (3.6) since the intensity window where these harmonic can be produced is shorter.

The observed behavior on the retrieve pulse duration and chirp as function of the phase of the dressing field is in agreement with the one predicted along the numerical simulations allowing as to anticipate the presence of a second order chirp in our HHG pulses.

5 Ultrafast Magnetization dynamics

Contents

While magnetism was discovered by mankind in the IV century B.C. it was only during the XIX century that many different authors started to study magnetism and related phenomena systematically. These results were synthesized in 1862 by James Maxwell [71] in a set of four differential equations. Later on, in the XX century with the development of quantum mechanics the origin of magnetism could successfully be described using different models like the Heisenberg model [72] or the Ising model [73].

Magnetism has remained a hot topic in research as various questions are still unanswered. The new frontiers on magnetism are linked to the advances of other research fields. For example, recent developments in nano-technology and nano-science allow to produce magnetic systems where the magnetism originates from the geometrical frustration [74] (spin ice). These systems show properties very similar to magnetic monopoles. Also, the opportunity to produce thin films of different compounds provide the possibility to study the magnetic properties at the interfaces between different compounds [75]. This enables the observation of magnetic properties in materials which are otherwise non-magnetic. In a similar way the novel opportunities offered by ultrafast science have opened the possibility to study the dynamics of magnetism with unprecedented temporal resolution.

The investigations of ultrafast magnetic phenomena induced by a laser were started in 1996 by Beaurepaire and co-workers [9]. In his pioneering work, Beaurepaire studied the magnetization dynamics on Nickel when it was exposed to an intense femtosecond laser pulse. This work inspired the description of the magnetization dynamics, or more correctly magnetic quenching, by a three temperature model. In this model the laser pulse produces an increase of the electron temperature. The electron releases a large part of his kinetic energy via collisions with the atomic lattice and also the different spin populations are modified due to the spin dependent electron scattering. Later on many different studies have been performed to understand and control the magnetization dynamics on the femtosecond time scale. Some of these works are based on the resonant excitation of spin waves [76].

The advent of ultrashort X-ray pulses give the researchers a new tool at hand to combine the temporal resolution provided by ultrafast lasers with element-sensitive techniques to probe the magnetization dynamics. The element sensitivity helps to disentangle the magnetization dynamics of different compounds in complex magnetic system.

In this chapter we present the work we have performed in ultrafast magnetization dynamics. The work can be divided in two major section: the first one studies magnetization dynamics in cobalt under the presence of a strong THz field. In this work we show for the first time an off-resonant and phase-locked control of the magnetization dynamics at the femtosecond time scale. The results of the work are published in [77]. The second part of this chapter presents first results using our HHG source as element selective probe for magnetization dynamics in a multi-layered CoPd thin film. Element sensitivity is fundamental to avoid spurious effects produced by other non-magnetic changes produced by the intense laser. Element sensitivity allows to distinguish the time scale of the dynamics for the different elements of the sample.

5.1 Off-resonant coherent control of magnetization dynamics

In this section, we present the results on the coherent control of the magnetization dynamics using the intense magnetic field of a THz pulse. In this research [77] we present the first observation of a coherent, phase-locked coupling between the magnetic dipoles of a ferromagnetic thin film of Cobalt and the external magnetic field of our single-cycle THz pulse [28]. Previous works relied on heat produced by a near infrared laser pulse increasing the electron temperature above the Curie temperature. Using laser heat, it was possible to observe an ultrafast demagnetization on the 100 femtosecond time scale. However, the thermalization process required for restoring the intital magnetization happens on a larger time scale up to nanoseconds.

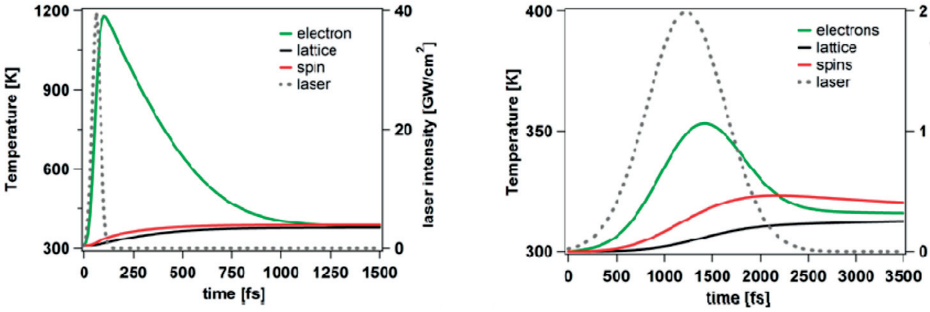

Figure 5.1: Temporal evolution of the electron (green) lattice (black) and spin (red) temperatures after a laser excitation (dotted). Left, using a near IR pulse. Right, using a THz pulse.

The incoherent nature of heat prevents the observation of any coherent phase effect on the demagnetization dynamics as the heat stimulus is defined purely by the intensity envelope. Using our THz stimulus it is possible to obtain a coherent, phase-locked control of the magnetization dynamics. This is possible because in contrast with nIR pulses THz pulses keep the electron temperature below the Curie temperature fig. 5.1. Under these conditions, the magnetization of the sample is conserved and the magnetic dipoles can couple to the external magnetic field of the laser. The dynamics of ferromagnet under the effect of a time-dependent magnetic field can be described using the Landau-Lifshitz-Gilbert (LLG) equation:

$$\frac{dM}{dt} = -\gamma M \times H_{eff} - \lambda M \times (M \times H_{eff}) \tag{5.1}$$

where $\vec{M}$ is the magnetization, $\vec{H_{eff}}$ is the effective external magnetic field, γ the gyromagnetic electron ratio and λ is a phenomenological damping parameter. The first term of this equation describes the precession of the magnetic dipoles around the external magnetic field. The second term describes damping that tends to orient the magnetic dipoles along the external magnetic field.

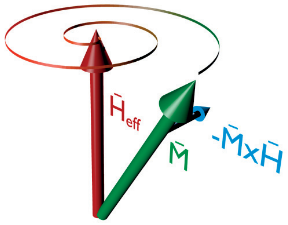

Figure 5.2: Scheme of the vectorial products involves in the LLG model. The term $\vec{H} \times \vec{M}$ produce the precession of the magnetic dipoles around the axis of $\vec{H_{eff}}$. The damping term is the responsible to produce the alignment of the magnetic dipole to the external magnetic field.

In this research, we observed for the first time off-resonant femtosecond magnetization dynamics driven by the intense magnetic field of a THz pulse carrying a stable absolute phase. The phase-locked opto-magnetic mechanism presented here could be of interest for next-generation storage technology as the field-controlled mechanism enables ultrafast reversible interaction.

In the following we first describe the experimental setup and the THz source employed throughout this research. Then the experimental results are presented which are excellently reproduced by LLG.

5.1.1 Experimental setup

The experiments are performed using a 20 mJ, 50 fs Ti: Sa laser system. The output of this laser system is used to pump a three stage white-light-seeded optical parameter amplifier (OPA) delivering a pulse energy up to 4 mJ at a central wavelength of 1.5 μm at . For THz generation in organic crystals a laser beam size of $\phi = 6mm$ is set to achieve intensities of 140 $\frac{GW}{cm^2}$ in the organic DAST crystal(4-N,N-dimethylamino-4'-N'-methyl stilbazolium tosylate). The THz radiation is separated from the pump laser by a 3 mm thick Teflon filter. The THz pulses are linearly polarized and the direction of polarization can be adjusted simply by rotating the NIR polarization and correspondingly the organic crystal to maintain phase-matching conditions. The characterization of the THz source is performed using an electro-optical (EO) sampling setup [28, 78]. The EO crystal is a 100 μm thick Gallium Phosphide crystal.

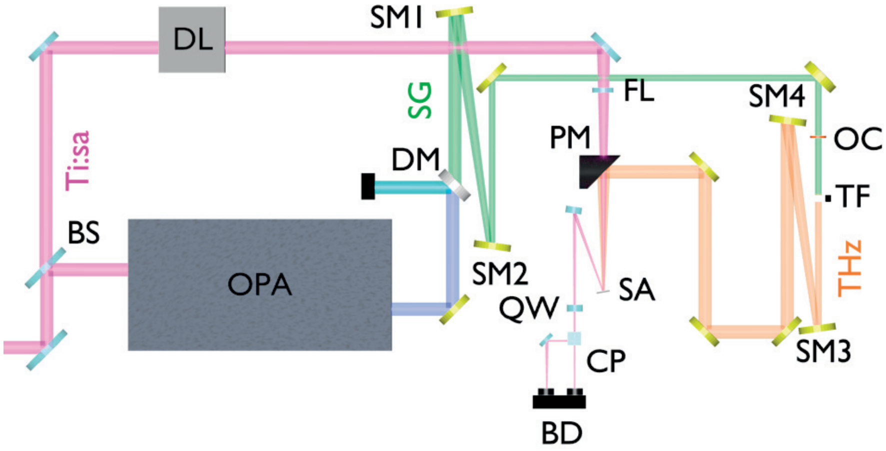

Figure 5.3: Scheme of the experimental setup. The signal and idler generated in the OPA are separated using a dichroic mirror (DM). SM1 and SM2 are spherical gold mirror used as a 2:1 telescope. SM3 and SM4 are spherical gold mirrors used to double the THz beam size. OC is the organic crystal and TF the Teflon filter. BS is the beam splitter used to pick up the probe pulse. SA is the cobalt sample. PM is the 5 cm focal length parabolic mirror used to focus the THz on the sample and to produce the overlap with the probe pulse. The probe is focuses on the sample usig a lens (FL). QW, CP and BD are a quarter wave plate, cube polarizer and a pair of balanced photodiodes for polarization analysis.

In the time domain, the generated THz radiation carries 1.5 cycles with the electric field being phase locked to the intensity envelope. The peak magnetic field is 0.3 Tesla. The THz spectrum is octave spanning and centered at 2.1 THz. These pulse characteristics have been measured directy at the position of the interaction with the magnetic thin film. Indeed, the magnetic thin film can be replaced by an EO crystal for this purpose. The magnetic sample consists of a 10 nm thick cobalt film covered with a

3 nm Al layer. The Cobalt is evaporated onto a Si/Pd base substrate. Before the Cobalt is deposited, the substrate is covered with 2 nm of Palladium. The aluminum cover prevents oxidation of the Cobalt and is transparent to the THz and the probe pulse. Its hcp crystalline structure exhibits an in-plane isotropy with the c-axis normal to the surface.

The magnetization is characterised using the magneto-optical Kerr effect (MOKE). MOKE rotates the polarization of the incident NIR pulse after it is reflected by the magnetic sample. The rotation of the polarization originates from the symmetry-break of the dielectric tensor induced by the magnetization. To probe this effect a small portion of the Ti: Sa laser is used, enabling an excellent synchronization between the THz pump and the NIR probe.

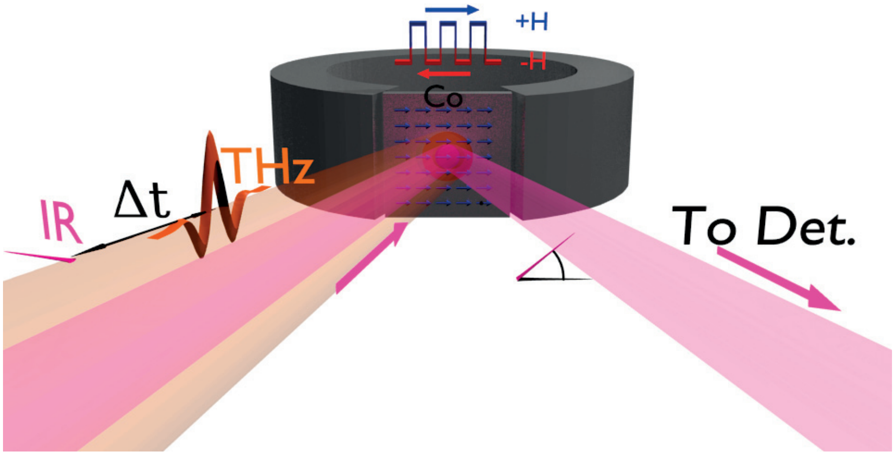

Figure 5.4: Experimental setup. The incident angle of the THz and IR beam on the Co sample is 10 deg from normal the normal. The reflected NIR beam is sent to the balanced detection scheme for determine the induced rotation angle of polarization. The Co sample is embedded in an alternating magnetic field which induces an initial orientation of the magnetization perpendicular to the THz magnetic field. The polarization of the NIR probe is parallel to the external magnetic field.

The magnetization of the cobalt sample is oriented by an external DC magnetic field from an electromagnet. The direction of the magnetic field can be inverted between laser pulses. This fact is used to improve the signal-to-noise ratio of the Kerr-rotation measurement. The polarization of the probe is measured by means of a half-wave plate set to 45 degrees with respect to the probe polarization. A cube polarizer separates the beam into the horizontal and vertical polarization components and the two spatially separated beams are then sent towards a pair of balanced photodiodes.

5.1.2 Experimental results

As a model system we use a 10 nm thin cobalt film. The film exhibits an in-plane magnetization due to shape anisotropy and was used at room temperature throughout the experiment. The sample is exposed to an external field B_{ext}, oriented 10 deg from the cobalt plane. The field was used to drive the macroscopic magnetic moment to saturation (Fig. 1). The linearly polarized terahertz pulse impinges onto the sample surface with an angle of incidence of 20 deg from the sample normal. The sub-50 fs probe pulse (λ=800 nm) used for sampling the terahertz-induced coherent magnetization dynamics via the magneto-optical Kerr effect (MOKE)follows the THz beam collinearly.

The measured time-resolved MOKE signals are presented in fig. 5.5 (red line). Obviously, the magnetic response driven by the THz stimulus is significantly different to the heat-induced spin response. The THz-driven magnetization dynamics are phase-locked with the terahertz magnetic field (blue dots). The MOKE signal exhibits a quarter period phase shift (50 fs delay) respect to the driving terahertz magnetic field. In fig. 5.5 the MOKE spectra (red lines) is compared with the THz spectra (blue lines) revealing a quasi-identical spectral response. This indicates that the observed magnetization dynamics do not rely on resonant excitation [76] or Larmor precession. Contrary to previous results [9], the subpicosecond magnetic response presented here is fully dominated by the phase of the terahertz stimulus.

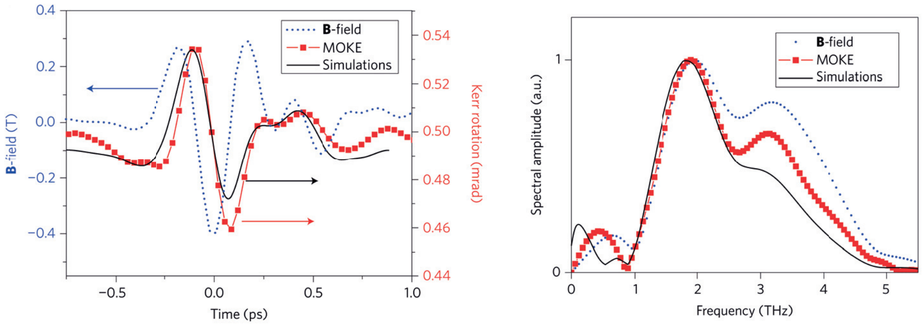

Figure 5.5: Left, Kerr-rotation (red curve) induced by the intense THz field (blue curve). Right, Spectral analysis of the magnetization dynamics (blue) and the THz pulse (red). In both cases the black curve represents the LLG simulations.

Using the LLG equation, a simulated MOKE response can be calculated via the micromagnetics simulation package OOMMF [79]. This is plotted in fig. 5.5 (black curves), and shows extremely good overall agreement with the experimental measurement. This good agreement also indicates that the co-propagating electric field has only a negligible influence on the magnetization dynamics at this timescale.

Such a phase-locked interaction between stimulus and magnetization far off any magnetic resonance has never been reported previously. This novel regime has become accessible due to the absence of hot electrons. Indeed, the use of THz pulses avoids extensive heating. This enables the observation of the phase and field sensitive coherent motions of the dipole magnets. With our measurements of $\vec{M}(t)$ (fig. 5.5) we show that the phase properties of the magnetization are determined by the terahertz magnetic field. This is the reason why we refer to this phenomena as "off-resonant coherent magnetization dynamics". The conventional approach based on heating the electronic and spin system above the Curie temperature produces a decrease in the macroscopic magnetization magnitude $|\vec{M}|$. In our studies, the coherent coupling affects exclusively the orientation of $\vec{M}$ and not its net magnitude.

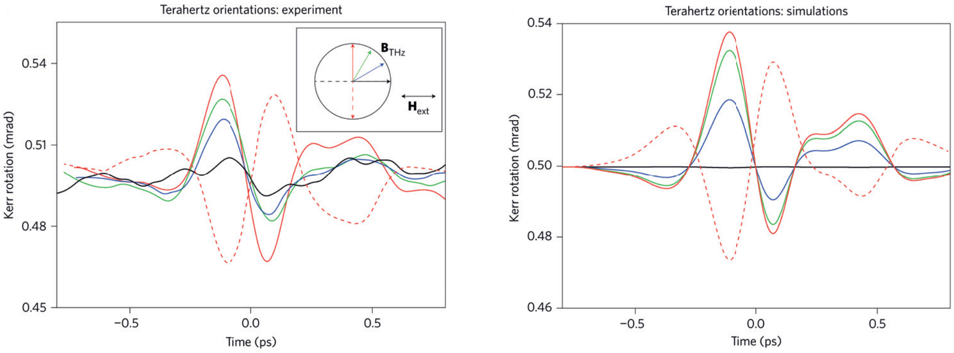

Figure 5.6: Evolution of the Kerr-rotation as function of the angle between the THz magnetic field $\vec{B}$ and the magnetization vector $\vec{M}$. Left curve, experimental data. Right curve, results form the LLG simulations. Green and blue curves correspond to an angle of 60 and 30 deg between $\vec{B}$ and $\vec{M}$ respectively. The black curves represents the case for parallel alignment between the magnetization vector and the THz field. In the latter case the THz field does not couple to the magnetization. Red dotted curve represents a 180 deg rotation of the THz magnetic field respects to the red solid curve.

We furthermore investigated the vectorial nature of the coupling by changing the vector direction of the terahertz field. We experimentally observed that the magnetization response is proportional to the sinus between $\vec{B}$ and $\vec{M}$ (fig. 5.6). The LLG equation can accurately describe this effect (fig. 5.6), indicating that the reduced angle between the terahertz field and the cobalt moments results in a smaller magnetic torque. The observed variation of the MOKE signal for parallel alignment of the terahertz B-field and sample magnetization (black curve in fig. 5.6) reflects the noise level of our experiment. The measurement and simulation performed with a terahertz stimulus with reversed magnetic field polarization result in a likewise inverted MOKE signal (solid and dashed red lines in fig. 5.6). The magnetic response for the two polarizations produces the same temporal shape and spectral components, providing evidence of the phase-locked coupling mechanism, which would not be expected for incoherent heating.

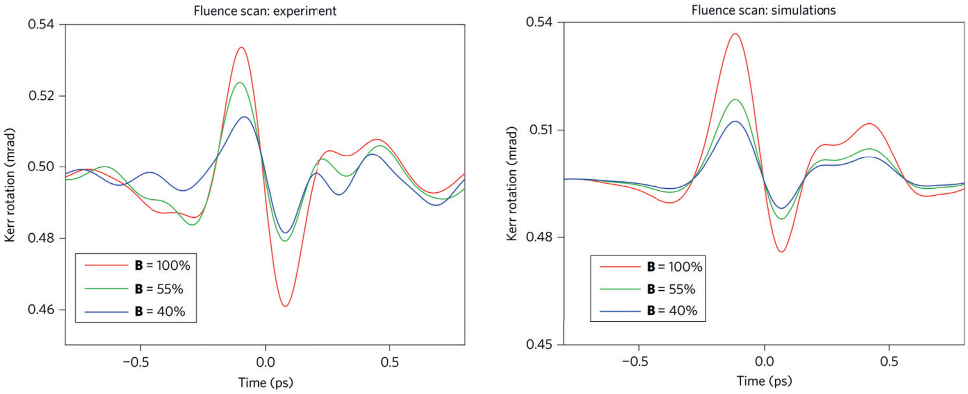

Figure 5.7: Left (right) experimental (simulated) MOKE response as function of the THz magnetic field strength. For all these measurement orientation of the THz magnetic field was orthogonal to the magnetization vector. This measurement show a linear response of the induced Kerr-rotation with the THz field strength.

Over the investigated range, the out-of-plane magnetization is inherently linear with respect to the magnitude of the terahertz field (fig. 5.7). Three MOKE traces are recorded for different field strengths down to 40% of the maximum. The experimental and simulated curves demonstrate a proportional relation between the amplitude of the stimulus and the MOKE responses. As the terahertz magnetic field strength varies, the timescale of the magnetization response and its spectral components remain substantially unchanged. This confirms that the observed dynamics occur far from saturation and in the absence of dissipative processes.

5.2 HHG probing of magnetization dynamics

In the experiment described in the previous section the magneto-optical Kerr effect (MOKE) was used to probe the magnetic state. Using MOKE, the magnetization state of a system can be deduced from the degree of rotation that is induced on the probe polarization by the change of magnetization. Macroscopically, MOKE shows a linear dependence of the dielectric tensor with the magnetization degree of the system. Quantum mechanically, MOKE is related to transitions of electrons that are located in the valence band. The electron density of states of this band is spin-dependent, presenting an asymmetry proportional to the degree of magnetization (see fig. 5.8).

The valence band has a continuum energy spectrum. This continuum makes optical transitions exited by photons of the probe with wavelength between 0.2 and 10 μm insensitive to the photon energy. The absence of such well defined absorption edges makes impossible to distinguish the atomic element whose magnetic state shall be probed. Furthermore, optical excitations may produce changes in the population of the exited states and the ground state symmetry. This purely electrical effect may change the magneto-optical response measured by MOKE even if the magnetic state of the system has not be changed.

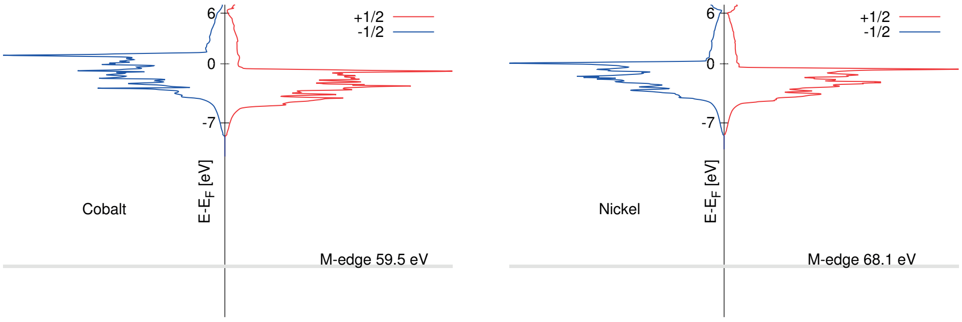

Figure 5.8: Density of states calculated using FLAPW [1] for Cobalt (left) and Nickel (right). The density of states are different for spin-up (+1/2) and spin-down (-1/2) electrons.

To overcome the limitations given by optical MOKE the magnetic states can be probed by X-rays. With the X-rays, one probes electronic transitions from the inner shell to the valence band, where magnetism is established. The use of inner shells with well-defined energy levels fig. 5.8 allow to distinguish the dynamics occurring on different atomic elements. Furthermore, the effects of the magnetization will only appear at the resonance wavelengths. This makes possible to distinguish the magnetic origin from other spurious optical and electronic effects. There are two main mechanisms for probing the magnetization using X-ray. The first one, X-ray magnetic circular dichroism (XMCD) uses the relation between the intensity of the different absorption edges (L_I, L_{II}, M_I, M_{II} ...) and the amount of empty states in the conduction band. This relationship is establish directly by the orbital sum rules [80]. The second technique, X-ray Magneto-optical Kerr effect takes advantage of the strong energy dependence of the MOKE around the absorption edges of different atoms allowing to perform an element selective probing of the magnetization dynamics

In the following sections we investigate the use of the two different techniques by means of a high-order harmonic x-ray source. High-order harmonics sources are ideal for these techniques since the short pulse duration provides a temporal resolution on the order of a few femtoseconds. Furthermore, the broad spectrum of a HHG source allows to probe the adsorption edges of different materials at the same time.

5.2.1 X-ray magnetic circular dichroism

In principle, XMCD requires the use of circularly polarized light. Nevertheless, we remind that linearly polarized light is a composition of right and left handed circularly polarized light with a given phase shift related to the polarization angle. But how can we exploit this in HHG experiments? If we try to observe XMCD effect on a magnetized sample using linear polarized light, the change of reflectivity induced by the magnetization will be zero, as the contributions from the right-handed and left-handed components are opposite. However, we can use magnetic samples where the magnetization is distributed on magnetic domains with the direction alternating between out-of-plane and into-the-plane. When the linearly polarized light pass through such a sample structure, the domains with magnetization pointing up induce a phase change of Δ in the right-handed polarization component and $-\Delta$ for the left-handed component. In domains with magnetization direction pointing down the phase changes are opposite. The difference in phases induced by the magnetic domains produces the diffraction of the transmitted radiation. It is important to remark that only the spectral component of the incident radiation where the magnetic asymmetry is present are diffracted. Using the intensity of the diffraction pattern we are able to probe the magnetization of magnetic system [81, 10].

We investigated two different magnetic samples consisting of a 20-layer stack of palladium and cobalt. The cobalt palladium ratio of sample 1 is Co(0.4 nm)/Pd(0.6 nm) while sample 2 is Co(0.4 nm)/Pd(0.2 nm). The deposition is performed by magnetron sputtering on a 30-nm thin Si_3N_4 membrane array placed on a Si chip. The stacking composition give rise to an out-of-plane magnetic anisotropy. The samples have been demagnetized prior to the experiment and exhibit aligned stripe domains with the pointing direction of the magnetization alternating between up and down.

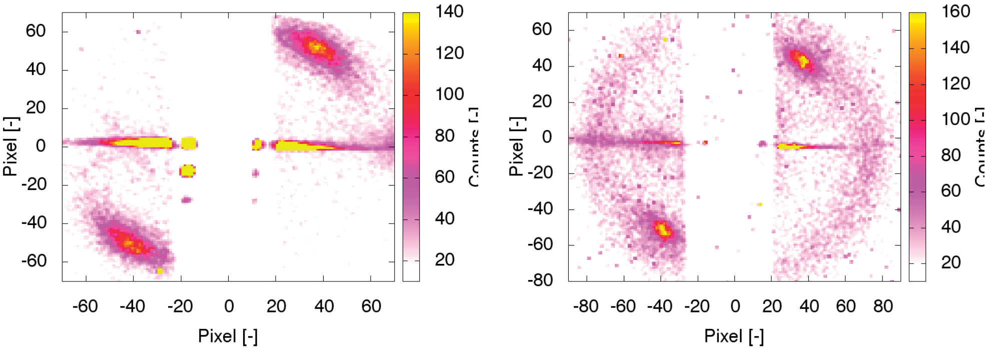

Figure 5.9: Diffraction patterns for a fresh sample (left) and after exposure to a laser fluence of approx. 8 mJ cm^{-2} (right).

In fig. 5.9 the diffraction pattern produced by these samples are shown. The left side of the image is a diffraction pattern prior to irradiation with an IR pulse. The right image is the diffraction pattern after the sample has been irradiated with an intense IR pulse. The main difference between the two patterns is the presence of a diffraction ring present for the irradiated sample. This appears due to the strong demagnetization produced by the IR radiation. After being demagnetized the domains are randomly reoriented due to the weak remaining magnetization of the sample.

Using the XMCD diffraction technique we performed first preliminary studies on thermally induced demagnetization dynamics. To perform these experiments, we used a small portion (up to 100 μJ) of the Ti:sapphire laser driving the HHG process. The pump pulse is focused onto the sample by a lens (f=1 m). For HHG a pulse energy of 18 mJ is focused into an elongated gas cell using a lens with f=3 m. The gas cell is periodically filled with Neon by a pulsed valve with 3 bar backing pressure and 300 μs of opening time. The generated HHG radiation is focused by a Toroidal mirror that images the output of the gas cell onto the magnetic sample. The spatial overlap fig. 5.10between the NIR pump and the HHG probe is achieved thanks to a thin gold coated silicon wafer (M2) that allows to establish a small angle between both beams.

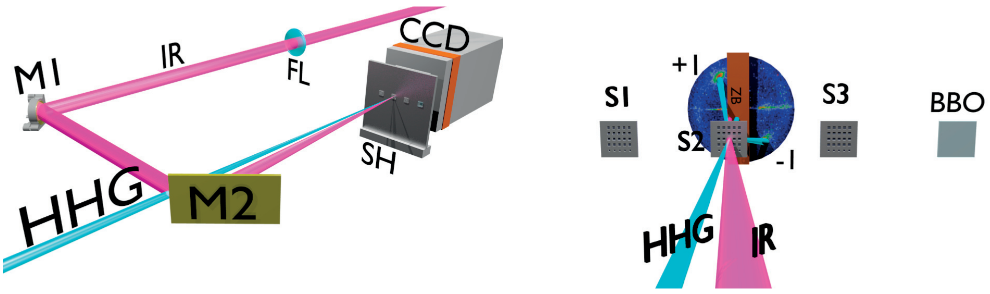

Figure 5.10: Experimental setup for XMCD with HHG. The NIR beam is focused onto the sample using a focusing lens (FL) with $f = 1\,m$. M1 is a gold flat mirror. M2 is a gold coated silicon wafer. The samples, placed in a dedicated holder (SH), can be translated perpendicularly to the beam to selected different samples. A BBO crystal is also installed on the sample holder for temporal diagnostics. The zero order of diffraction as well as the pump are blocked using a flat copper wire (ZB). The CCD is cover with a thin (200 nm) Aluminium foil to filter out any remaining IR pump. The HHG beam is focused into the samples under normal incidence using a toroidal mirror (fig. 3.14.

To characterize the magnetization state of the sample the intensities of the diffraction orders +1 and -1 are measured. For the pump-probe measurements we acquired diffraction pattern with an integration time of 5 seconds with a CCD, typically employing a binning of 5x5 pixels. Figure 5.11 represents the magnetization state as a function of the time delay between the X-ray probe and the IR pump for three different pump intensities. The demagnetization curves are fitted using the equation given in [82]. This equation is a solution of the three temperature model [9, 83] for demagnetization dynamics under the following assumptions: The electron temperature rises right after the laser excitation and the spin specific heat is ignored at low fluence. With this assumptions, temporal evolution of demagnetization can be expressed as:

$$\frac{\Delta M}{M_0} = \left[\left(\frac{A_1}{\sqrt{t/t_0+1}} - \frac{A_2\tau_e - A_1\tau_m}{\tau_e - \tau_m} e^{\frac{-t}{\tau_m}} - \tau_e \frac{A_1 - A_2}{\tau_e - \tau_m} e^{\frac{-t}{\tau_e}}\right)\Theta(t) - A_3\delta(t)\right] \times P(t) \quad (5.2)$$

The main parameters in this equation are: τ_m the demagnetization time, τ_e the electron relaxation time. A_1 is related to the magnitude of the magnetization when electron and lattice are back to equilibrium. A_2 is proportional to the increase of electrons after the laser excitation. A_3 takes into account the state filling effects during the pump-probe overlap. Here A_3 is set to 0 as this effect is not observed. P(t) is the intensity envelope of the laser pulse. In our case, we use a Gaussian pulse with a pulse duration of 25 fs (r.m.s). $\delta(t)$ and $\Theta(t)$ are the delta and step functions.

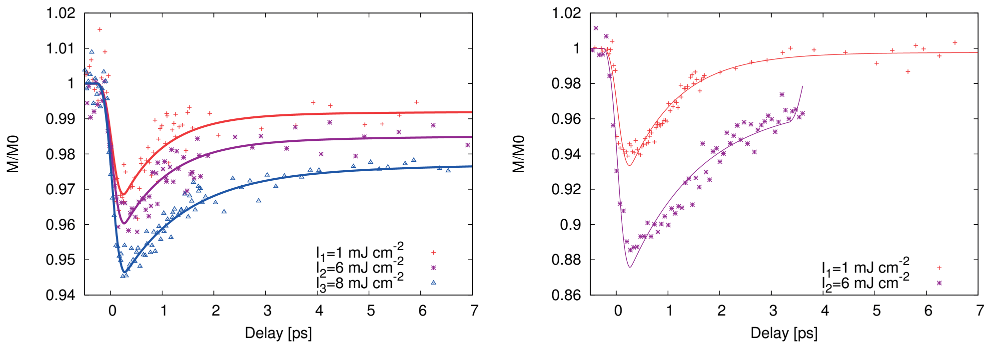

Figure 5.11: Demagnetization curves of sample 1 (left) and sample 2 (right) for different pump intensities. Fitting parameters are given in table 5.1.

		Sample 1			Sample 2	
Intensity $[mJcm^{-2}]$		$\sim$1	$\sim$6	$\sim$8	$\sim$1	$\sim$6
Parameter	$A_1[x10^{-3}]$	8.7 ± 0.1	43.7 ± 0.4	67.4 ± 0.2	2.5 ± 0.2	33 ± 2
	$A_2[x10^{-3}]$	3.9 ± 0.1	128 ± 2	163 ± 1	85 ± 1	143 ± 1
	τ_m [fs]	31 ± 5	32 ± 4	32 ± 2	40 ± 3	27 ± 3
	τ_e [fs]	830 ± 30	920 ± 30	1260 ± 20	970 ± 20	>1400

Table 5.1: Fitting parameters for eq. (5.2) for the different samples and intensities of fig. 5.11.

For the first sample, our measurement reveals a demagnetization time close to the pulse duration of the pump pulse and also to the value obtained for the HHG probe. In general, the obtained demagnetization are shorter that the ones by previous works [10, 82] however, these are the first set of measurement and further investigations are required. We also observe an increase of the relaxation time with increased laser intensity. For the second sample, there is a large discrepancy between the results obtained for the two different intensities which make it difficult to draw a final conclusion. However, there are indications that for the same pump fluence sample 2 shows a stronger demagnetization than sample 1. Next steps for these pilot experiments are to improve the signal-to-noise ratio by using a different detection scheme where the zero order is rather attenuated than fully blocked. This way, it is possible to use this beam to obtain a normalization factor to compensate the intensity fluctuations of the HHG radiation. The use of a different, more sensitive detection system such as the use of multichannel plates is also under investigation. Another possibility is to combine these measurements with the strong THz pulses as we did in the previous section. However, to perform such studies fully magnetized sample are required. As mentioned before the use of XMCD requires either circularly polarized X-rays [84] or as here presented the use the diffraction from magnetic domains. To overcome this limitation we explore the use of the magneto-optical Kerr effect (MOKE) using our HHG source as element selective probe for magnetization dynamics.

5.2.2 X-ray magneto-optical Kerr effect

In the X-ray spectral region the magneto-optical Kerr-effect (MOKE) becomes very sensitive to the photon energy of the probe beam. In particular, around the absorption edges of the different atomic elements, the dependence of the dielectric tensor with the magnetic state of the system becomes very pronounced allowing to perform an element sensitive probing of the magnetism. In opposition with the case of IR probing in the X-ray domain, is sufficient to compare the intensity of the reflected light as a function of the magnetic state, without the need of polarization analysis.

Using XMCD diffraction, the magnetization state of the system is probed by analysing the intensity of the recorded diffraction order. The spectral content of the diffracted orders corresponds to the spectrum of the magnetic edges and no spectral analysis is required. Using MOKE, however, we need to analyse the spectrum of the X-rays reflected by the sample. The experimental setup for the MOKE using x-rays as probe beam is described in fig. 5.12.

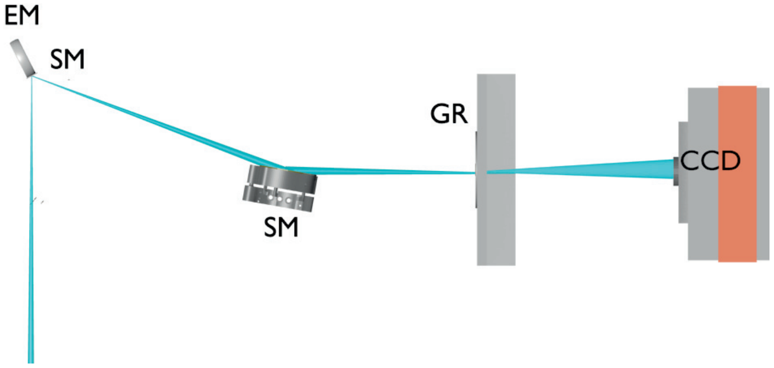

Figure 5.12: Setup for time-resolved X-ray magneto-optical Kerr-effect experiments. EM is the electro-magnet used to induce the magnetization of the sample (SM). SM is an spherical gold mirror used to produce a line focus on the CCD plane. GR is a diffraction grating with 2000 l/mm placed at 200 mm from the CCD plane.

After setting up a T-MOKE scheme at our HHG beamline we achieved first preliminary results at the M-edge in cobalt samples. A Ti:Sa laser is used to drive the HHG process in Neon and the generated X-ray beam is focused onto the cobalt sample using a toroidal mirror under grazing incidence. The spectrum of the reflected radiation is analysed by means of a transmissive gold grating (2000 g/mm) and a spherical gold mirror to obtain a line focus on the CCD plane. The magnetic field strength applied to the sample was approximately 100 mT. The magnetic asymmetry is obtained by comparing the HHG spectra obtained for two opposing magnetic field directions fig. 5.13.

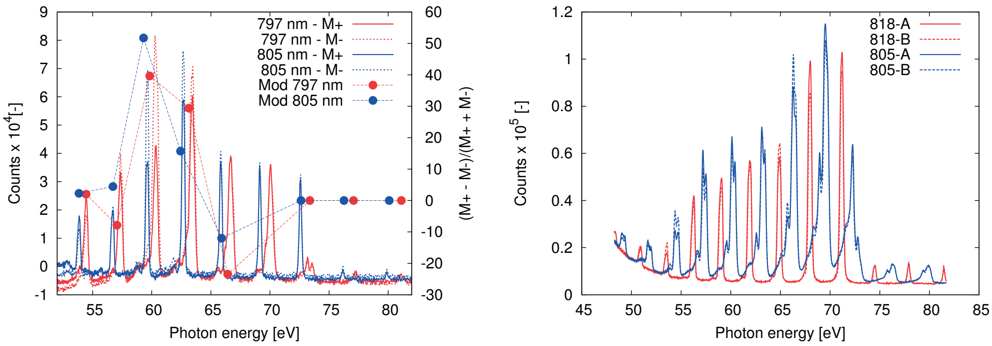

Figure 5.13: High-harmonic spectra recorded after the reflection on the cobalt sample left with magnetic field pointing up (red) and down (blue), respectively. The right figure represents the spectra recorded for a permalloy sample (80% nickle, 20% iron).

Using the wavelength-tuning capabilities of our laser system we tuned the laser to two different central wavelengths (800 nm and 810 nm) in order to change the harmonic wavelength around the resonant M-edge of cobalt (59.5 eV). For a drive laser centered at 800 nm the resonant M-edge lies between the harmonic 37 (57.35 eV) and 39 (60.45 eV). Using a laser centered at 810 nm results in a harmonic 39 which is at 59.7 eV. This results in a large asymmetry fig. 5.14.

The amplitude modulation of the magnetic asymmetry as a function of the photon energy for both driving wavelength are represented in fig. 5.14 (solid lines) together with the integrated modulation for the different harmonics (dots). It is possible to observe that the asymmetry is expanded along the different harmonics with opposite sign for photon energies smaller than the one of the M-edge.

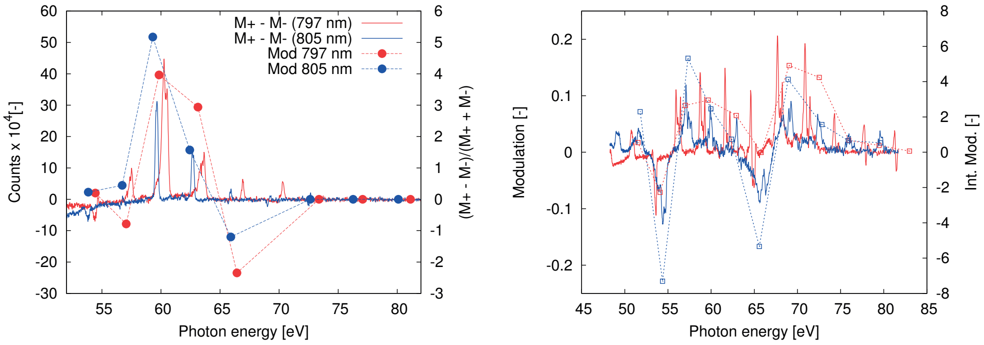

Figure 5.14: Solid lines, intensities modulation of the magnetic asymmetry for driver laser centered at different wavelengths. The discrete dots represent the signal integrated over the individual harmonics. Left, image represets the magnetic assymetry obtained for cobalt. Right, image for the permalloy sample (80% nickel, 20 % iron).

In conclusion, these first measurements on T-MOKE using our HHG beamline are encouraging for advanced pump-probe experiments in near future that will combine the HHG source with our THz pump source. Using this scheme will allow for element-selective magnetic dynamics in compounds/alloys which would be a significant step further than our results obtained in single-element thin films section 5.1.

6 Conclusions and outlook

In this work, I have presented the technical and scientific advance achieved during my thesis. The main achievements are the generation of a high-brightness electron beam, the installation and commissioning a HHG beamline, the temporal characterization of ultra-short X-ray pulses and the study of ultrafast magnetization dynamics by X-ray MOKE and XMCD using our home-built HHG beamline. The bright electron beam source described in chapter two represents a new type of metallic photo-cathode consisting of thousands of micrometric-sized filamentary Nb_3Sn superconductor wires acting as a bright electron emitter. This new approach combines the advantages of metal cathodes (fast response, low-emittance, ultrashort electron bunches) with the high QE of semiconductor-based cathodes. Up to 4800 pC could be extracted from this multifilament wire cathode by using a picosecond UV laser with intensities of 3 GW/cm^2 and accelerating voltages of 50 kV. The QE (0.9%) in this regime is 2 orders of magnitudes higher than what is reported on conventional metal photocathodes.

In chapter three, we present the studies of fully phase-matched high-order harmonics generated in a sapphire hollow waveguide by a conventional Ti:sapphire laser system emitting at 800 nm. Under optimized conditions the HH source delivers up to 10^{10} photons s^{-1} in a bandwidth of 80 eV around a central photon energy of 120 eV. Phase matching conditions of HH generation have been studied as a function of the pressure, and different behaviors of the phase matching for harmonic generation below and above the critical ionization ratio are observed, in excellent agreement with theoretical expectations. We also present the development on high-harmonic generation towards the water-window by using longer wavelengths to drive the HHG process. These developments are fundamental for expanding the spectrum of applications of the HHG sources.

In chapter four we described different techniques for temporal characterization of ultra-short x-ray pulses. I used the THz streak camera developed at PSI to characterize an entire attosecond pulse train produced by our HHG source. The striking feature of the THz streaking technique is that the characterization of ultrashort X-ray pulse trains can be performed without the need of long scans. This is a significant advance compared to conventionally used techniques. Indeed, for x-ray pulses with sufficient photon flux the THz streaking measurement can be performed within a single shot. This is fundamental for the characterization of FEL pulses, which vary significantly from shot to shot. A step towards improved performance will be the implementation of a more powerful THz source based on organic crystal. This will enable higher streak field gradients which is required for an enhanced temporal resolution towards a few fs.

The last chapter described my research efforts performed on ultrafast magnetism. We have shown that high-field terahertz pulses with a stable absolute phase offer an entirely new experimental avenue for the exploration and control of coherent subcycle femtosecond magnetization dynamics in ferromagnetic thin films. A strong phase-locking between the intense terahertz pulse and magnetization is established, with an absence of resonances (magnons, electromagnons and other modes) and heat injection. In this high-field regime, magnetization evolution is driven by the amplitude and phase of the terahertz laser. Previously inaccessible subcycle magnetization dynamics are therefore visualized. Remarkably, the magnetization response at this short timescale is very well understood by simple classical precession. This gives experimental insight into the bounds of applicability of the phenomenological LLG approach and also shows that the terahertz electric field has little influence on the magnetization dynamics.

Finally, I have installed an X-ray MOKE and XMCD scheme at our HHG source for element-selective studies on ultrafast magnetization. Thanks to the spectral characteristics of HHG it is possible to follow the dynamics of the different materials simultaneously. The use of x-ray pulses provides as well the possibility to disentangle magnetization dynamics from other purely optical effects providing a more reliable probe for magnetic studies. Future experiments on X-ray MOKE and XMCD diffraction are planned where temporal an spatial resolution are achieved combining the technique presented here with a phase retrieval technique like e.g. ptychography.

Bibliography

[1] Y. Mokrousov, G. Bihlmayer, and S. Blügel. Full-potential linearized augmented plane-wave method for one-dimensional systems: Gold nanowire and iron monowires in a gold tube. *Physical Review B*, 72(4):045402, July 2005.

[2] Todd S. Rose, Mark J. Rosker, and Ahmed H. Zewail. Femtosecond real-time probing of reactions. IV. The reactions of alkali halides. *The Journal of Chemical Physics*, 91(12):7415, 1989.

[3] Frederico A. Lima, Christopher J. Milne, Dimali C. V. Amarasinghe, Mercedes Hannelore Rittmann-Frank, Renske M. van der Veen, Marco Reinhard, Van-Thai Pham, Susanne Karlsson, Steven L. Johnson, Daniel Grolimund, Camelia Borca, Thomas Huthwelker, Markus Janousch, Frank van Mourik, Rafael Abela, and Majed Chergui. A high-repetition rate scheme for synchrotron-based picosecond laser pump-x-ray probe experiments on chemical and biological systems in solution. *Review of Scientific Instruments*, 82(6):063111, 2011.

[4] F. Schotte. Watching a Protein as it Functions with 150-ps Time-Resolved X-ray Crystallography. *Science*, 300(5627):1944–1947, June 2003.

[5] C. Consani, G. Aubock, F. van Mourik, and M. Chergui. Ultrafast Tryptophan-to-Heme Electron Transfer in Myoglobins Revealed by UV 2d Spectroscopy. *Science*, 339(6127):1586–1589, March 2013.

[6] Jing Su, Hongcheng Ni, Agnieszka Jaroń-Becker, and Andreas Becker. Time Delays in Two-Photon Ionization. *Physical Review Letters*, 113(26), December 2014.

[7] Aart Verhoef, Alexander Mitrofanov, Maria Krikunova, Nikolay M. Kabachnik, Markus Drescher, and Andrius Baltuska. Measurement of Attosecond Photoionization Delay in Xenon. page QF2C.4. OSA, 2013.

[8] P. Eckle, A. N. Pfeiffer, C. Cirelli, A. Staudte, R. Dorner, H. G. Muller, M. Buttiker, and U. Keller. Attosecond Ionization and Tunneling Delay Time Measurements in Helium. *Science*, 322(5907):1525–1529, December 2008.

[9] E. Beaurepaire, J.-C. Merle, A. Daunois, and J.-Y. Bigot. Ultrafast Spin Dynamics in Ferromagnetic Nickel. *Physical Review Letters*, 76(22):4250–4253, May 1996.

[10] Boris Vodungbo, Julien Gautier, Guillaume Lambert, Anna Barszczak Sardinha, Magali Lozano, Stéphane Sebban, Mathieu Ducousso, Willem Boutu, Kaigong Li, Bharati Tudu, Marina Tortarolo, Ranjit Hawaldar, Renaud Delaunay, Victor López-Flores, Jacek Arabski, Christine Boeglin, Hamed Merdji, Philippe Zeitoun, and Jan Lüning. Laser-induced ultrafast demagnetization in the presence of a nanoscale magnetic domain network. *Nature Communications*, 3:999, August 2012. 00030.

[11] Kraus P. M., Baykusheva D., and Hans Jakob Wörner. Two-Pulse Field-Free Orientation Reveals Anisotropy of Molecular Shape Resonance. *Physical Review Letters*, 113(2), July 2014.

[12] J. B. Bertrand, H. J. Wörner, P. Salières, D. M. Villeneuve, and P. B. Corkum. Linked attosecond phase interferometry for molecular frame measurements. *Nature Physics*, 9(3):174–178, February 2013.

[13] J. A. Armstrong. Measurement of picosecond laser pulse widths. *Applied Physics Letters*, 10(1):16, 1967.

[14] E. P. Ippen and C. V. Shank. Dynamic spectroscopy and subpicosecond pulse compression. *Applied Physics Letters*, 27(9):488, 1975.

[15] P. Maine, D. Strickland, P. Bado, M. Pessot, and G. Mourou. Generation of ultrahigh peak power pulses by chirped pulse amplification. *IEEE Journal of Quantum Electronics*, 24(2):398–403, February 1988.

[16] D. E. Spence, P. N. Kean, and W. Sibbett. 60-fsec pulse generation from a self-mode-locked Ti:sapphire laser. *Optics Letters*, 16(1):42, January 1991.

[17] P. Emma, R. Akre, J. Arthur, R. Bionta, C. Bostedt, J. Bozek, A. Brachmann, P. Bucksbaum, R. Coffee, F.-J. Decker, Y. Ding, D. Dowell, S. Edstrom, A. Fisher, J. Frisch, S. Gilevich, J. Hastings, G. Hays, Ph. Hering, Z. Huang, R. Iverson, H. Loos, M. Messerschmidt, A. Miahnahri, S. Moeller, H.-D. Nuhn, G. Pile, D. Ratner, J. Rzepiela, D. Schultz, T. Smith, P. Stefan, H. Tompkins, J. Turner, J. Welch, W. White, J. Wu, G. Yocky, and J. Galayda. First lasing and operation of an ångstrom-wavelength free-electron laser. *Nature Photonics*, 4(9):641–647, September 2010.

[18] James Rosenzweig, Gil Travish, and Luca Serafini. *The Physics and Applications of High Brightness Electron Beams*. WORLD SCIENTIFIC, 2003.

[19] A. Anghel, F. Ardana-Lamas, F. Le Pimpec, and C. P. Hauri. Large Charge Extraction from Metallic Multifilamentary Nb_3Sn Photocathode. *Physical Review Letters*, 108(19):194801, May 2012. 00000.

[20] F. Ardana-Lamas, F. Le Pimpec, A. Anghel, and C. P. Hauri. Towards high brightness electron beams from multifilamentary Nb_3Sn wire photocathode. *Physical Review Special Topics - Accelerators and Beams*, 16(4):043401, April 2013.

[21] Kun Zhao, Qi Zhang, Michael Chini, Yi Wu, Xiaowei Wang, and Zenghu Chang. Tailoring a 67 attosecond pulse through advantageous phase-mismatch. *Optics Letters*, 37(18):3891, September 2012.

[22] Tenio Popmintchev, Ming-Chang Chen, Paul Arpin, Margaret M. Murnane, and Henry C. Kapteyn. The attosecond nonlinear optics of bright coherent X-ray generation. *Nature Photonics*, 4(12):822–832, 2010. 00201.

[23] M.-C. Chen, P. Arpin, T. Popmintchev, M. Gerrity, B. Zhang, M. Seaberg, D. Popmintchev, M. M. Murnane, and H. C. Kapteyn. Bright, Coherent, Ultrafast Soft X-Ray Harmonics Spanning the Water Window from a Tabletop Light Source. *Physical Review Letters*, 105(17):173901, October 2010. 00157.

[24] S. Ackermann, A. Azima, S. Bajt, J. Bödewadt, F. Curbis, H. Dachraoui, H. Delsim-Hashemi, M. Drescher, S. Düsterer, B. Faatz, M. Felber, J. Feldhaus, E. Hass, U. Hipp, K. Honkavaara, R. Ischebeck, S. Khan, T. Laarmann, C. Lechner, Th. Maltezopoulos, V. Miltchev, M. Mittenzwey, M. Rehders, J. Rönsch-Schulenburg, J. Rossbach, H. Schlarb, S. Schreiber, L. Schroedter, M. Schulz, S. Schulz, R. Tarkeshian, M. Tischer, V. Wacker, and M. Wieland. Generation of coherent 19- and 38-nm radiation at a free-electron laser directly seeded at 38 nm. *Physical Review Letters*, 111(11):114801, September 2013. 00007.

[25] E. Allaria, R. Appio, L. Badano, W. A. Barletta, S. Bassanese, S. G. Biedron, A. Borga, E. Busetto, D. Castronovo, P. Cinquegrana, S. Cleva, D. Cocco, M. Cornacchia, P. Craievich, I. Cudin, G. D'Auria, M. Dal Forno, M. B. Danailov, R. De Monte, G. De Ninno, P. Delgiusto, A. Demidovich, S. Di Mitri, B. Diviacco, A. Fabris, R. Fabris, W. Fawley, M. Ferianis, E. Ferrari, S. Ferry, L. Froehlich, P. Furlan, G. Gaio, F. Gelmetti, L. Giannessi, M. Giannini, R. Gobessi, R. Ivanov, E. Karantzoulis, M. Lonza, A. Lutman, B. Mahieu, M. Milloch, S. V. Milton, M. Musardo, I. Nikolov, S. Noe, F. Parmigiani, G. Penco, M. Petronio, L. Pivetta, M. Predonzani, F. Rossi, L. Rumiz, A. Salom, C. Scafuri, C. Serpico, P. Sigalotti, S. Spampinati, C. Spezzani, M. Svandrlik, C. Svetina, S. Tazzari, M. Trovo, R. Umer, A. Vascotto, M. Veronese, R. Visintini, M. Zaccaria, D. Zangrando, and M. Zangrando. Highly coherent and stable pulses from the FERMI seeded free-electron laser in the extreme ultraviolet. *Nature Photonics*, 6(10):699–704, 2012. 00139.

[26] G. Lambert, T. Hara, D. Garzella, T. Tanikawa, M. Labat, B. Carre, H. Kitamura, T. Shintake, M. Bougeard, S. Inoue, Y. Tanaka, P. Salieres, H. Merdji, O. Chubar, O. Gobert, K. Tahara, and M.-E. Couprie. Injection of harmonics generated in gas in a free-electron laser providing intense and coherent extreme-ultraviolet light. *Nature Physics*, 4(4):296–300, 2008. 00238.

[27] Ulrike Frühling, Marek Wieland, Michael Gensch, Thomas Gebert, Bernd Schütte, Maria Krikunova, Roland Kalms, Filip Budzyn, Oliver Grimm, Jörg Rossbach, Elke

Plönjes, and Markus Drescher. Single-shot terahertz-field-driven X-ray streak camera. *Nature Photonics*, 3(9):523–528, 2009. 00106.

[28] Christoph P. Hauri, Clemens Ruchert, Carlo Vicario, and Fernando Ardana. Strong-field single-cycle THz pulses generated in an organic crystal. *Applied Physics Letters*, 99(16):161116, 2011. 00044.

[29] W. F. Krolikowski and W. E. Spicer. Photoemission Studies of the Noble Metals. I. Copper. *Physical Review*, 185(3):882–900, September 1969.

[30] S.I Anisimov, B.L Kapeliovich, and T.L. Perel'man. Electron emission from metal surfaces exposed to ultrashort laser pulses. *Soviet physics, JETP*, 39, 1974. 01419.

[31] William M. Haynes. *Handbook of Chemistry & Physics.* CRC Press, 96 edition, 2015.

[32] D. H. Dowell, F. K. King, R. E. Kirby, J. F. Schmerge, and J. M. Smedley. In situ cleaning of metal cathodes using a hydrogen ion beam. *Physical Review Special Topics - Accelerators and Beams*, 9(6):063502, June 2006.

[33] J.G. Wang, D.X. Wang, and M. Reiser. Beam emittance measurement by the pepper-pot method. *Nuclear Instruments and Methods in Physics Research Section A: Accelerators, Spectrometers, Detectors and Associated Equipment*, 307(2-3):190–194, October 1991.

[34] P Lu, H Vennekate, A Arnold, P Michel, P Murcek, J Teichert, and R Xiang. Transverse Emittance Measurement by Slit-scan Method for an SRF Photo Injector. *Proceedings of FEL2013, New York, NY, USA*, TUPSO44, December 2013.

[35] Dao Xiang, Ying-Chao Du, Li-Xin Yan, Ren-Kai Li, Wen-Hui Huang, Chuan-Xiang Tang, and Yu-Zheng Lin. Transverse phase space tomography using a solenoid applied to a thermal emittance measurement. *Physical Review Special Topics - Accelerators and Beams*, 12(2), February 2009.

[36] F. Le Pimpec, C. Gough, M. Paraliev, R. Ganter, C. Hauri, and S. Ivkovic . Vacuum breakdown limit and quantum efficiency obtained for various technical metals using dc and pulsed voltage sources. *Journal of Vacuum Science and Technology*, A 28:1191, 2010.

[37] V. G. Tkachenko, A. I. Kondrashev, and I. N. Maksimchuk. Advanced metal alloy systems for massive high-current photocathodes. *Applied Physics B*, 98(4):839–849, March 2010.

[38] D.H. Dowell, I. Bazarov, B. Dunham, K. Harkay, C. Hernandez-Garcia, R. Legg, H. Padmore, T. Rao, J. Smedley, and W. Wan. Cathode R&D for future light sources. *Nuclear Instruments and Methods in Physics Research Section A: Accelerators, Spectrometers, Detectors and Associated Equipment*, 622(3):685–697, October 2010.

[39] E. A. Litvinov. Theory of Explosive Electron Emission. *IEEE Transactions on Electrical Insulation*, EI-20(4):683–689, August 1985.

[40] R. Ganter, R. Bakker, C. Gough, S.C. Leemann, M. Paraliev, M. Pedrozzi, F. Le Pimpec, V. Schlott, L. Rivkin, A.F. Wrulich. Laser-Photofield Emission from Needle Cathodes for low-Emittance Electron Beams. *Phys. Rev. Lett.*, 100 (064801), 2008.

[41] R. Ganter, R.J. Bakker, C. Gough, M. Paraliev, M. Pedrozzi, F. Le Pimpec, L. Rivkin, and A. Wrulich. Nanosecond field emitted and photo-field emitted current pulses from ZrC tips. *Nuclear Instruments and Methods in Physics Research Section A: Accelerators, Spectrometers, Detectors and Associated Equipment*, 565(2):423–429, September 2006.

[42] C. P. Hauri, R. Ganter, F. Le Pimpec, A. Trisorio, C. Ruchert, and H. H. Braun. Intrinsic Emittance Reduction of an Electron Beam from Metal Photocathodes. *Physical Review Letters*, 104(23):234802, June 2010.

[43] H. Raether. *Surface plasmons on smooth and rough surfaces and on gratings*. Springer Verlag, 1988.

[44] T. Schietinger. http://amas.web.psi.ch/tools/XanaROOT/index.html.

[45] R. Ganter, editor. *SwissFEL Conceptual Design Report*. PSI-10-04. 2010.

[46] C. Pellegrini. The history of X-ray free-electron lasers. *The European Physical Journal H*, 37(5):659–708, October 2012.

[47] D. M. Ritson. A weapon for the twenty-first century. *Nature*, 328(6130):487–490, August 1987.

[48] A. McPherson, G. Gibson, H. Jara, U. Johann, T. S. Luk, I. A. McIntyre, K. Boyer, and C. K. Rhodes. Studies of multiphoton production of vacuum-ultraviolet radiation in the rare gases. *Journal of the Optical Society of America B*, 4(4):595, April 1987.

[49] M Ferray, A L'Huillier, X F Li, L A Lompre, G Mainfray, and C Manus. Multiple-harmonic conversion of 1064 nm radiation in rare gases. *Journal of Physics B: Atomic, Molecular and Optical Physics*, 21(3):L31–L35, February 1988.

[50] P. B. Corkum. Plasma perspective on strong field multiphoton ionization. *Physical Review Letters*, 71(13):1994–1997, September 1993. 04228.

[51] M. Lewenstein, Ph. Balcou, M. Yu. Ivanov, Anne L'Huillier, and P. B. Corkum. Theory of high-harmonic generation by low-frequency laser fields. *Physical Review A*, 49(3):2117–2132, March 1994. 02279.

[52] D. Bauer, D. B. Milošević, and W. Becker. Strong-field approximation for intense-laser-atom processes: The choice of gauge. *Physical Review A*, 72(2):023415, August 2005.

[53] J. Higuet, H. Ruf, N. Thiré, R. Cireasa, E. Constant, E. Cormier, D. Descamps, E. Mével, S. Petit, B. Pons, Y. Mairesse, and B. Fabre. High-order harmonic spectroscopy of the Cooper minimum in argon: Experimental and theoretical study. *Physical Review A*, 83(5):053401, May 2011.

[54] B. L. Henke, E. M. Gullikson, and J. C. Davis. X-Ray Interactions: Photoabsorption, Scattering, Transmission, and Reflection at E = 50-30,000 eV, Z = 1-92. *Atomic Data and Nuclear Data Tables*, 54(2):181–342, July 1993.

[55] Charles G. Durfee, Andy R. Rundquist, Sterling Backus, Catherine Herne, Margaret M. Murnane, and Henry C. Kapteyn. Phase Matching of High-Order Harmonics in Hollow Waveguides. *Physical Review Letters*, 83(11):2187–2190, September 1999. 00291.

[56] C M Heyl, J Güdde, A L'Huillier, and U Höfer. High-order harmonic generation with μJ laser pulses at high repetition rates. *Journal of Physics B: Atomic, Molecular and Optical Physics*, 45(7):074020, April 2012.

[57] F. Ardana-Lamas, G. Lambert, A. Trisorio, B. Vodungbo, V. Malka, P. Zeitoun, and C. P. Hauri. Spectral characterization of fully phase-matched high harmonics generated in a hollow waveguide for free-electron laser seeding. *New Journal of Physics*, 15(7):073040, July 2013.

[58] M.V Ammosov, N.B Delone, and V.P Krainov. Tunnel ionization of complex atoms and of atomic ions in an alternating electromagnetic field. *Soviet physics, JETP*, 91(6):2008, 1986. 00000.

[59] Alexandre Trisorio, Pierre M. Paul, Fabien Ple, Clemens Ruchert, Carlo Vicario, and Christoph P. Hauri. Ultrabroadband TW-class Ti:sapphire laser system with adjustable central wavelength, bandwidth and multi-color operation. *Optics Express*, 19(21):20128, October 2011.

[60] Tenio Popmintchev, Ming-Chang Chen, Dimitar Popmintchev, Paul Arpin, Susannah Brown, Skirmantas Ališauskas, Giedrius Andriukaitis, Tadas Balčiunas, Oliver D. Mücke, Audrius Pugzlys, Andrius Baltuška, Bonggu Shim, Samuel E. Schrauth, Alexander Gaeta, Carlos Hernández-García, Luis Plaja, Andreas Becker, Agnieszka Jaron-Becker, Margaret M. Murnane, and Henry C. Kapteyn. Bright Coherent Ultrahigh Harmonics in the keV X-ray Regime from Mid-Infrared Femtosecond Lasers. *Science*, 336(6086):1287–1291, June 2012. 00212.

[61] Rick Trebino, Kenneth W. DeLong, David N. Fittinghoff, John N. Sweetser, Marco A. Krumbügel, Bruce A. Richman, and Daniel J. Kane. Measuring ultrashort laser pulses in the time-frequency domain using frequency-resolved optical gating. *Review of Scientific Instruments*, 68(9):3277, 1997.

[62] C. Iaconis and I.A. Walmsley. Spectral phase interferometry for direct electric-field reconstruction of ultrashort optical pulses. *Optics Letters*, 23(10):792, May 1998.

[63] S. Grabielle, A. Moulet, N. Forget, V. Crozatier, S. Coudreau, R. Herzog, T. Oksenhendler, C. Cornaggia, and O. Gobert. Self-referenced spectral interferometry cross-checked with SPIDER on sub-15 fs pulses. *Nuclear Instruments and Methods in Physics Research Section A: Accelerators, Spectrometers, Detectors and Associated Equipment*, 653(1):121–125, October 2011.

[64] F. Quéré, Y. Mairesse, and J. Itatani. Temporal characterization of attosecond XUV fields. *Journal of Modern Optics*, 52(2-3):339–360, 2005. 00105.

[65] J. Itatani, F. Quéré, G. L. Yudin, M. Yu. Ivanov, F. Krausz, and P. B. Corkum. Attosecond Streak Camera. *Physical Review Letters*, 88(17):173903, April 2002. 00445.

[66] R. Vidal, Yi Ma, and S. Sastry. Generalized principal component analysis (GPCA). pages I–621–I–628. IEEE Comput. Soc, 2003.

[67] P. M. Paul, E. S. Toma, P. Breger, G. Mullot, F. Augé, Ph Balcou, H. G. Muller, and P. Agostini. Observation of a Train of Attosecond Pulses from High Harmonic Generation. *Science*, 292(5522):1689–1692, June 2001. 01446 PMID: 11387467.

[68] Chi-Cheng Chen, Yi-Shiun Chen, Chen-Bin Huang, and Shang-Da Yang. Non-iterative data inversion of phase retrieval by omega oscillating filtering (PROOF). In *2013 Conference on Lasers and Electro-Optics (CLEO)*, pages 1–2, June 2013.

[69] Andrei G. Stepanov, Luigi Bonacina, Sergei V. Chekalin, and Jean-Pierre Wolf. Generation of 30 μJ single-cycle terahertz pulses at 100 Hz repetition rate by optical rectification. *Optics Letters*, 33(21):2497, November 2008.

[70] C. Vicario, B. Monoszlai, Cs. Lombosi, A. Mareczko, A. Courjaud, J. A. Fülöp, and C. P. Hauri. Pump pulse width and temperature effects in lithium niobate for efficient THz generation. *Optics Letters*, 38(24):5373, December 2013.

[71] J. Clerk Maxwell. A Dynamical Theory of the Electromagnetic Field. *Philosophical Transactions of the Royal Society of London*, 155:459–512, January 1865.

[72] W. Heisenberg. Zur theorie des ferromagnetismus. *Zeitschrift für Physik*, 49(9-10):619–636, September 1928.

[73] Ernst Ising. Beitrag zur theorie des ferromagnetismus. *Zeitschrift für Physik*, 31(1):253–258, February 1925.

[74] S. T. Bramwell. Spin Ice State in Frustrated Magnetic Pyrochlore Materials. *Science*, 294(5546):1495–1501, November 2001.

[75] J. Chakhalian, J. W. Freeland, G. Srajer, J. Strempfer, G. Khaliullin, J. C. Cezar, T. Charlton, R. Dalgliesh, C. Bernhard, G. Cristiani, H.-U. Habermeier, and B. Keimer. Magnetism at the interface between ferromagnetic and superconducting oxides. *Nature Physics*, 2(4):244–248, April 2006.

[76] Tobias Kampfrath, Alexander Sell, Gregor Klatt, Alexej Pashkin, Sebastian Mährlein, Thomas Dekorsy, Martin Wolf, Manfred Fiebig, Alfred Leitenstorfer, and Rupert Huber. Coherent terahertz control of antiferromagnetic spin waves. *Nature Photonics*, 5(1):31–34, January 2011.

[77] C. Vicario, C. Ruchert, F. Ardana-Lamas, P. M. Derlet, B. Tudu, J. Luning, and C. P. Hauri. Off-resonant magnetization dynamics phase-locked to an intense phase-stable terahertz transient. *Nature Photonics*, 7(9):720–723, September 2013.

[78] Clemens Ruchert, Carlo Vicario, and Christoph P Hauri. Scaling submillimeter single-cycle transients toward megavolts per centimeter field strength via optical rectification in the organic crystal OH1. *Optics letters*, 37(5):899–901, March 2012. 00025 PMID: 22378431.

[79] M.J. Donahue and D.G. Porter. OOMMF User's Guide, Version 1.0. *National Institute of Standards and Technology, Gaithersburg, MD (Sept 1999)*, Interagency Report NISTIR 6376,, September 1999.

[80] M. Altarelli. Sum rules for X-ray magnetic circular dichroism. *Il Nuovo Cimento D*, 20(7-8):1067–1073, July 1998.

[81] B. Vodungbo, A. Barszczak Sardinha, J. Gautier, G. Lambert, M. Lozano, S. Sebban, E. Meltchakov, F. Delmotte, V. Lopez-Flores, J. Arabski, C. Boeglin, E. Beaurepaire, R. Delaunay, J. Lüning, and P. Zeitoun. Table-top resonant magnetic scattering with extreme ultraviolet light from high-order harmonic generation. *EPL (Europhysics Letters)*, 94(5):54003, June 2011. 00009.

[82] G. Malinowski, F. Dalla Longa, J. H. H. Rietjens, P. V. Paluskar, R. Huijink, H. J. M. Swagten, and B. Koopmans. Control of speed and efficiency of ultrafast demagnetization by direct transfer of spin angular momentum. *Nature Physics*, 4(11):855–858, November 2008.

[83] F. Dalla Longa, J. T. Kohlhepp, W. J. M. de Jonge, and B. Koopmans. Influence of photon angular momentum on ultrafast demagnetization in nickel. *Physical Review B*, 75(22):224431, June 2007.

[84] G. Lambert, B. Vodungbo, J. Gautier, B. Mahieu, V. Malka, S. Sebban, P. Zeitoun, J. Luning, J. Perron, A. Andreev, S. Stremoukhov, F. Ardana-Lamas, A. Dax, C. P. Hauri, A. Sardinha, and M. Fajardo. Towards enabling femtosecond helicity-dependent spectroscopy with high-harmonic sources. *Nature Communications*, 6, February 2015.

List of Abbreviations

DOS	Density of states
DFG	Difference frequency generation
EOS	Electro-optical sampling
FEL	Free electron laser
FROG	Frequency resolve optical gating
FROG-CRAB	Frequency resolve optical gating for complete reconstruction of attosecond burst
HH	High-order harmonic
HHG	High-order harmonic generation
MOKE	Magneto-optical Kerr effect
OPA	Optical parameter amplifier
PROOF	Phase retrieval by omega oscillation filtering
RABBIT	Reconstruction of attosecond beating by interference of two-photon transitions
THz	Terahertz
Ti:Sa	Titanium:sapphire
XMLD	X-ray magnetic linear dichroism
XMCD	X-ray magnetic circular dichroism

Fernando Ardana-Lamas

Date of birth: 16/02/1983
Place of birth: Cádiz, Spain
Nationality: Spain
Address: Landstarsse 29, 5415, Rieden
Email: fernando.ardana@psi.ch
Phone: +41563103510

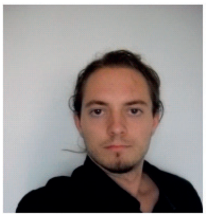

Education

- **Graduate studies**
  École polytechnique fédérale de Lausanne, Switzerland *Jan. 2011 - Present*
- **Summer internship**
  Paul Scherrer Institute, Switzerland *Jul. 2010 - Oct. 2010*
- **Exchange student**
  École polytechnique fédérale de Lausanne, Switzerland *Sep. 2009 - Jul. 2010*
- **Bachelor and Master studies in Physics**
  University of Granada, Spain *Sept. 2003 - Dec. 2010*

Languages

- Spanish: Mother language.
- English: Fluent
- French: Intermediate level understanding and speaking.
- German: Basic Level

Teaching activities

- Supervising two summer internships at Paul Scherrer Institute on the following topics:
  - High brightness photocathodes (6 months)
  - Temporal characterization of HHG pulses (6 months)
- Supervising practical lab work on the characterization of thin films used as photocathodes.

Research interest

- High-order harmonic generation
- Ultrafast magnetization dynamics
- High field THz generation
- Characterization of ultra-short X-ray pulses
- Molecular dynamics
- Free electron lasers

Computer skills

- **Python:** Data analysis, simulation and control interfaces
  Development of different applications and GUI to control the HHG beamline and for acquire and analyze the experimental data.
- **C++:** Data analysis and control interfaces
  Development of simple GUI to control the beamline and perform quick data analysis
- **EPICS:** Control system
  Integration of the developed beamline into the control system in collaboration with the control group.
- **Matlab:** Data analysis and GUI development
- **Other languages:** Mathematica, fortran, html, php, pascal
- **Linux:** Advance knowledge as user and administrator level

Selected publications

- A Anghel, F Ardana-Lamas, F Le Pimpec, and CP Hauri. Large charge extraction from metallic multifilamentary nb 3 sn photocathode. *Physical Review Letters*, 108(19):194801, 2012.
- F Le Pimpec, CJ Milne, CP Hauri, and F Ardana-Lamas. Quantum efficiency of technical metal photocathodes under laser irradiation of various wavelengths. *Applied Physics A*, 112(3):647–661, 2013.
- F Ardana-Lamas, F Le Pimpec, A Anghel, and CP Hauri. Towards high brightness electron beams from multifilamentary nb 3 sn wire photocathode. *Physical Review Special Topics-Accelerators and Beams*, 16(4):043401, 2013.
- Carlo Vicario, Clemens Ruchert, Fernando Ardana-Lamas, Peter M Derlet, B Tudu, Jan Luning, and Christoph P Hauri. Off-resonant magnetization dynamics phase-locked to an intense phase-stable terahertz transient. *Nature Photonics*, 7(9):720–723, 2013.
- F Ardana-Lamas, G Lambert, A Trisorio, B Vodungbo, V Malka, P Zeitoun, and CP Hauri. Spectral characterization of fully phase-matched high harmonics generated in a hollow waveguide for free-electron laser seeding. *New Journal of Physics*, 15(7):073040, 2013.
- PN Juranić, A Stepanov, P Peier, CP Hauri, R Ischebeck, V Schlott, M Radović, C Erny, F Ardana-Lamas, B Monoszlai, et al. A scheme for a shot-to-shot, femtosecond-resolved pulse length and arrival time measurement of free electron laser x-ray pulses that overcomes the time jitter problem between the fel and the laser. *Journal of Instrumentation*, 9(03):P03006, 2014.
- G Lambert, B Vodungbo, J Gautier, B Mahieu, V Malka, S Sebban, P Zeitoun, J Luning, J Perron, A Andreev, et al. Towards enabling femtosecond helicity-dependent spectroscopy with high-harmonic sources. *Nature Communications*, 6, 2015.

Oral presentations

- Spectral chracterization of fully phase matched high harmonics generated in a hollow waveguide for free electron laser seeding, CLEO Europe 2013, Munich
- THz streaking of attosecond pulse trains, CLEO US, 2014, San Jose
- Terahertz-driven non-resonant magnetization dynamics in cobalt, CLEO US, 2014, San Jose
- A new scheme for ultra-intense terahertz pulse generation, SPIE photonics west 2015, San Francisco
- Temporal characterization of HHG pulses by THz streaking, SPIE photonics west 2015, San Francisco

Full publication list (Google Scholar)

- A Anghel, F Ardana-Lamas, F Le Pimpec, and CP Hauri. Large charge extraction from metallic multifilamentary nb 3 sn photocathode. *Physical Review Letters*, 108(19):194801, 2012.

- Fernando Ardana Lamas. High quantum efficiency, low emittance electron beam from multifilamentary cathodes. In *CLEO: Science and Innovations*, pages JW2A–11. Optical Society of America, 2012.

- C Ruchert, C Vicario, F Ardana-Lamas, PM Derlet, B Tudu, J Luning, and CP Hauri. Field-driven femtosecond magnetization dynamics induced by ultrastrong coupling to thz transients. *arXiv preprint arXiv:1209.1280*, 2012.

- F Le Pimpec, CJ Milne, CP Hauri, and F Ardana-Lamas. Quantum efficiency of technical metal photocathodes under laser irradiation of various wavelengths. *Applied Physics A*, 112(3):647–661, 2013.

- F Ardana-Lamas, F Le Pimpec, A Anghel, and CP Hauri. Towards high brightness electron beams from multifilamentary nb 3 sn wire photocathode. *Physical Review Special Topics-Accelerators and Beams*, 16(4):043401, 2013.

- Carlo Vicario, Clemens Ruchert, Fernando Ardana-Lamas, Peter M Derlet, B Tudu, Jan Luning, and Christoph P Hauri. Off-resonant magnetization dynamics phase-locked to an intense phase-stable terahertz transient. *Nature Photonics*, 7(9):720–723, 2013.

- F Ardana-Lamas, G Lambert, A Trisorio, B Vodungbo, V Malka, P Zeitoun, and CP Hauri. Spectral characterization of fully phase-matched high harmonics generated in a hollow waveguide for free-electron laser seeding. *New Journal of Physics*, 15(7):073040, 2013.

- PN Juranić, A Stepanov, P Peier, CP Hauri, R Ischebeck, V Schlott, M Radović, C Erny, F Ardana-Lamas, B Monoszlai, et al. A scheme for a shot-to-shot, femtosecond-resolved pulse length and arrival time measurement of free electron laser x-ray pulses that overcomes the time jitter problem between the fel and the laser. *Journal of Instrumentation*, 9(03):P03006, 2014.

- Carlo Vicario, Peter Derlet, Fernando Ardana-Lamas, Clemens Ruchert, Barati Tudu, Jan Luning, and Christoph P Hauri. Terahertz-driven non-resonant magnetization dynamics in cobalt. In *CLEO: Science and Innovations*, pages SF2J–1. Optical Society of America, 2014.

- F Ardana-Lamas, C Vicario, F Le Pimpec, A Anghel, and CP Hauri. High brightness electron beams from a multi-filamentary niobium-tin photocathode. In *Proceedings of FEL2013, New York, NY, USA*, page TUPSO85, 2013.

- Fernando Ardana-Lamas, Andrey Stepanov, Christian Erny, Pavle Juranic, Christoph P Hauri, et al. Thz streaking of attosecond pulse trains. In *CLEO: QELS_Fundamental Science*, pages FM2B–8. Optical Society of America, 2014.

- F Ardana-Lamas, C Vicario, G Lambert, A Trisorio, V Malka, B Vodungbo, P Zeitoun, and CP Hauri. Fully phase matched high harmonic generation in a hollow waveguide for free electron laser seeding. In *Proceedings of FEL2013, New York, NY, USA*, page WEPSO70, 2013.

- C Vicario, F Ardana-Lamas, PM Derlet, B Tudu, J Luning, and CP Hauri. Coherent ultrafast magnetization dynamics non-resonantly induced in cobalt by an intense terahertz transient. In *Ultrafast Phenomena XIX*, pages 641–644. Springer International Publishing, 2015.

- G Lambert, B Vodungbo, J Gautier, B Mahieu, V Malka, S Sebban, P Zeitoun, J Luning, J Perron, A Andreev, et al. Towards enabling femtosecond helicity-dependent spectroscopy with high-harmonic sources. *Nature communications*, 6, 2015.

- Christoph P Hauri, Clemens Ruchert, Carlo Vicario, and Fernando Ardana. Strong-field single-cycle thz pulses generated in an organic crystal. *Applied Physics Letters*, 99(16):161116, 2011.
- Clemens Ruchert, Fernando Ardana, Alexandre Trisorio, Carlo Vicario, and Christoph P Hauri. Towards high-power single-cycle thz laser for initiating high-field-sensitive phenomena. *CHIMIA International Journal for Chemistry*, 65(5):320–322, 2011.
- Carlo Vicario, Clemens Ruchert, Fernando Ardana, and Christoph P Hauri. Laser-driven generation of intense single-cycle thz field. In *SPIE OPTO*, pages 82610Z–82610Z. International Society for Optics and Photonics, 2012.
- Fernando Ardana, Carlo Vicario, Peter Derlet, Barati Tudu, Jan Luning, and Christoph P Hauri. Coherent ultrafast magnetization dynamics non-resonantly induced in cobalt by an intense terahertz transient. In *International Conference on Ultrafast Phenomena*, pages 09–Wed. Optical Society of America, 2014.
- Clemens Ruchert, Carlo Vicario, Fernando Ardana, and Christoph P Hauri. Highly efficient generation of single-cycle MV/cm thz pulses in organic crystals. In *CLEO: Science and Innovations*, pages CM3J–2. Optical Society of America, 2012.
- Carlo Vicario, Balazs Monoszlai, Fernando Ardana, and Christoph P Hauri. Filling the entire terahertz frequency gap by single-cycle MV/cm pulses. In *International Conference on Ultrafast Phenomena*, pages 09–Wed. Optical Society of America, 2014.
- F Ardana-Lamas, C Erny, A Stepanov, I Gorgisyan, P Juranic, R Abela, and CP Hauri. Temporal characterization of individual harmonics of an attosecond pulse train by thz streaking. *arXiv preprint arXiv:1504.01958*, 2015.